UNIVERSITY OF SOUTHAMPTON

Next Generation Computational Modelling

Faculty of Engineering and Physical Science

School of Chemistry

New methods and applications of energy decomposition analysis based on large-scale first principles quantum mechanics

by

Han Chen

A thesis for the degree of

Doctor of Philosophy

June 2022

University of Southampton

Next Generation Computational Modelling

Faculty of Engineering and Physical Science

School of Chemistry

Doctor of Philosophy

New methods and applications of energy decomposition analysis based on large-scale first principles quantum mechanics

by Han Chen 

Supervised by Professor Chris-Kriton Skylaris

Abstract

Molecular systems with functional domains serve as a practical motivation for understanding the factors that contribute to the interaction energy. The ability to decompose the interaction energy of a group of interacting subsystems is an important method in studying the chemical nature of the interactions. Energy decomposition analysis (EDA) is a family of schemes that allows such dissection of the interaction energy into chemically relevant components depending on the scheme used. Since different EDA schemes decompose the interaction energy differently, the interpretation of the resulting components differs among schemes. However, various EDA schemes provide complementary insights into the interactions between chemical entities.

In this work, two EDA schemes are developed or extended: Hybrid Absolutely Localized Molecular Orbitals (HALMO) and Combined Localized Molecular Orbitals (CLMO). Both EDA schemes have been implemented as part of a linkable library alongside the computational chemistry package, ONETEP. Since ONETEP is a linear-scaling software package, an important application of such decomposition analysis is in the study of large, nontrivial molecular systems for more insightful understanding of chemical interactions, which in turn can lead to more accurate and focused design of chemical systems. Systems such as biomolecules usually contain several self-stabilizing domains that can fold independently and have important functions. Defining the fragments of a supermolecule is necessary in EDA, and if done appropriately given the

context of a particular application, the fragmentation of a biomolecule can elucidate the intramolecular interactions that contribute to the functions of the system as a whole.

Two major methods of self-consistent field for molecular interaction (SCF MI) are examined and made more mathematically transparent. SCF MI was originally designed to exclude basis set superposition error (BSSE) from molecular interactions. However, SCF MI is also used in separating charge transfer from polarization in HALMO EDA. Studying several SCF MI methods provides HALMO EDA alternatives for separating charge transfer as an EDA component.

Due to ONETEP's linear scaling, large biomolecules or large samples of biomolecules could be studied for their interactions or distributions of specific properties. The primary type of biomolecule studied in this work is double-stranded DNA (dsDNA) and how its stability relates to guanine-cytosine (GC) content, which is a measure of the amount of guanines or cytosines in nucleic acids. By examining the interaction energies in terms of EDA components, contributions to the variabilities within and across GC-content groups are examined and are correlated with differing stabilities despite having same GC content.

Ensemble density-functional theory (EDFT) optimizes the molecular orbitals of a system at finite electronic temperatures and allows occupancies to be fractional when the band gap is sufficiently small. EDA methods are normally developed for the pure state and pose difficulties in decomposing the interaction energy of a conductor due to the fractional occupancies that are part of the optimization process in EDFT. As such, fractional occupancies have been incorporated in the EDA optimization process of the fragmented species, thereby allowing EDA to be applied to systems of relevance to catalysis and metallic systems. The adaptations of EDA and SCF MI to metallic systems are novel and were validated using samples from catalysis and batteries, and HALMO EDA has provided reasonable decompositions of interaction energies and revealed some trends from SCF MI that correlate with charge distributions and chemical intuition.

Contents

Declaration of Authorship

I declare that this thesis and the work presented in it is my own and has been generated by me as the result of my own original research.

I confirm that:

1. This work was done wholly or mainly while in candidature for a research degree at this University;

2. Where any part of this thesis has previously been submitted for a degree or any other qualification at this University or any other institution, this has been clearly stated;

3. Where I have consulted the published work of others, this is always clearly attributed;

4. Where I have quoted from the work of others, the source is always given. With the exception of such quotations, this thesis is entirely my own work;

5. I have acknowledged all main sources of help;

6. Where the thesis is based on work done by myself jointly with others, I have made clear exactly what was done by others and what I have contributed myself;

7. Parts of this work have been published as:

   Han Chen and Chris-Kriton Skylaris. Analysis of DNA interactions and GC content with energy decomposition in large-scale quantum mechanical calculations. *Physical Chemistry Chemical Physics*, 23:8891–8899, 2021

   Han Chen and Chris-Kriton Skylaris. Energy decomposition analysis method for metallic systems. *Physical Chemistry Chemical Physics*, 24:1702–1711, 2022

Signed:..... Date:.....

Nomenclature

Abbreviations

OVLPS	Weighted overlap sum (5.2.2)
BSSE	Basis set superposition error
CLMO	Combined Localized Molecular Orbitals
CP	counterpoise
DFT	Density-functional theory
DNA	Deoxyribonucleic acid
EDA	Energy decomposition analysis §4
GC	Guanine-cytosine
GRS	Givens Relaxation Scheme §5.3
GS	Gram-Schmidt
HALMO	Hybrid Absolutely Localized Molecular Orbitals
JRS	Jacobi Relaxation Scheme
LMO	Localized Molecular Orbital
LP	Locally projected
MPI	Message Passing Interface
NGWF	Nonorthogonal generalized Wannier function

OpenMP	Open Multi-Processing
SCF MI	Self-consistent field for molecular interaction §6
SO	Symmetric orthogonalization §5.1
ssDNA	Single-stranded DNA
UML	Unified Modeling Language
WO	Weighted orthogonalization §5.2
CGS	Classical GS
dsDNA	Double-stranded DNA
EDFT	Ensemble DFT
gDNA	Genomic DNA
ICGS	Iterated CGS

Symbols

α	Up spin function
β	Down spin function
$\mathbf{\Phi}$	Basis functions or NGWFs (when in the context of ONETEP)
$\mathbf{\Xi}$	Selection matrix that selects specific columns of another matrix (6.2.23)
$\hat{\mathcal{O}}$	Operator
$\hat{\Omega}_J$	Partial star operator for Fragment J (6.2.27)
$\hat{P}$	Projection operator
$\mathbf{T}_{\mathrm{W}}$	Transformation matrix of WO (5.2.13)
ƒ	Diagonal matrix of occupation numbers for all spins
$\langle \hat{\mathcal{O}} \rangle$	Expectation value of an operator

$\mathbf{S}$	Overlap of basis functions ($\mathbf{\Phi}^\dagger\mathbf{\Phi}$) or NGWFs (when in the context of ONETEP)
ω	Spin function that is either α or β
$\mathbf{\Psi}$	Spatial molecular orbitals for an implicit ω
$\mathbf{f}$	Diagonal matrix of occupation numbers for an implicit ω
$\mathbf{M}$	Coefficient matrix of molecular orbitals ($\mathbf{\Phi M} = \mathbf{\Psi}$) for an implicit ω
σ	Overlap of spatial molecular orbitals ($\mathbf{\Psi}^\dagger\mathbf{\Psi}$) for an implicit ω
$\mathbf{K}$	Density kernel ($\mathbf{MfM}^\dagger$) for an implicit ω

Chapter 1

Introduction

1.1 Interactions in Molecular Systems

Molecular systems often have interacting subsystems. For example, many biomolecules interact with each other as part of biological complexes through non-covalent bonding. The nature of these intermolecular interactions is ubiquitous in protein-ligand complexes, DNA replication and repair, signaling pathways, gene expression, and many others. Interactions are the result of various types of contributions. If an interaction can be decomposed into contributing factors as components, determining which factors are the significant contributors to the interaction would aid a more accurate reduction of the number of drug candidates and facilitate the design of new drugs.

For this work, double-stranded DNA (dsDNA) is the type of biomolecule being studied (discussed in §7). In the language of DNA, there are four canonical bases: deoxyadenosine (dA), deoxythymidine (dT), deoxyguanosine (dG), and deoxycytidine (dC). The letter "d" is used to distinguish them from RNA bases, but for convenience, the same DNA bases shall be denoted without the leading "d" unless the distinction with RNA is necessary. Interactions among the four bases contribute to the level of DNA stability. Counterintuitively, thermophiles do not necessarily have higher guanine-cytosine (GC) content in their genomic DNA (gDNA) and yet are able to survive under temperatures much higher than non-thermophiles [3].

Hydrogen bonding represents a significant contribution to the stability of a double-stranded DNA. Each A-T base pair contributes two hydrogen bonds, and each G-C

base pair contributes three hydrogen bonds. As such, the amount of energy required to denature double-stranded DNA depends on the GC content, which is the percentage of nucleobases that are guanine or cytosine. Base stacking represents another significant contribution due to the π-π interactions [4]. Base stacking occurs for neighboring base pairs and, therefore, is not evident from GC content alone. In addition to the GC content, the ordering of the base pairs is thus a factor in the stability of a DNA molecule.

Due to the importance of interacting biomolecules in a supermolecule system, determining the various factors, such as GC content and base ordering, that contribute to the interaction energy of a biomolecular system would aid in the understanding of some biological phenomena. For instance, mRNA transcription involves the opening and unwinding of the DNA helix by RNA polymerase along with the aid of many transcription factors. The biochemical interactions that contribute to the interaction energy of the DNA strands affect the transcription process and efficiency. Another example is CG islands, which are regions of high GC content often associated with the beginning of a gene. GC content affects the interaction energy of the DNA helical region. Since it can be near or within the promoters of many genes, understanding how the GC content and its distribution affect the interaction energy in CG islands near such genes can elucidate some of the aspects of transcription initiation and promoter escape.

Understanding such biomolecular interactions is a motivation for using and furthering computational chemistry methods. Density-functional theory (DFT) studies usually involve simple or simplified models of biomolecules on a small scale to understand biomolecular interactions. For example, pairing of stacked amino acids and their orientations relative to each other determine the stability and interaction energy [5]. Also regarding stacking interactions, drug fragments and moieties have been studied in the context of binding to different DNA base pairs [6]. Stacking interactions and hydrogen bonding are often the focus in DFT-based studies of biomolecules, since they serve as important noncovalent contributors to the stabilization of the supermolecule.

Many of such studies usually involve very simple or simplified versions of real biomolecules. DFT calculations are expensive, and conventional software packages are cubic scaling in terms of the computation time it takes and the number of atoms in the system being studied. Biological molecules, such as proteins and nucleic acids, are

usually large or part of a larger complex of interacting units, which exceed reasonable limits in the computational time that a cubic-scaling software package takes on such systems.

ONETEP (Order-*N* Electronic Total Energy Package) is a DFT software package based on a plane-wave, pseudopotential approach that utilizes the electronic localization inherent in systems with a non-vanishing band gap [7, 8]. As such, the computational cost of a ONETEP DFT calculation scales linearly with the number of atoms and the number of processors when parallelized [9]. Due to its linear scaling, ONETEP is suitable for studying biological systems on the order of thousands of atoms [10]. On the other hand, cubic-scaling calculations in general can only handle up to hundreds of atoms at best. In addition to the size of the system, the variability of a class of systems, such as nucleic acids with different sequences, presents combinatorial problems for setting up and running large number of calculations and is exacerbated with cubic-scaling calculations.

1.2 Energy Decomposition Analysis (EDA)

While the DFT method aims to estimate the total energy of a system, the main objectives of energy decomposition analysis (EDA, discussed in §4) is to partition the interacting energy of a multi-fragment supermolecule into their chemical origins [11], such as electrostatics, exchange-correlation contributions, polarization, and charge transfer for example (cf. §4.5). EDA is thus an important analytical tool that partitions the interaction energy into chemically interpretable components.

EDA is a family of decomposition methods, each of which is known as an EDA scheme and carries out the decomposition of interaction energy into a set of chemical components. Different EDA schemes decompose interaction energy into different components. Depending on the chemical system being studied or the purpose of the study, one EDA scheme may be more applicable and interpretable than another scheme. The EDA method of Kitaura and Morokuma (KM) is a widely used EDA scheme [12] but poses numerical instabilities for the polarization and charge-transfer components when

the interactions occur at short distances and with large basis sets [13]. As such, alternative EDA schemes were proposed to address the issue, but some of these alternative schemes do not completely separate out charge transfer or do not obtain the intermediate wave functions by the variation method. The latter problem results in the charge-transfer term to be overestimated [13].

EDA schemes can be categorized according to the nature of their underlying theory [11]. There are two major categories of EDA schemes: variational-based and perturbation-based. Variational-based schemes are typically derived from the early forms of EDA. The interaction energy is decomposed by the use of intermediate wave functions. Localized Molecular Orbitals (LMO) [14], Absolutely Localized Molecular Orbitals (ALMO) [13], and Block-Localized Wavefunction (BLW) [15, 16] schemes fall into this category. Perturbation-based schemes approach EDA from the popular, symmetry-adapted perturbation theory (SAPT) scheme. The interactions among the fragments are seen as perturbations to the non-interacting description and are constructed as corrections resulting from different physical effects.

There has been other work on applying DFT and EDA to simple biomolecules in understanding some of the stabilization interactions common in biological systems and with drugs. Usually, the types of biomolecules being studied are DNA base pairs, amino acids, or interactions between the two. In order to facilitate the studies or computations, sometimes simplified versions of biomolecules with some functional groups (such as the phosphate backbone) removed are used when studying interactions between pairs and avoiding confounding factors due to other subunits and other types of biological interactions [17, 4]. While the decomposition of the interactions of base pairs, base stacking, and base pairs with amino acids on small scales serve as important starting points, studies of such interactions on larger and nontrivial systems would provide deeper insights into how the variety of nucleobases in nucleic acids or the domains of a protein come into play in biological systems and complexes [18].

1.3 HALMO-EDA and CLMO-EDA Development

Since polarization and charge transfer are important in protein-ligand interactions, accurately decomposing delocalization interactions into polarization and charge-transfer contributions would provide further insights into the interactions in biological complexes. ALMO EDA is a variational-based scheme that attempts to address the shortcomings of other schemes that do not decompose the delocalization interaction using the variation method [13]. ALMO EDA uses localized molecular orbitals that variationally calculates the polarization energy. As such, the polarization term is separated from the charge-transfer term as a natural consequence. Because the decomposition of the delocalization interaction is performed using the variation method, ALMO EDA can be applied to both strongly and weakly interacting molecules [13]. For studying biological complexes, a compatible adaptation of ALMO EDA called HALMO EDA (discussed in §4.5.2) is chosen as the scheme that provides a sensible set of components, as it has been shown to reasonably separate polarization and charge-transfer effects [11, 19].

Delocalization and basis set superposition error (BSSE) are intricately linked. The method of self-consistent field for molecular interaction (SCF MI, discussed in §6) was originally designed to exclude BSSE from molecular interactions. It does this by expanding the molecular orbitals for each fragment in the basis functions belonging to the fragment, forming localized molecular orbitals. The localized molecular orbitals are then optimized in the presence of other fragments. By the nature of SCF MI optimizing localized molecular orbitals to eliminate BSSE, SCF MI is also used in separating charge transfer from polarization in HALMO EDA, since SCF MI disallows most charge-transfer effects due to the localization of the molecular orbitals.

A new EDA scheme called Combined Localized Molecular Orbitals (CLMO, discussed in §4.5.3) was developed and implemented for treating the dispersion component of interaction energy. CLMO EDA is based on LMO EDA by Su and Li [14]. LMO EDA is a simpler scheme than ALMO/HALMO EDA and offers a robust energy decomposition that is less sensitive to the choice of basis set. LMO EDA is also computationally cheaper than HALMO EDA by obviating the complications of separating polarization and charge transfer. However, when BSSE correction is performed via the counterpoise (CP) method, LMO EDA provides two energy decompositions as

opposed to one that adjusts all of its EDA components. CLMO EDA essentially takes what are two energy decompositions in LMO EDA and combines them into one in such a way that makes BSSE correction more interpretable by the nature of its placement in the EDA components. Even though ONETEP does not exhibit BSSE [20], CLMO EDA for ONETEP still simplifies the interpretation of the energy components by providing one instead of two energy decompositions. Determining the components of the CLMO EDA can take on the form of a dedicated implementation or as a combination of the two energy decompositions from an existing LMO-EDA calculation. The CLMO-EDA implementation was compared with that of LMO EDA in GAMESS-US by applying both EDA schemes to some simple compounds as a form of validating CLMO EDA. Benchmarking results indicate good agreement with GAMESS-US, both for generalized gradient approximation (GGA) and meta-GGA functionals.

Correlation between interaction energies and GC content of 4bp (four base pairs) dsDNA were examined with HALMO EDA. GC content is a measure of the amount of guanines or cytosines in nucleic acids, and was originally treated as an indicator of nucleic-acid stability. However, recent studies suggest that GC content is insufficient in determining how stable nucleic acids are [3, 21]. In this work, computational results that support such experimental studies are provided. Unlike studies involving only overall interaction energies, HALMO EDA was used in decomposing the interaction energies of various dsDNA structures grouped by GC content in order to examine the energy components that contribute to the variabilities of the interactions energies that exist for each GC content.

1.4 EDA and Ensemble DFT

Ensemble DFT (EDFT) [22, 23] optimizes a species at finite electronic temperatures and allows occupancies to be fractional when the band gap is sufficiently small, such as in conductors. Conducting systems can also be fragmented into subsystems in order to obtain the interaction energy. However, EDA methods are normally developed for the pure state. EDA schemes pose difficulties in decomposing the interaction energy of a metallic system due to the fractional occupancies that are part of the optimization

process in EDFT. As such, fractional occupancies must also be incorporated in the EDA optimization process of the fragmented species.

Heterogeneous catalysts are important type of materials that facilitate wide-ranging reactions with chemicals and fuels, many of which involve support systems that have relatively heavy transition and post-transition metals like platinum and titanium [24]. Such catalysts have a requirement that it can form a transient reaction complex of intermediate stability. Since the reactants must interact with the catalyst, studying the interactions by energy decomposition can offer insights into the nature of the reaction complex, thereby opening up the possibility for improving the catalysis or even a class of catalytic reactions [25, 26, 27].

Although EDA is normally developed and applied to insulators, developing EDA for metallic systems or fragments that interact with each other through the conduction of charge necessitates the incorporation of EDA in EDFT, such that the interactions (which could possibly involve covalent bonding) can be dissected into contributing factors as EDA components. Motivation of and results from EDA with EDFT applied to some metallic systems with small band gaps are presented in §8.

Chapter 2

Wave Mechanics and Density-Functional Theory

2.1 Wave Mechanics

2.1.1 Schrödinger Equation

Even though density-functional theory (DFT) aims to replace functionals of wave function with functionals of electron density, references to wave-function theory serve as an essential starting perspective. The time-independent Schrödinger equation describes the electronic structure of a system and is therefore given an overview first. (Szabo and Ostlund [28] can be consulted for further details.) The time-independent Schrödinger equation is

$$\hat{H}\Psi = \Psi E \tag{2.1.1}$$

where E is the electronic energy, $\Psi = \Psi\left(\mathbf{x}_1, \mathbf{x}_2, \cdots, \mathbf{x}_N\right)$ is the wave function, and $\hat{H}$ is the Hamiltonian operator. $\mathbf{x}_i = (\mathbf{r}_i, s_i)$ is the coordinate of i-th electron that is composed of a spatial coordinate, $\mathbf{r}_i$, and a spin coordinate, s_i. In atomic units, the Hamiltonian for a system with N_{elec} electrons and N_{nucl} nuclei is

$$\hat{H} = -\sum_{i=1}^{N_{\text{elec}}} \frac{1}{2}\nabla_i^2 - \sum_{A=1}^{N_{\text{nucl}}} \frac{1}{2\mathcal{M}_A}\nabla_A^2 - \sum_{i=1}^{N_{\text{elec}}}\sum_{A=1}^{N_{\text{nucl}}} \frac{Z_A}{r_{iA}} + \sum_{i=1}^{N_{\text{elec}}}\sum_{j>i}^{N_{\text{elec}}} \frac{1}{r_{ij}} + \sum_{A=1}^{N_{\text{nucl}}}\sum_{B>A}^{N_{\text{nucl}}} \frac{Z_A Z_B}{R_{AB}} \tag{2.1.2}$$

where $\mathcal{M}_A$ is the ratio of the mass of nucleus A to the mass of an electron, and Z_A is the atomic number of nucleus A. The first term is the operator for kinetic energy of the electrons; the second term is the operator for kinetic energy of the nuclei; the third term is the Coulombic attraction between electrons and nuclei; the fourth term is the repulsion between electrons; the fifth term is the repulsion between nuclei.

An approximation to solving (2.1.1) is the Born-Oppenheimer approximation. Since nuclei are much more massive than electrons, nuclei usually move more slowly than electrons. Therefore, nuclei are assumed to be fixed in position under the Born-Oppenheimer approximation. For (2.1.2), this leads to the kinetic energy of the nuclei (corresponding to the second term) being zero, and the repulsion between nuclei (last term) being a constant. The constant adds to the eigenvalues of an operator but does not affect the eigenfunctions. Under the Born-Oppenheimer approximation and with the constant term of nuclei repulsion omitted, (2.1.2) reduces to the electronic Hamiltonian as

$$\hat{H}_{\text{elec}} = -\sum_{i=1}^{N_{\text{elec}}} \frac{1}{2}\nabla_i^2 - \sum_{i=1}^{N_{\text{elec}}} \sum_{A=1}^{N_{\text{nucl}}} \frac{Z_A}{r_{iA}} + \sum_{i=1}^{N_{\text{elec}}} \sum_{j>i}^{N_{\text{elec}}} \frac{1}{r_{ij}} \tag{2.1.3}$$

and the Schrödinger equation involving the electronic Hamiltonian becomes

$$\hat{H}_{\text{elec}} \Psi_{\text{elec}} = \Psi_{\text{elec}} E_{\text{elec}} \tag{2.1.4}$$

where $\Psi_{\text{elec}} = \Psi_{\text{elec}}\left(\{\mathbf{x}_i\}; \{\mathbf{R}_A\}\right)$ is the electronic wave function with the positions of the nuclei as parameters. For fixed nuclei, the total energy, E_{tot}, is

$$E_{\text{tot}} = E_{\text{elec}} + \sum_{A=1}^{N_{\text{nucl}}} \sum_{B>A}^{N_{\text{nucl}}} \frac{Z_A Z_B}{R_{AB}} \tag{2.1.5}$$

The electronic energy solved from the electronic Hamiltonian in (2.1.4) is used for the average field of the electrons under the same assumption that the electrons move much more quickly compared to the nuclei. The nuclear Hamiltonian, then, is

$$\hat{H}_{\text{nucl}} = -\sum_{A=1}^{N_{\text{nucl}}} \frac{1}{2\mathcal{M}_A}\nabla_A^2 + E_{\text{tot}} \tag{2.1.6}$$

and the Schrödinger equation involving the nuclear Hamiltonian becomes

$$\hat{H}_{\text{nucl}}\Psi_{\text{nucl}} = \Psi_{\text{nucl}}E \tag{2.1.7}$$

where $\Psi_{\text{nucl}} = \Psi_{\text{nucl}}(\{\mathbf{R}_A\})$ is the nuclear wave function that describes the vibration, rotation, and translation of the system. Since $\hat{H}_{\text{nucl}}$ incorporates the field of the electrons in an average way, E in (2.1.7) is the Born-Oppenheimer approximation to the energy of the system described by (2.1.1). The approximation to the wave function of the system is

$$\Psi = \Psi_{\text{elec}}\Psi_{\text{nucl}} \tag{2.1.8}$$

where the two wave functions corresponding to electrons and nuclei are decoupled and treated separately.

2.1.2 Spin Functions and Antisymmetry Principle

To fully describe an electron, its spin must be taken into account and is done by introducing two spin functions, α and β, that correspond to spin up and spin down. Each spin function is a function of a spin coordinate, s. The two spin functions are specified as complete and orthonormal:

$$\langle\alpha|\alpha\rangle = \int \alpha^*(s)\alpha(s)\,\mathrm{d}s = 1 \tag{2.1.9a}$$

$$\langle\beta|\beta\rangle = \int \beta^*(s)\beta(s)\,\mathrm{d}s = 1 \tag{2.1.9b}$$

$$\langle\alpha|\beta\rangle = \int \alpha^*(s)\beta(s)\,\mathrm{d}s = 0 \tag{2.1.9c}$$

$$\langle\beta|\alpha\rangle = \int \beta^*(s)\alpha(s)\,\mathrm{d}s = 0 \tag{2.1.9d}$$

where the Dirac bra-ket notation is used. Collectively, a spin function that is either spin up or spin down is denoted as $\omega \in \{\alpha, \beta\}$.

A Hamiltonian does not depend on spin, but the wave function of the system, Ψ, does. The antisymmetry principle states that interchanging two electron coordinates,

$\mathbf{x}_i$ and $\mathbf{x}_j$, negates the value of the wave function:

$$\Psi\left(\mathbf{x}_1, \cdots, \mathbf{x}_i, \cdots, \mathbf{x}_j, \cdots, \mathbf{x}_{N_{\text{elec}}}\right) = -\Psi\left(\mathbf{x}_1, \cdots, \mathbf{x}_j, \cdots, \mathbf{x}_i, \cdots, \mathbf{x}_{N_{\text{elec}}}\right) \tag{2.1.10}$$

for $i \neq j$. Therefore, a wave function of the system must satisfy both the Schrödinger equation and the antisymmetry principle.

2.1.3 Orbital Functions and Slater Determinant

An orbital is a wave function for a single electron. A molecular orbital is a wave function of an electron in a molecule. A spatial orbital, ψ, is a wave function of spatial coordinate, $\mathbf{r}$, such that the probability of finding an electron having a spatial coordinate between $\mathbf{r}$ and $\mathbf{r} + \mathrm{d}\mathbf{r}$ is

$$|\psi(\mathbf{r})|^2 \, \mathrm{d}\mathbf{r} \tag{2.1.11}$$

Spatial molecular orbitals of a system usually form an orthonormal set:

$$\langle \psi_i | \psi_j \rangle = \delta_{ij} \tag{2.1.12}$$

For an orbital to fully describe an electron, the spin of the electron must be taken into account. A spin molecular orbital, χ, is defined as the product of a spatial function and a spin function [28]:

$$\chi(\mathbf{x}) = \psi^{\omega}(\mathbf{r})\omega(s) \tag{2.1.13}$$

where s is the spin coordinate, and ψ^{ω} is the spatial molecular orbital associated with a generic spin function, ω. In this work, indexing over spin orbitals is for both spin functions, whereas indexing over spatial orbitals is always for one of the spin functions only, even when the spin function associated with each of them is not explicitly specified. For convenience, if the spin function associated with a spatial orbital is not specified, the spatial orbital shall be treated as having a generic spin function implicitly associated with it. When more than one spatial orbital are in the same expression without having a spin function specified, they are treated as being associated with the same generic spin

function, otherwise the spin function must be indicated. The rationale of this convention is to avoid the complexities that often arise from the differences between indexing over spin orbitals and indexing over spatial orbitals. (2.1.13) is agnostic to whether ψ^{α} and ψ^{β} are the same (as in restricted) or different (as in unrestricted). A set of spin orbitals is orthonormal if the corresponding set of spatial orbitals is orthonormal:

$$\langle \chi_i | \chi_j \rangle = \delta_{ij} \tag{2.1.14}$$

An antisymmetric wave function that serves as an approximation to the system wave function is the Slater determinant, whose value is defined as

$$\Psi_s\left(\mathbf{x}_1, \mathbf{x}_2, \cdots, \mathbf{x}_{N_{\text{elec}}}\right) \equiv \frac{1}{\sqrt{N_{\text{elec}}!}} \begin{vmatrix} \chi_a\left(\mathbf{x}_1\right) & \chi_b\left(\mathbf{x}_1\right) & \cdots & \chi_{N_{\text{elec}}}\left(\mathbf{x}_1\right) \\ \chi_a\left(\mathbf{x}_2\right) & \chi_b\left(\mathbf{x}_2\right) & \cdots & \chi_{N_{\text{elec}}}\left(\mathbf{x}_2\right) \\ \vdots & \vdots & \ddots & \vdots \\ \chi_a\left(\mathbf{x}_{N_{\text{elec}}}\right) & \chi_b\left(\mathbf{x}_{N_{\text{elec}}}\right) & \cdots & \chi_{N_{\text{elec}}}\left(\mathbf{x}_{N_{\text{elec}}}\right) \end{vmatrix} \tag{2.1.15}$$

where N_{elec} electrons occupy N_{elec} spin orbitals, and $\frac{1}{\sqrt{N_{\text{elec}}!}}$ is the normalization factor. Slater determinant satisfies the antisymmetry principle, since interchanging two electron coordinates corresponds to interchanging two rows in (2.1.15) and results in negating the value of the determinant. It also satisfies the Pauli exclusion principle, which states that no more than one electron can occupy a spin orbital. If two electrons occupy the same spin orbital, the two corresponding columns in the Slater determinant become equal, resulting in the overall determinant to be zero.

2.2 Density-Functional Theory (DFT)

2.2.1 Density Matrix

Density matrices and operators are defined and derived for spin orbitals and spatial orbitals (cf. §2.1.3). Hohenberg-Kohn theorems and Kohn-Sham approach to density-functional theory are briefly discussed. Before proceeding to the Hohenberg-Kohn theorems and the Kohn-Sham approach to density-functional theory, preliminary definitions and theorems of density matrices are presented first. Let $\mathbf{x}$ be the coordinate of

an electron that is composed of a spatial coordinate, $\mathbf{r}$, and a spin coordinate, ω. When integrating with respect to $\mathbf{x}$, $\int \mathrm{d}\mathbf{x}^N$ means integration over $3N$ spatial coordinates and summation over N spin coordinates.

The elements of a density matrix are defined as

$$\gamma_N(\mathbf{x}'_1\mathbf{x}'_2\cdots\mathbf{x}'_N,\mathbf{x}_1\mathbf{x}_2\cdots\mathbf{x}_N) = \Psi_N(\mathbf{x}'_1\mathbf{x}'_2\cdots\mathbf{x}'_N)\Psi^*_N(\mathbf{x}_1\mathbf{x}_2\cdots\mathbf{x}_N) \tag{2.2.1}$$

where $\mathbf{x}'_1\mathbf{x}'_2\cdots\mathbf{x}'_N$ and $\mathbf{x}_1\mathbf{x}_2\cdots\mathbf{x}_N$ are two independent sets of coordinates. (2.2.1) is a coordinate representation of the density operator,

$$\hat{\gamma}_N = |\Psi_N\rangle\langle\Psi_N| \tag{2.2.2}$$

The reduced density matrix of order p [29, 30, 31] is defined as

$$\gamma_p(\mathbf{x}'_1\mathbf{x}'_2\cdots\mathbf{x}'_p,\mathbf{x}_1\mathbf{x}_2\cdots\mathbf{x}_p) = \binom{N}{p}\int\cdots\int\gamma_N(\mathbf{x}'_1\mathbf{x}'_2\cdots\mathbf{x}'_p\mathbf{x}_{p+1}\cdots\mathbf{x}_N,\mathbf{x}_1\mathbf{x}_2\cdots\mathbf{x}_N)\,\mathrm{d}\mathbf{x}_{p+1}\cdots\mathrm{d}\mathbf{x}_N \tag{2.2.3}$$

The relationship of the eigenfunctions, χ_i, and their associated eigenvalues, $\mathfrak{f}_i$, for the first-order reduced density operator, $\hat{\gamma}_1$, is

$$\int\gamma_1(\mathbf{x}'_1,\mathbf{x}_1)\chi_i(\mathbf{x}_1)\,\mathrm{d}\mathbf{x}_1 = \mathfrak{f}_i\chi_i(\mathbf{x}'_1) \tag{2.2.4}$$

where χ_i are called natural spin orbitals, and $\mathfrak{f}_i$ are called occupation numbers for the natural spin orbitals [32, 31]. A requirement on γ_1 [33] is that

$$0 \le \mathfrak{f}_i \le 1 \tag{2.2.5}$$

which conforms to the rule that a spin orbital cannot be occupied by more than one electron. $\hat{\gamma}_1$ can be expressed in terms of its eigenfunctions:

$$\hat{\gamma}_1 = \sum_i \mathfrak{f}_i\,|\chi_i\rangle\langle\chi_i| \tag{2.2.6}$$

with its coordinate representation as

$$\gamma_1(\mathbf{x}_1', \mathbf{x}_1) = \left\langle \mathbf{x}_1' \middle| \hat{\gamma}_1 \middle| \mathbf{x}_1 \right\rangle \tag{2.2.7a}$$

$$= \sum_i \mathfrak{f}_i \chi_i(\mathbf{x}_1') \chi_i^*(\mathbf{x}_1) \tag{2.2.7b}$$

Occupation numbers denoted with the Fraktur typeface ($\mathfrak{f}$) are indexed for both spin functions, and when in the normal typeface ($\mathbf{f}$), they are indexed for one of the spin functions only. Similar to the convention set forth by (2.1.13), if the spin function associated with an occupation number is not specified, the occupation number shall be treated as having a generic spin function implicitly associated with it. Spinless density operator (discussed below) for a spin function is always denoted with a spin function to distinguish it from a spinless density operator that is associated with both spin functions collectively (2.2.10). When more than one occupation number are in the same expression without having a spin function specified, they are treated as being associated with the same generic spin function, otherwise the spin function must be indicated.

Using (2.1.13), (2.2.7b) can be separated into two sums by the spin function:

$$\gamma_1(\mathbf{x}', \mathbf{x}) = \sum_{\substack{i \\ \omega=\alpha}} \mathfrak{f}_i \chi_i(\mathbf{x}') \chi_i^*(\mathbf{x}) + \sum_{\substack{i \\ \omega=\beta}} \mathfrak{f}_i \chi_i(\mathbf{x}') \chi_i^*(\mathbf{x}) \tag{2.2.8a}$$

$$= \sum_i f_i^\alpha \psi_i^\alpha(\mathbf{r}') \psi_i^{\alpha*}(\mathbf{r}) \alpha^*(s) \alpha(s) + \sum_i f_i^\beta \psi_i^\beta(\mathbf{r}') \psi_i^{\beta*}(\mathbf{r}) \beta^*(s) \beta(s) \tag{2.2.8b}$$

The coordinate representation of the first-order spinless density operator, $\rho_1(\mathbf{r}', \mathbf{r})$, is obtained by integrating (2.2.8b) with respect to the spin coordinate:

$$\rho_1(\mathbf{r}', \mathbf{r}) = \int \gamma_1(\mathbf{x}', \mathbf{x}) \, \mathrm{d}s \tag{2.2.9a}$$

$$= \sum_i f_i^\alpha \psi_i^\alpha(\mathbf{r}') \psi_i^{\alpha*}(\mathbf{r}) + \sum_i f_i^\beta \psi_i^\beta(\mathbf{r}') \psi_i^{\beta*}(\mathbf{r}) \tag{2.2.9b}$$

which suggests that the operator, $\hat{\rho}_1$, itself can be defined as

$$\hat{\rho}_1 = \sum_i f_i^\alpha \left| \psi_i^\alpha \right\rangle \left\langle \psi_i^\alpha \right| + \sum_i f_i^\beta \left| \psi_i^\beta \right\rangle \left\langle \psi_i^\beta \right| = \hat{\rho}_1^\alpha + \hat{\rho}_1^\beta \tag{2.2.10}$$

along with the definition of

$$\hat{\rho}_1^{\omega} = \sum_i f_i^{\omega} \, |\psi_i^{\omega}\rangle \, \langle \psi_i^{\omega}| \tag{2.2.11}$$

For convenience, a diagonal element of the coordinate representation of $\hat{\rho}_1^{\omega}$ is denoted as

$$n^{\omega}(\mathbf{r}) = \rho_1^{\omega}(\mathbf{r}, \mathbf{r}) = \langle \mathbf{r}| \hat{\rho}_1^{\omega} \, |\mathbf{r}\rangle \tag{2.2.12}$$

and similarly for $\hat{\rho}_1$ such that

$$n(\mathbf{r}) = \rho_1(\mathbf{r}, \mathbf{r}) = n^{\alpha}(\mathbf{r}) + n^{\beta}(\mathbf{r}) \tag{2.2.13}$$

is the electron density.

Spin density is a quantity that measures the amount of spin polarization [31] and is defined as

$$Q(\mathbf{r}) = n^{\alpha}(\mathbf{r}) - n^{\beta}(\mathbf{r}) \tag{2.2.14}$$

If $Q(\mathbf{r}) \neq 0$, the system is considered to be spin polarized. If $Q(\mathbf{r}) = 0$, the system is considered not to be spin polarized, and (2.2.13) simply becomes

$$n(\mathbf{r}) = 2n^{\alpha}(\mathbf{r}) = 2n^{\beta}(\mathbf{r}) \tag{2.2.15}$$

2.2.2 Hohenberg-Kohn (HK) Theorems

The Hohenberg-Kohn (HK) theorems are two theorems of density-functional theory (DFT) and are considered to be two of the most important developments in quantum theory since the Schrödinger equation. In the HK theorems [34], the central quantity in quantum mechanics, the wave function, is replaced by the electron density.

The first HK theorem [34] demonstrates that the electron density determines both the external potential and the number of electrons. This, in turn, determines the ground-state wave function and other electronic properties. The proof of the first theorem is proof by contradiction and involves the minimum-energy principle for the ground

state. First, suppose that two external potentials, v and v', differ by more than a constant but give the same electron density for the ground state. From this, there would be two Hamiltonians, $\hat{H}$ and $\hat{H}'$, with the same ground-state electron density but with different normalized wave functions, Ψ and Ψ'. Using Ψ' as a trial function for $\hat{H}$ under the variational principle for the ground state (with $\mathbf{r}$ being the spatial coordinate of an electron and $n'(\mathbf{r}) = |\Psi'(\mathbf{r})|^2$),

$$E_0 < \langle \Psi' | \hat{H} | \Psi' \rangle = \langle \Psi' | \hat{H}' | \Psi' \rangle + \langle \Psi' | \hat{H} - \hat{H}' | \Psi' \rangle \tag{2.2.16a}$$

$$= E_0' + \int \big(v(\mathbf{r}) - v'(\mathbf{r})\big)\, n'(\mathbf{r})\, \mathrm{d}\mathbf{r} \tag{2.2.16b}$$

where E_0 and E_0' are ground-state energies for $\hat{H}$ and $\hat{H}'$, respectively. Similarly, using Ψ as a trial function for $\hat{H}'$,

$$E_0' < \langle \Psi | \hat{H}' | \Psi \rangle = \langle \Psi | \hat{H} | \Psi \rangle + \langle \Psi | \hat{H}' - \hat{H} | \Psi \rangle \tag{2.2.17a}$$

$$= E_0 - \int \big(v(\mathbf{r}) - v'(\mathbf{r})\big)\, n(\mathbf{r})\, \mathrm{d}\mathbf{r} \tag{2.2.17b}$$

Adding (2.2.16b) and (2.2.17b) as well as noting that $n' = n$ (from the initial assumption) produces

$$E_0 + E_0' < E_0' + E_0 \tag{2.2.18}$$

which is a contradiction. Therefore, there is a one-to-one mapping between electron density and external potential. Since n determines v and the number of electrons, the total energy, $E_v[n]$, can be written as

$$E_v[n] = V_{\mathrm{ne}}[n] + T[n] + V_{\mathrm{ee}}[n] \tag{2.2.19a}$$

$$= \int v(\mathbf{r}) n(\mathbf{r})\, \mathrm{d}\mathbf{r} + F[n] \tag{2.2.19b}$$

where the subscript in E_v indicates that the total energy depends on the external potential, $T[n]$ is kinetic energy, V_{ne} is potential energy due to nucleus-electron interactions,

V_{ee} is potential energy due to electron-electron interactions, and

$$F[n] = T[n] + V_{ee}[n] \tag{2.2.20}$$

is an unknown but universal functional that is defined independently of the external potential.

The second HK theorem [34] provides the energy variational principle. For a trial density, $\tilde{n}(\mathbf{r})$, such that

$$\tilde{n}(\mathbf{r}) \geq 0 \text{ and} \tag{2.2.21a}$$

$$\int \tilde{n}(\mathbf{r})\, d\mathbf{r} = N, \tag{2.2.21b}$$

where N is the number of electrons, $E_v[\tilde{n}]$ is never less than the ground-state energy, E_0:

$$E_0 \leq E_v[\tilde{n}] \tag{2.2.22}$$

This theorem allows a trial electron-density function, $\tilde{n}$, to be varied in order to obtain the ground state.

To prove (2.2.22), let $\tilde{n}$ be an electron density that determines $\tilde{v}$ and $\tilde{\Psi}$, of which the latter is used as a trial function for $\hat{H}$ having v as the external potential:

$$E_0 \leq \langle \tilde{\Psi} | \hat{H} | \tilde{\Psi} \rangle = \int v(\mathbf{r})\tilde{n}(\mathbf{r})\, d\mathbf{r} + F[\tilde{n}] \tag{2.2.23a}$$

$$= E_v[\tilde{n}] \tag{2.2.23b}$$

2.2.3 Kohn-Sham (KS) DFT Approach

After the development of the HK theorems, Kohn and Sham [35] realized that most of the problems with density-functionals are related to the way the kinetic energy is determined and noticed that previous methods of approximating the kinetic energy were crude. As such, a fictitious system, the Kohn-Sham (KS) system, was introduced and is constructed from a set of orbitals such that the electrons are non-interacting and

that the kinetic energy is calculated based on the wave function, which is then a single Slater determinant.

The KS method introduces orbitals of a fictitious system where the electrons are non-interacting and the kinetic energy can be calculated with a small correction that is dealt with separately. The kinetic energy of N independent electrons is

$$T_s = -\sum_{i=1}^{N} \left\langle \chi_i \middle| \frac{1}{2}\nabla_i^2 \middle| \chi_i \right\rangle \tag{2.2.24}$$

where χ_i are KS spin molecular orbitals. The electron density is

$$n(\mathbf{r}) = \sum_{\omega\in\{\alpha,\beta\}} \sum_{i=1}^{N^\omega} \psi_i^{\omega *}(\mathbf{r})\psi_i^{\omega}(\mathbf{r}) \tag{2.2.25}$$

Kohn and Sham [35] constructed a fictitious non-interacting system as a reference that has the following as the Hamiltonian:

$$\hat{H}_s = \sum_{i}^{N} \hat{h}_s(i) \tag{2.2.26}$$

where

$$\hat{h}_s(i) = -\frac{1}{2}\nabla_i^2 + v_s(\mathbf{r}) \tag{2.2.27}$$

which has no electron-electron repulsion, and the ground-state electron density is exactly n. v_s is the external potential (which was discussed in §2.2.2) for the non-interacting system. Such a fictitious system has an exact ground-state wave function as

$$\Psi_s = \frac{1}{\sqrt{N!}} \det\left[\chi_a \chi_b \cdots \chi_N\right] \tag{2.2.28}$$

which is the Slater determinant (2.1.15) where $\{\chi_i\}$ are the eigenfunctions with the N lowest eigenvalues of the one-electron Hamiltonians:

$$\hat{h}_s(i)\chi_i(\mathbf{x}) = \varepsilon_i \chi_i(\mathbf{x}) \tag{2.2.29}$$

$T_s[n]$ is not the exact kinetic-energy functional, which is $T[n]$. Kohn and Sham [35] rewrote (2.2.20) as

$$F[n] = T_s[n] + J[n] + E_{\text{xc}}[n] \tag{2.2.30}$$

where

$$J[n] = \frac{1}{2} \iint \frac{1}{|\mathbf{r}_2 - \mathbf{r}_1|} n(\mathbf{r}_1) n(\mathbf{r}_2) \, \mathrm{d}\mathbf{r}_1 \, \mathrm{d}\mathbf{r}_2 \tag{2.2.31a}$$

$$E_{\text{xc}}[n] = T[n] - T_s[n] + V_{\text{ee}}[n] - J[n] \tag{2.2.31b}$$

thereby placing the small (but non-zero) difference, $T[n] - T_s[n]$, into the exchange-correlation energy, $E_{\text{xc}}[n]$.

The ground-state electron density minimizes (2.2.19b) and satisfies the Euler equation,

$$\mu = v(\mathbf{r}) + \frac{\delta F[n]}{\delta n(\mathbf{r})} \tag{2.2.32a}$$

$$= v(\mathbf{r}) + \frac{\delta J[n]}{\delta n(\mathbf{r})} + \frac{\delta E_{\text{xc}}[n]}{\delta n(\mathbf{r})} + \frac{\delta T_s[n]}{\delta n(\mathbf{r})} \tag{2.2.32b}$$

$$= v_{\text{eff}}(\mathbf{r}) + \frac{\delta T_s[n]}{\delta n(\mathbf{r})} \tag{2.2.32c}$$

where v is the external potential of the original interacting system, and μ is the Lagrange multiplier with the constraint of

$$\int n(\mathbf{r}) \, \mathrm{d}\mathbf{r} = N \tag{2.2.33}$$

v_{eff} is the KS effective potential, which from (2.2.32c) is defined as

$$v_{\text{eff}}(\mathbf{r}) = v(\mathbf{r}) + \frac{\delta J[n]}{\delta n(\mathbf{r})} + \frac{\delta E_{\text{xc}}[n]}{\delta n(\mathbf{r})} \tag{2.2.34a}$$

$$= v(\mathbf{r}) + \int \frac{n(\mathbf{r}')}{|\mathbf{r} - \mathbf{r}'|} \, \mathrm{d}\mathbf{r}' + v_{\text{xc}}(\mathbf{r}) \tag{2.2.34b}$$

with v_{xc} as the exchange-correlation potential,

$$v_{xc}(\mathbf{r}) = \frac{\delta E_{xc}[n]}{\delta n(\mathbf{r})} \tag{2.2.35}$$

The KS procedure must be performed self-consistently, since $v_{eff}(\mathbf{r})$ depends on $n(\mathbf{r})$ via (2.2.34b). Starting with a guessed $n(\mathbf{r})$, $v_{eff}(\mathbf{r})$ is determined. Invoking the non-interacting reference system and by the form of (2.2.32c), $v_s(\mathbf{r})$ is substituted by $v_{eff}(\mathbf{r})$ in (2.2.27) to give

$$\left(-\frac{1}{2}\nabla_i^2 + v_{eff}(\mathbf{r})\right)\chi_i = \varepsilon_i \chi_i \tag{2.2.36}$$

which is solved for $\{\chi_i\}$. A different $n(\mathbf{r})$ is then obtained from (2.2.25). From (2.2.34b) again, a new $v_{eff}(\mathbf{r})$ is determined, and the procedure is repeated until self consistency is achieved. The KS DFT approach is an exact theory that uses the same self-consistent machinery from the Hartree-Fock (HF) approximation [28].

2.2.4 General Forms of Exchange-Correlation Functionals

Exchange-correlation functionals are classified by the types of approximation that have varying degrees of accuracy. The different forms of approximation rely on the electron density in specific ways. Generally, exchange-correlation functionals that incorporate additional dependencies on the electron density have higher accuracy (as in Jacob's ladder [36], Figure 2.1). Exchange-correlation functions can be categorized based on their characteristics [37]:

- Local density approximation (LDA) functionals: depend on only the electron density, n.
- Generalized gradient approximation (GGA): correct LDA functionals with the electron density gradient, ∇n.
- Meta-GGA functionals: correct GGA functionals with the kinetic energy density, τ.
- Hybrid functionals: mix the Hartree-Fock exchange integral, E_x^{HF}, at a constant ratio.

Functionals usually attempt to satisfy fundamental physical conditions (e.g., exchange-correlation energies must be negative definite) while accurately reproducing various properties of a wide range of molecules [37].

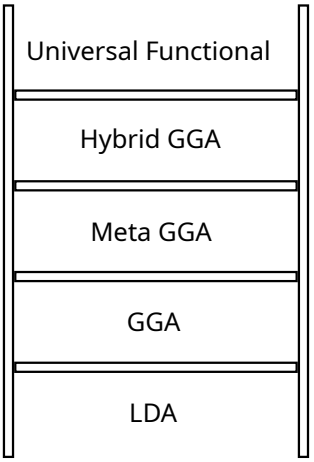

FIGURE 2.1: Jacob's ladder of exchange-correlation functionals [36].

2.2.4.1 LDA and GGA Functionals

LDA functionals are focused only on the electron density at a certain point in space and is the simplest of all exchange-correlation functionals. Usually used in the Kohn-Sham method, the Dirac LDA exchange functional is

$$E_{\mathrm{x}}^{\mathrm{LDA}}[n] = -\frac{3}{4}\left(\frac{3}{\pi}\right)^{1/3}\int n^{4/3}(\mathbf{r})\,\mathrm{d}\mathbf{r} \tag{2.2.37}$$

and is found to be the exact LDA exchange functional. Unlike the exchange functional, there is no exact LDA correlation functional, so approximate functionals are developed instead [37]. Most popular LDA correlation functionals are VWN [38] and PW [39]. The VWN correlation functional was developed so that it converges to the high and low electron density limits by fitting parameters to the expected correlation energy of a uniform density gas given by the quantum Monte Carlo method [38, 37]. The PW correlation functional, in turn, modifies the VWN correlation functional to reduce the number of parameters and to satisfy more fundamental physical conditions [39, 37].

GGA functionals are gradient-corrected approximation (GCA) functionals that are more accurate than LDA functionals by utilizing the gradient of the electron density to treat the non-uniformity of the electron density. GGA exchange functionals have a

general form [40] defined by

$$E_{\mathrm{x}}^{\mathrm{GGA}} = -\frac{1}{2}\sum_{\omega}\int c_{\omega} n_{\omega}^{4/3}\,\mathrm{d}\mathbf{r} \tag{2.2.38}$$

where $\omega \in \{\alpha, \beta\}$ is a spin, and c_ω is a dimensionless quantity that is usually expressed in terms of the dimensionless parameter, x_ω:

$$x_{\omega} = \frac{|\nabla n_{\omega}|}{n_{\omega}^{4/3}} \tag{2.2.39}$$

Widely used GGA exchange functionals usually only have differing c_ω. However, c_ω in turn varies greatly for large x_ω, which indicates a region of low electron density or high electron density gradient. This implies that different GGA exchange functionals can yield significantly different exchange-energy values. An example of c_ω is for the PBE exchange functional [41, 37]:

$$c_{\omega}^{\mathrm{PBE}} = c_{\omega}^{\mathrm{LDA}}\left(1 + \kappa - \frac{\kappa}{1 + \frac{\mu x_{\omega}^2}{(48\pi^2)^{2/3}\kappa}}\right) \tag{2.2.40}$$

where $\mu = 0.21951$, $\kappa = 0.804$, and

$$c_{\omega}^{\mathrm{LDA}} = 3\left(\frac{3}{4\pi}\right)^{1/3} \tag{2.2.41}$$

GGA correlation functionals can be further categorized into density gradient approximation and Colle-Salvetti (CS) type functionals. Functionals of the density gradient approximation type are developed in a similar manner to the GGA exchange functionals by determining a general form and then attempting to satisfy some fundamental physical conditions of the correlation energy. The popular PW91 and PBE correlation functionals are in this category. The CS type is developed from a correlation wave function that multiplies an uncorrelated wave function with a correlation function to give a correlation hole satisfying the correlation cusp condition [37]. An example of a CS-type functional is the LYP functional. Density gradient approximation-type functionals often have complicated forms with many fitted parameters, while the CS-type functionals usually have simple forms. CS-type functionals can have highly accurate

correlation energies, but unlike the density gradient approximation-type functionals, CS-type functionals often do not satisfy fundamental physical conditions [37].

2.2.4.2 Meta-GGA and Hybrid Functionals

Meta-GGA functionals incorporate the kinetic energy density in addition to the electron density gradient as an attempt to improve upon GGA. Meta-GGA functionals share the general form [42] of

$$E_{\mathrm{xc}}^{\mathrm{GCA}}[n] = \int \epsilon_{\mathrm{xc}}(n(\mathbf{r}), \nabla n(\mathbf{r}), \tau(\mathbf{r}))\, \mathrm{d}\mathbf{r} \tag{2.2.42}$$

where ϵ_{xc} is the exchange-correlation energy per unit volume, and

$$\tau(\mathbf{r}) = \frac{1}{2}\sum_i |\nabla \psi_i(\mathbf{r})|^2 \tag{2.2.43}$$

is the kinetic-energy density with i iterating over occupied spatial orbitals. Meta-GGA functionals include VS98 [43], PKZB [44], TPSS [45], and B97M-V [46]. These functionals have varying degrees of parameterization, satisfaction of fundamental physical conditions, and reproducibility of observed exchange-correlation energies of molecules.

Hybrid functionals are at a higher rung on Jacob's ladder compared to meta-GGA functionals. However, instead of building upon meta-GGA, hybrid functionals mix the Hartree-Fock exchange energy to GGA exchange functionals at a constant ratio [37] in lieu of the kinetic energy density. As such, hybrid functionals make the connection between the exchange energy of a non-interacting electron model system and the exchange energy of the corresponding fully interacting system, where the latter is described by the Hartree-Fock exchange energy. Hybrid functionals take on the form [37] of

$$E_{\mathrm{x}}^{\mathrm{hybrid}} = \int_0^1 E_{\mathrm{x}}^{\lambda}\, \mathrm{d}\lambda \approx E_{\mathrm{x}}^{\mathrm{GGA}} + \lambda\left(E_{\mathrm{x}}^{\mathrm{HF}} - E_{\mathrm{x}}^{\mathrm{GGA}}\right) \tag{2.2.44}$$

where $0 \leq \lambda \leq 1$ is the coupling strength parameter [47]. Hybrid functionals are not considered to be corrections to the exchange functionals. Rather, their definitions are based on the assumption that the exact exchange energy is somewhere between the

GGA exchange energy and the Hartree-Fock exchange energy, as suggested by (2.2.44) and the presence of a coupling strength parameter. Some hybrid functionals include B3LYP [48], PBE0 [49], and HSE [50].

B3LYP is the first hybrid functional and is the most popular of all functionals [37]. B3LYP [48] has three parameters as mixing ratios, and includes the GGA term of the B88 exchange functional [51] and the LYP-GGA correlation functional [52]:

$$E_{\mathrm{xc}}^{\mathrm{B3LYP}} = E_{\mathrm{xc}}^{\mathrm{LDA}} + a_1 \left(E_{\mathrm{x}}^{\mathrm{HF}} - E_{\mathrm{x}}^{\mathrm{LDA}} \right) + a_2 E_{\mathrm{x}}^{\mathrm{B88}} + a_3 \left(E_{\mathrm{c}}^{\mathrm{LYP}} - E_{\mathrm{c}}^{\mathrm{VWN\text{-}LDA}} \right) \tag{2.2.45}$$

with the mixing ratios $a_1 = 0.2$, $a_2 = 0.72$, and $a_3 = 0.81$.

2.2.5 Linear-Scaling DFT and ONETEP

DFT calculations can be sped up when a system is divided into subsystems and only nearby neighboring subsystems are considered. This property of matter is known as nearsightedness of electronic matter (NEM) and serves as the physical basis of linear scaling [53]. A system is arbitrarily divided into subsystems, each with a volume of V_n and has a surrounding buffer zone with a size of B_n. The buffer zones overlap each other and mark transitory distances prior to a hard cutoff of the range of interactions to consider. A buffer zone can be adjusted according to the desired accuracy and plays the role of removing long-range ionic interactions.

ONETEP (Order-*N* Electronic Total Energy Package) [8] is a DFT software package based on a reformulated, plane-wave, pseudopotential approach that utilizes the electronic localization inherent in systems (which are usually solids or semiconductors) with a non-vanishing band gap. As such, the computational cost of a ONETEP DFT calculation scales linearly with the number of atoms and the number of processors when parallelized [9].

The time taken by a ONETEP calculation is a function of increasing number of atoms for a given number of processors is linear. For example, an eight-fold increase in computational power (such as increasing the number of processors) allows calculations for eight times the number of atoms in same amount of time, instead of only twice the number of atoms as in the cubic-scaling approaches in conventional DFT programs.

The cubic scaling is caused by a consequence of the delocalized nature of the wave functions, which are the eigen solutions of the KS single-particle Hamiltonian.

To achieve the linear scaling that ONETEP has, a crossover point must be met. The crossover point is defined as the number of atoms such that a linear-scaling approach becomes faster than a conventional, cubic-scaling approach. The onset of linear scaling occurs only after the number of atoms exceeds this critical value. The crossover point is system-dependent but often lies on the order of hundreds of atoms. As single-processor workstations are capable of calculations with roughly no more than 100 atoms, it is important to use multiprocessor computers in order to gain any benefit of linear-scaling DFT.

ONETEP uses a linear-scaling method that employs a basis set of orthogonal and localized functions. Such basis set allows systematic control of truncation errors and accurate representation of the kinetic-energy operator [9]. The localized quantities lead to a physical way of dividing the computational effort among many processors to allow calculations to be performed in parallel. What distinguishes this approach is that the localization is achieved in a controlled and mathematically consistent manner so that ONETEP obtains the same accuracy as cubic-scaling plane-wave approaches, while offering fast and stable convergence [9].

ONETEP aims to obtain the same result as solving a set of single-particle Schrödinger equations in DFT:

$$\hat{h}(i)\psi_i(\mathbf{r}) = \left(-\frac{1}{2}\nabla_i^2 + v(\mathbf{r})\right)\psi_i(\mathbf{r}) = \varepsilon_i\psi_i(\mathbf{r}) \tag{2.2.46}$$

where $\hat{h}(i)$ is the one-electron Hamiltonian for the i-th electron with ε_i as energy eigenvalues and $\psi_i(\mathbf{r})$ as spatial eigenfunctions. Information about the ground-state system is contained in the single-particle density operator (2.2.10). At absolute zero temperature, the occupation number, f_i, is restricted to either 0 or 1.

The ONETEP formalism is often based on the assumption of a closed-shell description. Therefore, it is important to note the difference in the formulas of the electron-density function, n, which depend on whether the indexing is over spin or spatial orbitals. When the indexing is over spatial orbitals, the electron density is occasionally

written as

$$n(\mathbf{r}) = 2\rho(\mathbf{r}, \mathbf{r}) \tag{2.2.47}$$

which appears to differ from (2.2.13). The discrepancy lies in the fact that the indexing in (2.2.13) is over spin orbitals and that $\rho(\mathbf{r}, \mathbf{r})$ is incorrectly treated as the electron density for only one of the spins.

If there is a band gap in the system, the density matrix decays exponentially as a function of $|\mathbf{r}' - \mathbf{r}|$. The density matrix, then, can be truncated to a sparse band-diagonal form such that the amount of information it contains increases linearly with its size [9]. The density kernel, $\mathbf{K}$, is used to achieve the truncation, and its elements are defined as

$$K_{ij} = \sum_k M_{ik} f_k \left(\mathbf{M}^\dagger\right)_{kj} \tag{2.2.48}$$

over occupied molecular orbitals for a particular spin with occupation numbers as $\mathbf{f}$ (cf. §2.2.1) and expansion coefficients of molecular orbitals as $\mathbf{M}$. Using the density kernel, the elements of the density matrix can be written as

$$\rho(\mathbf{r}, \mathbf{r}') = \sum_{\iota,\kappa} \phi_\iota(\mathbf{r}) K_{\iota\kappa} \phi_\kappa^*(\mathbf{r}') \tag{2.2.49}$$

where $\{\phi_\iota\}$ is a set of spatially localized orbitals called nonorthogonal generalized Wannier functions (NGWFs) [54]. The truncation is carried out by setting

$$K_{\iota\kappa} = 0 \tag{2.2.50}$$

when

$$|\mathbf{R}_\iota - \mathbf{R}_\kappa| > r_{\text{cut}} \tag{2.2.51}$$

where $\mathbf{R}_\iota$ and $\mathbf{R}_\kappa$ are the centers of localization regions of ϕ_ι and ϕ_κ, respectively, for a cutoff distance, r_{cut}.

Localization of NGWFs is performed by restricting the construction of NGWFs where

only the contributions to them that are within defined spherical regions centered on atoms are selected. Any contributions that are outside the localization spheres are therefore truncated and not part of the conjugate-gradient optimization process [7, 9]. Each NGWF is expanded in an orthogonal set of periodic sinc (psinc) functions equivalent to a plane-wave basis set:

$$\phi_\iota(\mathbf{r}) = \sum_{m \in L_\iota} D(\mathbf{r} - \mathbf{r}_m) C_{m\iota} \tag{2.2.52}$$

where each psinc, $D(\mathbf{r} - \mathbf{r}_m)$, is centered at $\mathbf{r}_m$ on a real-space Cartesian grid [55]. $C_{m\iota}$ is non-zero only when the corresponding psinc falls within the localization region, L_ι. A psinc function is

$$D(\mathbf{r} - \mathbf{r}_m) = \frac{1}{N_1 N_2 N_3} \sum_{p=-J_1}^{J_1+1} \sum_{q=-J_2}^{J_2+1} \sum_{s=-J_3}^{J_3+1} e^{i(p\mathbf{B}_1 + q\mathbf{B}_2 + s\mathbf{B}_3)\cdot(\mathbf{r}-\mathbf{r}_m)} \tag{2.2.53}$$

where $\{N_k\}$ are number of grid points along each direction in the simulation cell, $\{J_k\}$ are integers (discussed next), and $\{\mathbf{B}_k\}$ are reciprocal lattice vectors as

$$\mathbf{B}_1 = \frac{2\pi\,(\mathbf{A}_2 \times \mathbf{A}_3)}{\mathbf{A}_1 \cdot (\mathbf{A}_2 \times \mathbf{A}_3)} \tag{2.2.54}$$

with $\{\mathbf{A}_k\}$ being the primitive direct lattice vectors. Originally, J_k is merely stated to be an integer and is not defined per se [55]. Rather, N_k is defined in terms of J_k as

$$N_k = 2J_k + 2 \tag{2.2.55}$$

which implies that N_k must be an even integer with one grid point at each boundary. Dividing (2.2.55) by 2 suggests that J_k must be the number of grid points in half of the simulation cell along a direction without counting the grid point at the boundary. The purpose of not including the boundary grid point in J_k is so that the summations in (2.2.53) can avoid double counting the grid point located at a boundary, which is periodic.

The total energy is variationally minimized with respect to both the density kernel and the NGWFs. The method of minimizing the energy is done using two nested

loops. Corresponding to the outer loop, the set of NGWFs is varied. Corresponding to the inner loop, the density kernel is optimized with respect to a fixed set of NGWFs. The density kernel is constrained to be idempotent, which imposes orthogonality of the orbitals. The constraint is applied in ONETEP using a modified Li-Nunes-Vanderbilt (LNV) scheme [56, 57, 58] where the energy is minimized with respect to an auxiliary density kernel. The relationship between the auxiliary density kernel, **L**, and the density kernel, **K**, is

$$\mathbf{K} = 3\mathbf{LSL} - 2\mathbf{LSLSL} \tag{2.2.56}$$

where

$$S_{ij} = \int \phi_i^*(\mathbf{r})\phi_j(\mathbf{r})\,\mathrm{d}\mathbf{r} \tag{2.2.57}$$

is the overlap of NGWFs, and **L** is nearly idempotent. By (2.2.56), the auxiliary density kernel causes the density kernel to approach idempotency.

Chapter 3

Bra-Ket Matrix: A New Mathematical and Computational Construct

The bra-ket matrix is a new construct developed in this work that concisely expresses mathematical formulations and computational methods. It is based on the Dirac notation and aims to compactly formulate mathematical and computational intentions as matrices instead of the usual summations over elements of matrix products. By employing the bra-ket matrices, many summations are genuinely eliminated and are turned into matrix multiplications. This differs from the usage of the Einstein notation, which merely omits the summation symbol and relies on conventions to imply how the summation is performed. Bra-ket matrices are essentially ordinary mathematical matrices and, hence, can take advantage of the computing architecture in code that is dominated by matrix multiplication [59]. After defining the bra-ket matrix and its properties, some of the constructs previously discussed are re-expressed in bra-ket matrices for use henceforth.

3.1 Definitions and Operations

A matrix where each column corresponds to a ket is called a ket matrix. Similarly, a matrix where each row corresponds to a bra is called a bra matrix. A bra-ket matrix is a

generic term that refers to both types. To define the nature of the elements of a bra-ket matrix, let a ket matrix, $\mathbf{A}$, be denoted as

$$\mathbf{A} = \begin{pmatrix} |a_1\rangle & |a_2\rangle & \cdots \end{pmatrix} \tag{3.1.1}$$

where $|a_i\rangle$ is a column that represents a ket (which can be a vector or function according to the Dirac notation). The conjugate transpose of $\mathbf{A}$ is therefore a bra matrix, denoted as

$$\mathbf{A}^\dagger = \begin{pmatrix} \langle a_1| \\ \langle a_2| \\ \vdots \end{pmatrix} \tag{3.1.2}$$

Since a ket or bra is respectively represented by a column or row in a matrix, the scalar products of two bra-ket matrices, $\mathbf{A}$ and $\mathbf{B}$, follows the usual matrix multiplication:

$$\mathbf{A}^\dagger\mathbf{B} = \begin{pmatrix} \langle a_1|b_1\rangle & \langle a_1|b_2\rangle & \cdots \\ \langle a_2|b_1\rangle & \langle a_2|b_2\rangle & \cdots \\ \vdots & \vdots & \ddots \end{pmatrix} \tag{3.1.3}$$

For kets that are vectors, the columns in a ket matrix trivially correspond to the vectors. If the kets are functions however, the columns are determined via Cholesky decomposition of the overlap of a set of basis functions that the ket functions can be expanded in. Suppose a ket matrix, $\mathbf{A}$, whose elements are to be determined is written as a product of two matrices:

$$\mathbf{A} = \mathbf{\Phi}\mathbf{M} \tag{3.1.4}$$

where $\mathbf{\Phi}$ is a ket matrix that represents the basis functions, and $\mathbf{M}$ is a coefficient matrix. Determining $\mathbf{\Phi}$ is discussed below. First, observe that (3.1.4) expresses each ket in $\{|a_i\rangle\}$ in terms of the basis functions, $\{|\phi_k\rangle\}$, when written in the definition of matrix

multiplication:

$$|a_i\rangle = \sum_k |\phi_k\rangle M_{ki} \tag{3.1.5}$$

where the only semantic difference is that a ket is now represented by a matrix column regardless of whether the ket is a vector or a function. The number of elements in the matrix column representing a ket in (3.1.5) is the number of basis functions, making the construction compatible with the matrix multiplication in (3.1.4). As such, (3.1.4) provides the mathematical means of constructing a ket matrix from a basis set and coefficient matrix if both are known.

In practice, the coefficient matrix and the overlap of the basis functions are usually known, but the basis functions, $\mathbf{\Phi}$, themselves are not. Despite this, the matrix elements of $\mathbf{\Phi}$ can be determined by Cholesky decomposition. If the overlap of the basis functions is denoted as $\mathbf{S}$, its Cholesky decomposition would be $\mathbf{S} = \mathbf{U}^\dagger\mathbf{U}$. $\mathbf{U}$ is an upper triangular matrix that can be defined to be equal to $\mathbf{\Phi}$, which from (3.1.3) would recover the original overlap as $\mathbf{S} = \mathbf{\Phi}^\dagger\mathbf{\Phi}$. Given $\mathbf{S}$ and $\mathbf{M}$, $\mathbf{A}$ can be constructed as a ket matrix that is directly implementable and manipulated as an ordinary matrix in code, even when the kets are functions. Conversely, given $\mathbf{\Phi}$ and $\mathbf{A}$, $\mathbf{M}$ can be determined by back substitution. Along with Cholesky decomposition, (3.1.4) serves as the bridge between mathematical expressions and computational implementations using bra-ket matrices.

Since a bra-ket matrix can be treated as an ordinary matrix, the usual matrix operations are the same for bra-ket matrices. Nevertheless, care should be taken when a bra-ket matrix is viewed as a conceptual container for bra-kets, since the kets or bras contained in the bra-ket matrix must also be treated accordingly such that the inherent semantics of the Dirac notation are preserved. Multiplication of bra-ket matrices is standard matrix multiplication that respects the commutativity of the bra-kets being

multiplied. For instance,

$$\mathrm{tr}\left(\mathbf{A}^{\dagger}\mathbf{B}\right) = \sum_i \langle a_i | b_i \rangle \tag{3.1.6a}$$

$$\mathbf{A}\mathbf{B}^{\dagger} = \begin{pmatrix} |a_1\rangle & |a_2\rangle & \cdots \end{pmatrix} \begin{pmatrix} \langle b_1| \\ \langle b_2| \\ \vdots \end{pmatrix}$$

$$= \sum_i |a_i\rangle \langle b_i| = \sum_i \left(|a_i\rangle \otimes_{\text{outer}} |b_i\rangle \right) \tag{3.1.6b}$$

where the first equality is a scalar, and the second equality is a matrix that can be thought of as the sum of the corresponding outer products (since a ket is a column). Note that the right-hand sides of (3.1.3) and (3.1.6) yield the usual Dirac expressions commonly seen in mathematical formulations of quantum chemistry when summations are used.

3.2 Linear Operators

To denote the application of a linear operator, $\hat{\mathcal{O}}$, on many kets using bra-ket matrices, $\hat{\mathcal{O}}$ should first be expressed as a bra-ket matrix in a manner that is consistent with the definitions and operations of bra-ket matrices. This can be achieved by arbitrarily defining a linear operator as a ket times a bra without loss of generality:

$$\hat{\mathcal{O}} |a\rangle \equiv \left(|c\rangle \langle b| \right) |a\rangle \tag{3.2.1a}$$

$$= |c\rangle \xi \tag{3.2.1b}$$

$$\equiv \left|a'\right\rangle \tag{3.2.1c}$$

where $|b\rangle$ and $|c\rangle$ are intermediate kets, ξ is an intermediate scalar, and $|a\rangle$ is effectively mapped to $|a'\rangle$ by $\hat{\mathcal{O}}$. This suggests that $\hat{\mathcal{O}}$ can be expressed as a bra-ket matrix that has multiple rows and columns, where determining it is discussed below. Extending

the application of $\hat{\mathcal{O}}$ to multiple kets or bras gives

$$\hat{\mathcal{O}}\mathbf{A} = \begin{pmatrix} \hat{\mathcal{O}} \left|a_1\right\rangle & \hat{\mathcal{O}} \left|a_2\right\rangle & \cdots \end{pmatrix} \tag{3.2.2a}$$

$$\mathbf{A}^\dagger \hat{\mathcal{O}}^\dagger = \begin{pmatrix} \left\langle a_1\right| \hat{\mathcal{O}}^\dagger \\ \left\langle a_2\right| \hat{\mathcal{O}}^\dagger \\ \vdots \end{pmatrix} \tag{3.2.2b}$$

where the distribution of $\hat{\mathcal{O}}$ to each ket or bra is in accordance with the usual block-matrix multiplication. From the equations of (3.2.2), the matrix representation of $\hat{\mathcal{O}}$ in $\mathbf{\Phi}$ is

$$\mathbf{\Phi}^\dagger \hat{\mathcal{O}} \mathbf{\Phi} = \begin{pmatrix} \left\langle \phi_1\right| \hat{\mathcal{O}} \left|\phi_1\right\rangle & \left\langle \phi_1\right| \hat{\mathcal{O}} \left|\phi_2\right\rangle & \cdots \\ \left\langle \phi_2\right| \hat{\mathcal{O}} \left|\phi_1\right\rangle & \left\langle \phi_2\right| \hat{\mathcal{O}} \left|\phi_2\right\rangle & \cdots \\ \vdots & \vdots & \ddots \end{pmatrix} \tag{3.2.3}$$

On the other hand, if $\hat{\mathcal{O}}$ is defined or expressed in terms of bra-ket matrices, then the resulting expression is referred as $\hat{\mathcal{O}}$ in bra-ket matrix, which is distinguished from its matrix representation in a basis set.

If $\hat{\mathcal{O}}$ is in the form of a bra-ket matrix, implementation of $\hat{\mathcal{O}}\mathbf{A} = \mathbf{A}'$ becomes an ordinary matrix multiplication, lending directness and conciseness in code. To determine a Hermitian operator, $\hat{\mathcal{O}}$, as a bra-ket matrix given its basis functions, $\mathbf{\Phi}$, and its matrix representation, $\mathbf{O}$, the system of equations

$$\mathbf{\Phi}^\dagger \hat{\mathcal{O}} \mathbf{\Phi} = \mathbf{O} \tag{3.2.4}$$

is solved using two forward substitutions, since $\mathbf{\Phi}^\dagger$ is a lower triangular matrix. Letting $\mathbf{y} = \hat{\mathcal{O}}\mathbf{\Phi}$,

$$\mathbf{\Phi}^\dagger \mathbf{y} = \mathbf{O} \tag{3.2.5}$$

is solved for $\mathbf{y}$ using forward substitution. $\hat{\mathcal{O}}$ is then determined by solving

$$\mathbf{\Phi}^\dagger \hat{\mathcal{O}} = \mathbf{y}^\dagger \tag{3.2.6}$$

using another forward substitution. Even though $\hat{\mathcal{O}}$ in bra-ket matrix form is an ordinary matrix in code, caution must be taken not to confuse it with its matrix representation, $\mathbf{O}$, which is another matrix with different elements as implied by (3.2.4).

3.3 Working with Eigenvalue Equations

In general, the eigenvalues corresponding to the eigenvectors or eigenfunctions of $\hat{\mathcal{O}}$ can be obtained using the left inverse of a ket matrix. Suppose $\mathbf{\Psi}$ is a ket matrix whose columns are the eigenfunctions of $\hat{\mathcal{O}}$ with the corresponding square diagonal matrix of eigenvalues, $\boldsymbol{\varepsilon}$. The eigenvalue equation in bra-ket matrices would be

$$\hat{\mathcal{O}}\mathbf{\Psi} = \mathbf{\Psi}\boldsymbol{\varepsilon} \tag{3.3.1}$$

Multiplying both sides by the left inverse of $\mathbf{\Psi}$ gives the eigenvalues:

$$\boldsymbol{\varepsilon} = \mathbf{\Psi}_{\mathrm{L}}^{-1}\hat{\mathcal{O}}\mathbf{\Psi} \tag{3.3.2}$$

where

$$\mathbf{\Psi}_{\mathrm{L}}^{-1} = \left(\mathbf{\Psi}^{\dagger}\mathbf{\Psi}\right)^{-1}\mathbf{\Psi}^{\dagger} \tag{3.3.3}$$

If $\mathbf{\Psi} = \begin{pmatrix} |\Psi\rangle \end{pmatrix}$ is a one-column ket matrix that represents the wave function, (3.3.2) becomes the expectation value of $\hat{\mathcal{O}}$:

$$\left\langle \hat{\mathcal{O}} \right\rangle = \left(\langle\Psi|\Psi\rangle^{-1} \langle\Psi| \right) \hat{\mathcal{O}} \, |\Psi\rangle \tag{3.3.4a}$$

$$= \frac{\langle\Psi| \, \hat{\mathcal{O}} \, |\Psi\rangle}{\langle\Psi|\Psi\rangle} \tag{3.3.4b}$$

The above mathematical approach to obtaining the eigenpairs is not normally done in practice. Since the matrix representation of the operator (and not the operator itself) is given, (3.3.1) is usually rewritten in matrices and then solved as an eigenvalue equation.

To demonstrate the utility of bra-ket matrices in eigenvalue equations, let us first formulate one where the Kohn-Sham molecular orbitals are solved from the given matrix

representation of a Hamiltonian without bra-ket matrices. The conventional formulation begins with the expansion of one molecular orbital, $|\psi_i\rangle$, as

$$|\psi_i\rangle = \sum_k |\phi_k\rangle \, M_{ki} \tag{3.3.5}$$

where $\{|\phi_k\rangle\}$ is the basis set, and M_{ki} is the coefficient associated with $|\phi_k\rangle$ in the expansion of $|\psi_i\rangle$. Applying the Hamiltonian operator, $\hat{H}$, produces the eigenvalue equation

$$\sum_k \hat{H} \, |\phi_k\rangle \, M_{ki} = \sum_k |\phi_k\rangle \, M_{ki}\varepsilon_i \tag{3.3.6}$$

where ε_i is the eigenvalue (also called orbital energy in this context) associated with $|\psi_i\rangle$. To get the Hamiltonian operator expressed in terms of the elements of its matrix representation, both sides are further multiplied by $\langle\phi_\ell|$:

$$\sum_k \langle\phi_\ell|\hat{H}|\phi_k\rangle \, M_{ki} = \sum_k \langle\phi_\ell|\phi_k\rangle \, M_{ki}\varepsilon_i \tag{3.3.7}$$

Letting $H_{\ell k} = \langle\phi_\ell|\hat{H}|\phi_k\rangle$ and $S_{\ell k} = \langle\phi_\ell|\phi_k\rangle$, the eigenvalue equation for one molecular orbital becomes

$$\sum_k H_{\ell k} M_{ki} = \sum_k S_{\ell k} M_{ki}\varepsilon_i \tag{3.3.8}$$

The long-winded nature of using summations is eliminated with bra-ket matrices. Given the matrix representation, $\mathbf{H}$, of a Hamiltonian, the eigenvalue equation for all molecular orbitals can be immediately formulated without summations:

$$\hat{H}\boldsymbol{\Psi} = \boldsymbol{\Psi}\boldsymbol{\varepsilon} \tag{3.3.9a}$$

$$\boldsymbol{\Phi}^\dagger \hat{H} \boldsymbol{\Phi}\mathbf{M} = \boldsymbol{\Phi}^\dagger \boldsymbol{\Phi}\mathbf{M}\boldsymbol{\varepsilon} \tag{3.3.9b}$$

$$\mathbf{H}\mathbf{M} = \mathbf{S}\mathbf{M}\boldsymbol{\varepsilon} \tag{3.3.9c}$$

Although (3.3.9) may be a trivial example, the directness of manipulating equations using bra-ket matrices becomes particularly apparent in complicated mathematical formulations that involve many matrix multiplications.

For this work, almost all places (both mathematical and computational) directly work with orbital functions themselves as bra-ket matrices, not in their expanded form as $\mathbf{\Phi M}$. As a consequence, the mathematical formulations in this work are simplified, since there is no longer the necessity that an expression be in terms of the basis overlap or the coefficient matrix, with only a small number of exceptions. Exceptions include scenarios where the density kernel, $\mathbf{K} = \mathbf{MfM}^\dagger$, is needed (cf. §3.4), and in fragment-based methods where block matrices are incompatible (e.g., SCF MI discussed in §6). On the other hand, orthogonalization methods, for example, are more demanding in that the orbital functions must not be treated and implemented as expanded in the basis set with a coefficient matrix (discussed in §5.2.2.1). Otherwise, the mathematical formulations, computational implementations, and performance of such orthogonalization methods would suffer drastically.

3.4 Density Operator, Basis Set, and Density Kernel

The first-order reduced density operator (2.2.6) can be defined in terms of bra-ket matrices. Let $\mathbf{X} = \begin{pmatrix} |\chi_1\rangle & |\chi_2\rangle & \cdots \end{pmatrix}$ be a ket matrix of orthonormal spin molecular orbitals. The first-order reduced density operator (2.2.6) in bra-ket matrices is

$$\hat{\gamma} = \mathbf{X}\mathfrak{f}\mathbf{X}^\dagger \tag{3.4.1}$$

where $\mathfrak{f}$ is a square diagonal matrix of occupation numbers for the spin orbitals.

The ket matrix of the spatial molecular orbitals (from (2.1.13)) is denoted as $\mathbf{\Psi} = \begin{pmatrix} |\psi_1\rangle & |\psi_2\rangle & \cdots \end{pmatrix}$. The first-order spinless density operator for a spin function ω (2.2.11) in bra-ket matrices would be

$$\hat{\rho}^\omega = \mathbf{\Psi}^\omega \mathbf{f}^\omega \mathbf{\Psi}^{\omega\dagger} \tag{3.4.2}$$

where $\mathbf{f}^\omega$ is a square diagonal matrix of occupation numbers for the spatial orbitals associated with ω.

The density kernel allows the density operator for a particular spin to be expressed in terms of spatial basis functions. Let $\mathbf{\Phi} = \begin{pmatrix} |\phi_1\rangle & |\phi_2\rangle & \cdots \end{pmatrix}$ be the ket matrix of spatial

basis functions that are the same for both spin functions. The spatial molecular orbitals can be expanded as

$$\mathbf{\Psi} = \mathbf{\Phi}\mathbf{M} \tag{3.4.3}$$

where $\mathbf{M}$ is a matrix of expansion coefficients such that each column corresponds to a spatial molecular orbital for a spin function. (3.4.2) written in terms of the basis functions is

$$\hat{\rho}^{\omega} = \mathbf{\Phi}\mathbf{M}^{\omega}\mathbf{f}^{\omega}\mathbf{M}^{\omega\dagger}\mathbf{\Phi}^{\dagger} \tag{3.4.4a}$$

$$= \mathbf{\Phi}\mathbf{K}^{\omega}\mathbf{\Phi}^{\dagger} \tag{3.4.4b}$$

with the definition of

$$\mathbf{K} = \mathbf{M}\mathbf{f}\mathbf{M}^{\dagger} \tag{3.4.5}$$

as the density kernel for an implicit ω.

In ONETEP, spin-polarized calculations involve two density kernels, one for each spin function. On the other hand, calculations that are not spin polarized involve only one density kernel by utilizing (2.2.15), where both spin functions have the same density kernel.

3.5 One-Electron and Two-Electron Integrals

3.5.1 One-Electron Integral

The core Hamiltonian for the i-th electron is denoted as $\hat{h}(i)$ and is the sum of the electron's kinetic energy and potential energy due to all nuclei:

$$\hat{h}(i) = -\frac{1}{2}\nabla_i^2 - \sum_A \frac{Z_A}{r_{iA}} \tag{3.5.1}$$

where A is a nucleus, Z_A is the atomic number of A, and r_{iA} is the distance between the i-th electron and A. The trace of the one-electron integrals is

$$\operatorname{tr}\left(\mathfrak{f}\mathbf{X}^\dagger\hat{h}\mathbf{X}\right) = \sum_i \mathfrak{f}_i \left\langle \chi_i \middle| \hat{h}(i) \middle| \chi_i \right\rangle \tag{3.5.2a}$$

$$= \sum_i \mathfrak{f}_i \int \chi_i^*(\mathbf{x})\hat{h}(i)\chi_i(\mathbf{x})\,\mathrm{d}\mathbf{x} \tag{3.5.2b}$$

where $\hat{h}$ is the core Hamiltonian for whatever electron it is acting on, χ_i is a spin orbital, and $\mathfrak{f}_i$ is an occupation number associated with χ_i that is along the diagonal of $\mathfrak{f}$. Using (2.1.13), (3.5.2) can be separated for each spin:

$$\operatorname{tr}\left(\mathfrak{f}\mathbf{X}^\dagger\hat{h}\mathbf{X}\right) = \sum_{\omega\in\{\alpha,\beta\}} \operatorname{tr}\left(\mathbf{f}^\omega\mathbf{\Psi}^{\omega\dagger}\hat{h}\mathbf{\Psi}^\omega\right) \tag{3.5.3}$$

where ω is a spin function (cf. §2.2.1), $\mathbf{\Psi}^\omega$ is a ket matrix of spatial orbitals associated with ω, and $\mathbf{f}^\omega$ is a square diagonal matrix of occupation numbers corresponding to $\mathbf{\Psi}^\omega$. With the property that compatible matrices commute in a trace, (3.5.3) can be readily expressed in terms of basis functions, $\mathbf{\Phi}$, and density kernel, $\mathbf{K}^\omega$, through the coefficient matrix, $\mathbf{M}^\omega$, when needed:

$$\operatorname{tr}\left(\mathfrak{f}\mathbf{X}^\dagger\hat{h}\mathbf{X}\right) = \sum_{\omega\in\{\alpha,\beta\}} \operatorname{tr}\left(\mathbf{f}^\omega\mathbf{M}^{\omega\dagger}\mathbf{\Phi}^\dagger\hat{h}\mathbf{\Phi}\mathbf{M}^\omega\right) \tag{3.5.4a}$$

$$= \sum_{\omega\in\{\alpha,\beta\}} \operatorname{tr}\left(\mathbf{M}^\omega\mathbf{f}^\omega\mathbf{M}^{\omega\dagger}\mathbf{\Phi}^\dagger\hat{h}\mathbf{\Phi}\right) \tag{3.5.4b}$$

$$= \sum_{\omega\in\{\alpha,\beta\}} \operatorname{tr}\left(\mathbf{K}^\omega\mathbf{\Phi}^\dagger\hat{h}\mathbf{\Phi}\right) \tag{3.5.4c}$$

3.5.2 Two-Electron Integral

Before formulating the two-electron integral as bra-ket matrices, the physicists' and chemists' notations for two-electron integrals are defined first [28]. The physicists' notation is

$$\langle\chi_i\chi_j|\chi_k\chi_\ell\rangle = \int \chi_i^*(\mathbf{x}_1)\chi_j^*(\mathbf{x}_2)r_{12}^{-1}\chi_k(\mathbf{x}_1)\chi_\ell(\mathbf{x}_2)\,\mathrm{d}\mathbf{x}_1\,\mathrm{d}\mathbf{x}_2 \tag{3.5.5}$$

whereas the chemists' notation is

$$[\chi_i\chi_j|\chi_k\chi_\ell] = \int \chi_i^*(\mathbf{x}_1)\chi_j(\mathbf{x}_1)r_{12}^{-1}\chi_k^*(\mathbf{x}_2)\chi_\ell(\mathbf{x}_2)\,\mathrm{d}\mathbf{x}_1\,\mathrm{d}\mathbf{x}_2 \tag{3.5.6}$$

These notations are defined in Szabo and Ostlund [28] but are not necessarily adhered by all literature, although most do. One particular exception relevant to EDA is the work by Su and Li [14], which uses the unconventional notation where $\langle\chi_i\chi_j|\chi_k\chi_\ell\rangle$ is actually the chemists' notation according to Szabo and Ostlund [28]. The chemists' notation as in (3.5.6) is never used in this work, since it is incompatible with bra-ket matrices as demonstrated below. The physicists' notation as in (3.5.5) is always used instead.

In the context of bra-ket matrices, the physicists' notation is used without regard to whether the orbitals are spin or spatial. Instead, the type of orbitals is explicitly indicated with the orbital functions themselves, and the notation where indices alone (as in $\langle ij|k\ell\rangle$) is not used. The matrices from §3.4 are reused here. Only the Coulomb integral is explored for bra-ket matrices. The exchange integral poses difficulties for bra-ket matrices and happens not to be used in this work, so it is not discussed.

Prior to deriving the Coulomb integrals for multiple molecular orbitals in bra-ket matrices, the case for two orbitals is examined first. The Coulomb integral for two molecular orbitals, ψ_i and ψ_j, is

$$\langle\psi_i\psi_j|\psi_i\psi_j\rangle = \int \psi_i(\mathbf{r}_1)\psi_i^*(\mathbf{r}_1)r_{12}^{-1}\psi_j(\mathbf{r}_2)\psi_j^*(\mathbf{r}_2)\,\mathrm{d}\mathbf{r}_1\,\mathrm{d}\mathbf{r}_2 \tag{3.5.7}$$

and similarly for two basis functions, ϕ_i and ϕ_j. Expressing (3.5.7) in terms of the basis functions gives

$$\langle\psi_i\psi_j|\psi_i\psi_j\rangle = \sum_{\iota,\kappa,\lambda,\mu} M_{\iota i}M_{\kappa i}^*\langle\phi_\kappa\phi_\mu|\phi_\iota\phi_\lambda\rangle M_{\lambda j}M_{\mu j}^* \tag{3.5.8}$$

Rearranging the expansion coefficients, the Coulomb integral becomes

$$\langle\psi_i\psi_j|\psi_i\psi_j\rangle = \sum_{\iota,\kappa,\lambda,\mu} M_{\kappa i}^*M_{\mu j}^*\langle\phi_\kappa\phi_\mu|\phi_\iota\phi_\lambda\rangle M_{\iota i}M_{\lambda j} \tag{3.5.9}$$

which provides the rationale for the following definition. The Coulomb integral in terms of the basis functions as ket matrices is defined as

$$|\psi_i\psi_j\rangle = \begin{pmatrix} |\phi_1\phi_1\rangle & |\phi_1\phi_2\rangle & \cdots & |\phi_2\phi_1\rangle & |\phi_2\phi_2\rangle & \cdots \end{pmatrix} (\mathbf{m}_i \otimes_{\text{Kron}} \mathbf{m}_j) \tag{3.5.10a}$$

$$= \check{\mathbf{\Phi}} (\mathbf{m}_i \otimes_{\text{Kron}} \mathbf{m}_j) \tag{3.5.10b}$$

where $\mathbf{m}_k$ is a column matrix of expansion coefficients for the k-th spatial molecular orbital, and $\otimes_{\text{Kron}}$ is the Kronecker product. The ordering of the elements of $\check{\mathbf{\Phi}}$ is dictated by the ordering of the rows of $\mathbf{m}_k$. Furthermore, due to the nature of the Kronecker product, the grouping of the elements of $\check{\mathbf{\Phi}}$ always begins with electron-one and then electron-two.

To extend (3.5.10) to include all molecular orbitals with the same grouping as $\check{\mathbf{\Phi}}$, the Kronecker product would be extended as

$$\begin{pmatrix} \mathbf{m}_1 \otimes_{\text{Kron}} \mathbf{m}_1 & \mathbf{m}_1 \otimes_{\text{Kron}} \mathbf{m}_2 & \cdots & \mathbf{m}_2 \otimes_{\text{Kron}} \mathbf{m}_1 & \mathbf{m}_2 \otimes_{\text{Kron}} \mathbf{m}_2 & \cdots \end{pmatrix} \tag{3.5.11}$$

which can be factored as $\mathbf{M} \otimes_{\text{Kron}} \mathbf{M}$ based on the definition of the Kronecker product and the ordering of the molecular orbitals. Therefore, the ket matrix for the Coulomb integral across all molecular orbitals is

$$\check{\mathbf{\Psi}} = \begin{pmatrix} |\psi_1\psi_1\rangle & |\psi_1\psi_2\rangle & \cdots & |\psi_2\psi_1\rangle & |\psi_2\psi_2\rangle & \cdots \end{pmatrix} \tag{3.5.12a}$$

$$= \check{\mathbf{\Phi}} (\mathbf{M} \otimes_{\text{Kron}} \mathbf{M}) \tag{3.5.12b}$$

where again the grouping of the elements of $\check{\mathbf{\Psi}}$ always begins with electron-one and then electron-two. Note that the ordering of the elements of $\check{\mathbf{\Psi}}$ is dictated by the ordering of the columns of $\mathbf{M}$. (3.5.12) illustrates why the physicists' notation must be used.

The conjugate transpose of $\breve{\mathbf{\Psi}}$ is simply

$$\breve{\mathbf{\Psi}}^{\dagger} = \begin{pmatrix} \langle \psi_1 \psi_1 | \\ \langle \psi_1 \psi_2 | \\ \vdots \\ \langle \psi_2 \psi_1 | \\ \langle \psi_2 \psi_2 | \\ \vdots \end{pmatrix} \tag{3.5.13}$$

with the direction of the angle brackets flipped as expected. This is not possible with the chemists' notation, since taking its conjugate does not change the direction of its square bracket.

Analogous to the one-electron integrals of (3.5.3), the sum of the Coulomb integrals for all molecular orbitals (without double-counting correction) is

$$\mathrm{tr}\left((\mathbf{f} \otimes_{\mathrm{Kron}} \mathbf{f})\, \breve{\mathbf{\Psi}}^{\dagger} \breve{\mathbf{\Psi}} \right) = \sum_{i,j} f_i f_j \left\langle \psi_i \psi_j | \psi_i \psi_j \right\rangle \tag{3.5.14}$$

where $(\mathbf{f} \otimes_{\mathrm{Kron}} \mathbf{f})$ is a square diagonal matrix of occupation-number products in the same ordering as $\breve{\mathbf{\Psi}}$. Written in terms of $\breve{\mathbf{\Phi}}$ and density kernel, $\mathbf{K}$,

$$\mathrm{tr}\left((\mathbf{f} \otimes_{\mathrm{Kron}} \mathbf{f})\, \breve{\mathbf{\Psi}}^{\dagger} \breve{\mathbf{\Psi}} \right) = \mathrm{tr}\left((\mathbf{M} \otimes_{\mathrm{Kron}} \mathbf{M})\, (\mathbf{f} \otimes_{\mathrm{Kron}} \mathbf{f})\, \left(\mathbf{M}^{\dagger} \otimes_{\mathrm{Kron}} \mathbf{M}^{\dagger} \right) \breve{\mathbf{\Phi}}^{\dagger} \breve{\mathbf{\Phi}} \right) \tag{3.5.15a}$$

$$= \mathrm{tr}\left(\left(\mathbf{M}\mathbf{f}\mathbf{M}^{\dagger} \otimes_{\mathrm{Kron}} \mathbf{M}\mathbf{f}\mathbf{M}^{\dagger} \right) \breve{\mathbf{\Phi}}^{\dagger} \breve{\mathbf{\Phi}} \right) \tag{3.5.15b}$$

$$= \mathrm{tr}\left((\mathbf{K} \otimes_{\mathrm{Kron}} \mathbf{K})\, \breve{\mathbf{\Phi}}^{\dagger} \breve{\mathbf{\Phi}} \right) \tag{3.5.15c}$$

With bra-ket matrices, the Coulomb integral for all molecular orbitals can be expressed without a myriad of summations and indices in its formulation such as for (3.5.9).

Chapter 4

Energy Decomposition Analysis (EDA)

4.1 Categories and Schemes

While the KS DFT method aims to estimate the total energy of a system, the main objective of energy decomposition analysis (EDA) is to partition the interacting energy of a multi-fragment supermolecule into their chemical origins, such as electrostatics, exchange-correlation contributions, polarization, and any other relevant chemical phenomena depending on the scheme of the decomposition. The interaction energy of a system is

$$\Delta E_{\text{int}} = E_{\text{supermol}} - \sum_i E_{\text{frag},i} \tag{4.1.1}$$

where E_{supermol} is the energy of the supermolecule, and $E_{\text{frag},i}$ is the energy of an isolated fragment in the geometry that it has within the supermolecule. Hence, EDA is an important analytical tool that partitions the interaction energy into chemically interpretable components.

There are several versions of EDA known as schemes. The EDA schemes can be categorized according to the nature of their underlying theory [11]. There are two major categories of EDA schemes:

1. **Variational-based methods.** These schemes are typically derived from the early forms of EDA. The interaction energy is decomposed by the use of intermediate wave functions. Localized Molecular Orbitals (LMO) [14], Absolutely Localized Molecular Orbitals (ALMO) [13], and Block-Localized Wavefunction (BLW) [15, 16] schemes fall in this category.

2. **Perturbation-based methods.** These schemes approach EDA from the popular, symmetry-adapted perturbation theory (SAPT) scheme. The interactions among the fragments are seen as perturbations to the non-interacting description and are constructed as corrections resulting from different physical effects. These methods are not discussed.

Many variational schemes are derived from the original scheme known as the Kitaura-Morokuma (KM) scheme [60, 12, 61]. Some of these variational schemes include reduced variational space (RVS), constrained space orbital variations (CSOV), and natural energy decomposition analysis (NEDA) [11, 19]. Each EDA scheme has unique approaches to the decomposition of the interaction energy with various advantages and disadvantages.

One of the pressing problems addressed by EDA is the separation of polarization and charge-transfer effects. EDA schemes like LMO do not attempt such separation and have the two effects combined as one EDA component. Those that do separate polarization and charge transfer have different ways of achieving it. KM, RVS [62], CSOV [63, 64], ALMO, and other schemes in this category impose localization of the molecular orbitals to respective fragments and applies constraints to the optimization of such localized molecular orbitals. Based on natural bond orbital (NBO) theory [65, 66], the NEDA scheme [67, 68, 69, 70] uses a very localized view of bonding, but its approach does not involve the variational optimization of the polarized state.

In ONETEP, the EDA scheme being further developed and used in this work is Hybrid Absolutely Localized Molecular Orbitals (HALMO), which is based on two other schemes: LMO [14] and ALMO [13]. The decomposition of the interaction energy into frozen density, polarization, and charge transfer is based on ALMO EDA. Further decomposition of the frozen-density component is based on LMO EDA. LMO (cf. §4.5.1)

and HALMO (cf. §4.5.2) EDA schemes are discussed in detail in their respective sections. A brief description of them is given here.

LMO EDA is an EDA scheme implemented in GAMESS-US by Su and Li [14] that is intended to be robust and basis-set insensitive. It is developed for both HF-based and KS methods, but only the latter is discussed for this work. LMO EDA does not have a charge-transfer component but has an energy component that is called polarization. However, the polarization in LMO EDA (discussed in §4.5.1) is not the same as the polarization in HALMO EDA (discussed in §4.5.2), which is taken to be the same as that of ALMO EDA [13, 19].

Polarization in ALMO/HALMO EDA arises from SCF MI (§6). After it is determined, charge-transfer simply becomes the remaining component of the interaction energy. LMO EDA intentionally omits the calculation of the charge-transfer component due to its basis-set sensitivity [14]. Since LMO EDA does not concern itself with charge transfer, SCF MI is not used in LMO EDA, making LMO EDA a simpler scheme to start with in understanding the hybrid approach of HALMO EDA. As such, the definitions of LMO EDA shall be presented as a groundwork for understanding HALMO EDA afterwards. Because frozen density, polarization, and charge transfer in HALMO EDA are the same as in ALMO EDA, it is not necessary to discuss ALMO EDA on its own in this work.

Before presenting the equations for LMO EDA, some conventions, notations, preliminary definitions, and fundamental quantities in bra-ket matrices must be set in place in order to alleviate the inconsistent semantics between LMO EDA and HALMO EDA and to use bra-ket matrices in lieu of summations as much as possible. Einstein notation is never used, so any summation is always explicit.

4.2 Orbital Indexing and Optimization

In EDA, it is necessary to distinguish the different quantum states of the molecular orbitals. For this work, the following sets of spatial-orbital indices correspond to various quantum states.

- $\tilde{X}$ is the set of indices over spatial orbitals of the supermolecule where the molecular orbitals are variationally optimized within their respective fragments in isolation of other fragments.
- $X*$ is the set of indices over spatial orbitals of the supermolecule where the molecular orbitals were first variationally optimized within their respective fragments in isolation of other fragments and are then orthonormalized across the supermolecule.
- $\widehat{X}$ is the set of indices over spatial orbitals of the supermolecule where the molecular orbitals are SCF-MI optimized (discussed in §6).
- X is the set of indices over spatial orbitals of the supermolecule where the molecular orbitals are expanded in all basis functions and are variationally optimized across the supermolecule.
- Ω is a set of indices over spatial orbitals of the supermolecule.
- $\mathrm{F}(i)$ is the set of indices over the spatial orbitals localized to the same fragment that the spatial orbital corresponding to index i is localized to (discussed in §4.3).

Adapted from Su and Li [14], the star, $*$, distinguishes the different variational optimizations and does not denote a power set. Based on the definitions above, $\mathrm{F}(\Omega)$ is a mathematically valid expression of an image of F over Ω:

$$\mathrm{F}(\Omega) = \{\mathrm{F}(i) \mid i \in \Omega\} \tag{4.2.1}$$

When indexing over spatial orbitals from Ω, the index itself contains information on how the spin orbitals are variationally optimized and is applied to the spatial orbital in question. For instance, whether ψ_i is variationally optimized within its fragment or across the supermolecule depends on the set of indices Ω that i is iterating over.

4.3 Localized and Delocalized Molecular Orbitals

An orbital localized to a fragment is an orbital that is expanded in terms of the basis functions of the fragment only. Localized molecular orbitals are important in BSSE,

which are corrected in different ways in different EDA schemes. Expansion of a molecular orbital, $|\psi_J\rangle$, in terms of the basis functions that are localized to a particular fragment, J, is

$$|\psi_J\rangle = \sum_{i=1}^{N_\phi^J} |\phi_{Ji}\rangle\, m_{Ji} \tag{4.3.1a}$$

$$= \mathbf{\Phi}_J \mathbf{m}_J \tag{4.3.1b}$$

where N_ϕ^J is the number of basis functions belonging to J, $|\phi_{Ji}\rangle$ is the i-th basis function belonging to J, and m_{Ji} is the expansion coefficient for $|\phi_{Ji}\rangle$. By extension, the molecular orbitals, $\mathbf{\Psi}_J$, localized to J is

$$\mathbf{\Psi}_J = \mathbf{\Phi}_J \begin{pmatrix} \mathbf{m}_{J,1} & \mathbf{m}_{J,2} & \cdots & \mathbf{m}_{J,N_\psi^J} \end{pmatrix} \tag{4.3.2a}$$

$$= \mathbf{\Phi}_J \mathbf{M}_J \tag{4.3.2b}$$

where the number of molecular orbitals localized to J is $N_\psi^J \leq N_\phi^J$. An alternative definition can be made as $\mathbf{\Psi}_J = \mathbf{\Phi}\mathbf{M}_J$ using the basis functions across the supermolecule but with zero coefficients in $\mathbf{M}_J$ when the corresponding basis function is not in J. For this definition, the number of rows in $\mathbf{M}_J$ would be $\sum_{i=1}^{N_\text{frag}} N_\phi^i$ in an N_frag-fragment system. The presence of either $\mathbf{\Phi}_J$ or $\mathbf{\Phi}$ distinguishes the two definitions and defines the size of $\mathbf{M}_J$.

For specifying the localized molecular orbitals of the supermolecule, the ket matrix of all molecular orbitals expanded only in terms of the basis functions localized to their respective fragments can be compactly written as

$$\mathbf{\Psi}_{\tilde{X}} = \begin{pmatrix} \mathbf{\Phi}_A\mathbf{M}_A & \mathbf{\Phi}_B\mathbf{M}_B & \cdots \end{pmatrix} \tag{4.3.3a}$$

$$= \begin{pmatrix} \mathbf{\Phi}_A & \mathbf{\Phi}_B & \cdots \end{pmatrix} \begin{pmatrix} \mathbf{M}_A & \mathbf{0} & \cdots \\ \mathbf{0} & \mathbf{M}_B & \cdots \\ \vdots & \vdots & \ddots \end{pmatrix} \tag{4.3.3b}$$

$$= \mathbf{\Phi}\mathbf{M}_{\tilde{X}} \tag{4.3.3c}$$

with the definition of $\mathbf{M}_{\tilde{X}}$. Note that the ordering of the elements of $\mathbf{\Phi}$ and $\mathbf{\Psi}$ are implicitly dictated, respectively, by the ordering of the rows and columns of $\mathbf{M}_{\tilde{X}}$.

A delocalized molecular orbital is a molecular orbital that is expanded in terms of basis functions from all fragments. The expansion-coefficient matrix of a delocalized molecular orbital is not block diagonal and takes on the form as

$$\mathbf{M}_{\tilde{X}} = \begin{pmatrix} \mathbf{M}_A & \mathbf{M}_B & \cdots \end{pmatrix} \tag{4.3.4}$$

where the number of rows of $\mathbf{M}_J$ for $\forall J \in \mathrm{F}(\tilde{X})$ is the number of basis functions from all fragments and represents the delocalized nature of the molecular orbitals of the fragments. Unlike a localized molecular orbital, the expansion coefficient of a delocalized molecular orbital can be nonzero for a basis function from a different fragment.

Since $\tilde{X}$ itself does not make the distinction whether molecular orbitals are localized or not (cf. 4.2), $\mathbf{\Psi}_J$ can be molecular orbitals of a fragment that are either all localized or all delocalized. In turn, this can make $\mathbf{M}_{\tilde{X}}$ either block diagonal or not. The lack of notational difference between the two originates from whether BSSE is corrected in LMO EDA, and a common and agnostic notation is preferred. As such, the context should make it clear as to whether the molecular orbitals are localized in a particular method that is being employed.

4.4 Energies of Quantum States

EDA decomposes the interaction energy through the use of various intermediate wave functions, each of which represents a particular quantum state of the system. The state of a system is denoted by the letter Ψ without boldface. Since a ket matrix of spatial orbitals uses the same letter as that of a quantum state, the spatial orbitals of such ket row matrix would correspond to the quantum state denoted by the same, but not boldfaced, symbol for a spin function.

The energy functional due to kinetic energy, electron-electron Coulombic repulsion, and nucleus-nucleus repulsion is collectively denoted as E_{cl} and is considered to be the classical-like terms of the Kohn-Sham energy. The exchange and correlation functionals

are denoted as E_x and E_c, respectively. The total energy functional, then, is

$$E\left[\Psi\right] = E_\mathrm{cl}\left[\Psi\right] + E_\mathrm{x}\left[\Psi\right] + E_\mathrm{c}\left[\Psi\right] \tag{4.4.1}$$

4.4.1 State of a Fragment

The state of a fragment J with optimized orbitals in isolation of other fragments is represented by Ψ_J. Ψ_J implies that J must be a member in $\mathrm{F}(\tilde{X})$ when J is iterating over the fragments of the supermolecule.

The classical-like part of the energy functional of Ψ_J is

$$E_\mathrm{cl}\left[\Psi_J\right] = \sum_{i\in J} \mathfrak{f}_i \left\langle \chi_i \middle| \hat{h}(i) \middle| \chi_i \right\rangle + \frac{1}{2} \sum_{\omega\in\{\alpha,\beta\}} \sum_{i,j\in J} f_i f_j \left\langle \psi_i^\omega \psi_j^\omega \middle| \psi_i^\omega \psi_j^\omega \right\rangle + E_J^\mathrm{nuc} \tag{4.4.2a}$$

$$= \sum_{\omega\in\{\alpha,\beta\}} \mathrm{tr}\left(\mathbf{f}_J^\omega \mathbf{\Psi}_J^{\omega\dagger} \hat{h} \mathbf{\Psi}_J^\omega\right) + \frac{1}{2} \sum_{\omega\in\{\alpha,\beta\}} \mathrm{tr}\left(\left(\mathbf{f}_J \otimes_\mathrm{Kron} \mathbf{f}_J\right) \check{\mathbf{\Psi}}_J^\dagger \check{\mathbf{\Psi}}_J\right) + E_J^\mathrm{nuc} \tag{4.4.2b}$$

$$= \sum_{\omega\in\{\alpha,\beta\}} \mathrm{tr}\left(\mathbf{K}_J^\omega \mathbf{\Phi}_{\tilde{\xi}}^\dagger \hat{h} \mathbf{\Phi}_{\tilde{\xi}}\right) + \frac{1}{2} \sum_{\omega\in\{\alpha,\beta\}} \mathrm{tr}\left(\left(\mathbf{K}_J \otimes_\mathrm{Kron} \mathbf{K}_J\right) \check{\mathbf{\Phi}}_{\tilde{\xi}}^\dagger \check{\mathbf{\Phi}}_{\tilde{\xi}}\right) + E_J^\mathrm{nuc} \tag{4.4.2c}$$

where

$$\mathbf{\Phi}_{\tilde{\xi}} = \begin{cases} \mathbf{\Phi}_J & \text{molecular orbitals are localized} \\ \mathbf{\Phi} & \text{molecular orbitals are delocalized} \end{cases} \tag{4.4.3}$$

For the non-classical parts of the energy, the exchange and correlation functionals are simply rewritten in terms of the fragment's electron density n_J^ω for a spin function ω (cf. (2.2.12)) as

$$E_\mathrm{x}\left[\Psi_J\right] = \sum_{\omega\in\{\alpha,\beta\}} E_\mathrm{x}\left[n_J^\omega\right] \tag{4.4.4a}$$

$$E_\mathrm{c}\left[\Psi_J\right] = \sum_{\omega\in\{\alpha,\beta\}} E_\mathrm{c}\left[n_J^\omega\right] \tag{4.4.4b}$$

4.4.2 States of the Supermolecule

The state of the supermolecule differs depending on how the orbitals are optimized and whether molecular orbitals are orthonormal. In contrast to a fragment in isolation, $\Psi_{\tilde{X}}$

is not the same as Ψ_{X*}, since the fragments are now collectively considered as members of the supermolecule. Similar to a fragment in isolation, $E_\Omega^{\text{nuc}} = E_X^{\text{nuc}}$ regardless of Ω (which is generic as to the quantum state of the supermolecule, cf. §4.2), since only the electron orbitals differ.

The classical-like part of the energy functional of Ψ_Ω is

$$E_{\text{cl}}[\Psi_\Omega] = \sum_{i\in\Omega} \mathfrak{f}_i \left\langle \chi_i \middle| \hat{h}(i) \middle| \chi_i \right\rangle + \frac{1}{2} \sum_{\omega\in\{\alpha,\beta\}} \sum_{i,j\in\Omega} f_i f_j \left\langle \psi_i^\omega \psi_j^\omega \middle| \psi_i^\omega \psi_j^\omega \right\rangle + E_X^{\text{nuc}} \tag{4.4.5a}$$

$$= \sum_{\omega\in\{\alpha,\beta\}} \text{tr}\left(\mathbf{f}_\Omega^\omega \mathbf{\Psi}_\Omega^{\omega\dagger} \hat{h} \mathbf{\Psi}_\Omega^\omega \right) + \frac{1}{2} \sum_{\omega\in\{\alpha,\beta\}} \text{tr}\left(\left(\mathbf{f}_\Omega \otimes_{\text{Kron}} \mathbf{f}_\Omega \right) \check{\mathbf{\Psi}}_\Omega^\dagger \check{\mathbf{\Psi}}_\Omega \right) + E_X^{\text{nuc}} \tag{4.4.5b}$$

$$= \sum_{\omega\in\{\alpha,\beta\}} \text{tr}\left(\mathbf{K}_\Omega^\omega \mathbf{\Phi}^\dagger \hat{h} \mathbf{\Phi} \right) + \frac{1}{2} \sum_{\omega\in\{\alpha,\beta\}} \text{tr}\left(\left(\mathbf{K}_\Omega \otimes_{\text{Kron}} \mathbf{K}_\Omega \right) \check{\mathbf{\Phi}}^\dagger \check{\mathbf{\Phi}} \right) + E_X^{\text{nuc}} \tag{4.4.5c}$$

Exchange and correlation functionals for the supermolecule are

$$E_{\text{x}}[\Psi_\Omega] = \sum_{\omega\in\{\alpha,\beta\}} E_{\text{x}}[n_\Omega^\omega] \tag{4.4.6a}$$

$$E_{\text{c}}[\Psi_\Omega] = \sum_{\omega\in\{\alpha,\beta\}} E_{\text{c}}[n_\Omega^\omega] \tag{4.4.6b}$$

The generic density kernel, $\mathbf{K}_\Omega$, will now be defined in turn for $\Omega \in \{\tilde{X}, X*, X\}$. $\Omega = \widehat{X}$ is SCF MI and is discussed in §6.

The density kernel for the supermolecule state with nonorthogonal molecular orbitals ($\Omega = \tilde{X}$) is

$$\mathbf{K}_{\tilde{X}} = \mathbf{M}_{\tilde{X}} \mathbf{f}_{\tilde{X}} \mathbf{M}_{\tilde{X}}^\dagger \tag{4.4.7}$$

and is called the nonorthogonal supermolecule density kernel. The occupation numbers from the individual fragments are collected as

$$\mathbf{f}_{\tilde{X}} = \begin{pmatrix} \mathbf{f}_A & \mathbf{0} & \cdots \\ \mathbf{0} & \mathbf{f}_B & \cdots \\ \vdots & \vdots & \ddots \end{pmatrix} \tag{4.4.8}$$

In the special case that the molecular orbitals are localized, the nonorthogonal supermolecule density kernel is the superposition of the fragment density kernels, $\mathbf{K}_J = \mathbf{M}_J \mathbf{f}_J \mathbf{M}_J^\dagger$, along the diagonal:

$$\mathbf{K}_{\tilde{X}} = \begin{pmatrix} \mathbf{K}_A & \mathbf{0} & \cdots \\ \mathbf{0} & \mathbf{K}_B & \cdots \\ \vdots & \vdots & \ddots \end{pmatrix} \tag{4.4.9}$$

The density kernel for the supermolecule state with orthonormal molecular orbitals ($\Omega = X*$) is

$$\mathbf{K}_{X*} = \mathbf{M}_{X*} \mathbf{f}_{\tilde{X}} \mathbf{M}_{X*}^\dagger \tag{4.4.10}$$

and is called the orthonormal supermolecule density kernel [19] that is constructed from orthonormal molecular orbitals with the same occupation numbers as that of the quantum state $\Psi_{\tilde{X}}$. In LMO EDA and in the original implementation of HALMO EDA of ONETEP, symmetrical orthogonalization (SO) is used, which would make

$$\mathbf{M}_{X*} = \mathbf{M}_{\tilde{X}} \boldsymbol{\sigma}_{\tilde{X}}^{-\frac{1}{2}} \tag{4.4.11}$$

and

$$\mathbf{K}_{X*} = \mathbf{M}_{\tilde{X}} \boldsymbol{\sigma}_{\tilde{X}}^{-\frac{1}{2}} \mathbf{f}_{\tilde{X}} \boldsymbol{\sigma}_{\tilde{X}}^{-\frac{1}{2}} \mathbf{M}_{\tilde{X}}^\dagger \tag{4.4.12}$$

where $\mathbf{S} = \boldsymbol{\Phi}^\dagger \boldsymbol{\Phi}$ is the overlap matrix of basis functions (from all fragments), and $\sigma_{\tilde{X}} = \boldsymbol{\Psi}_{\tilde{X}}^\dagger \boldsymbol{\Psi}_{\tilde{X}} = \mathbf{M}_{\tilde{X}}^\dagger \mathbf{S} \mathbf{M}_{\tilde{X}}$ is the overlap matrix of nonorthogonal molecular orbitals.

The density kernel for the supermolecule state with optimized delocalized molecular orbitals ($\Omega = X$) is

$$\mathbf{K}_X = \mathbf{M}_X \mathbf{f}_X \mathbf{M}_X^\dagger \tag{4.4.13}$$

and is called the delocalized supermolecule density kernel. It is the state where the molecular orbitals are expanded in terms of the basis functions from all fragments (i.e.,

delocalized molecular orbitals) and are variationally optimized across the entire supermolecule with its own occupation numbers (i.e., $\mathbf{f}_X \neq \mathbf{f}_{\bar{X}}$).

4.5 Schemes Relevant to ONETEP

In this section, only the EDA schemes relevant to this work are discussed. The relevant schemes are LMO [14], HALMO [19], and the newly developed CLMO.

4.5.1 LMO EDA

The decomposition of interaction energy, ΔE_{int}, into LMO-EDA components (Figure 4.1) is

$$\Delta E_{\text{int}} = \Delta E_{\text{ele}}^{\text{LMO}} + \Delta E_{\text{ex}}^{\text{LMO}} + \Delta E_{\text{rep}}^{\text{LMO}} + \Delta E_{\text{pol}}^{\text{LMO}} + \Delta E_{\text{disp}}^{\text{LMO}} \tag{4.5.1}$$

Each component is defined as the energy difference between two intermediate quantum states (cf. §4.4). Energy decomposition with localized molecular orbitals for the fragments is always performed. If BSSE correction is requested, a second energy decomposition is done with delocalized molecular orbitals for the fragments. The BSSE-corrected decomposition results in all EDA components being corrected, since delocalized molecular orbitals are used in lieu of localized molecular orbitals throughout the decomposition as a counterpoise method. The BSSE-uncorrected decomposition can then be compared with the BSSE-corrected one to inspect the changes in the EDA components due to BSSE. In the BSSE-uncorrected decomposition, $\mathbf{M}_{\bar{X}}$ is block diagonal (4.3.3c). In the BSSE-corrected decomposition, $\mathbf{M}_{\tilde{X}}$ is not block diagonal (4.3.4). The following definitions of LMO-EDA components are agnostic to whether BSSE correction is performed.

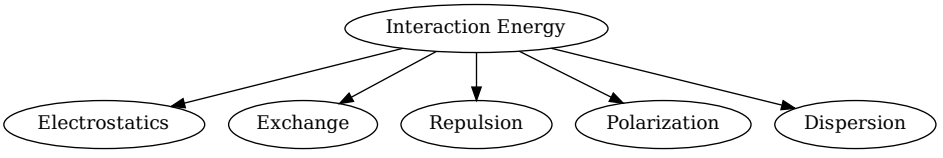

FIGURE 4.1: Decomposition of interaction energy in LMO EDA.

The electrostatics component is the change in classical-like terms of the KS energy containing kinetic energy, electron-electron Coulombic repulsion, and nucleus-nucleus repulsion when going from isolated fragments to the supermolecule without orbital orthonormalization. It is defined as

$$\Delta E_{\text{ele}}^{\text{LMO}} = E_{\text{cl}}\left[\Psi_{\tilde{X}}\right] - \sum_{J \in \text{F}(\tilde{X})} E_{\text{cl}}\left[\Psi_J\right] \tag{4.5.2}$$

In Su and Li [14], the one-electron Hamiltonians in the respective E_{cl} terms are canceled out by mistake.

The exchange component is the change in exchange energy when going from isolated fragments to the supermolecule without orbital orthonormalization. It is defined as

$$\Delta E_{\text{ex}}^{\text{LMO}} = E_{\text{x}}\left[\Psi_{\tilde{X}}\right] - \sum_{J \in \text{F}(\tilde{X})} E_{\text{x}}\left[\Psi_J\right] \tag{4.5.3}$$

The repulsion component is the change in energy upon orbital orthonormalization excluding correlation. It is defined as

$$\Delta E_{\text{rep}}^{\text{LMO}} = \left(E_{\text{cl}}\left[\Psi_{X*}\right] + E_{\text{x}}\left[\Psi_{X*}\right]\right) - \left(E_{\text{cl}}\left[\Psi_{\tilde{X}}\right] + E_{\text{x}}\left[\Psi_{\tilde{X}}\right]\right) \tag{4.5.4}$$

The LMO polarization component is the change in energy when going from the supermolecule with orthonormal molecular orbitals to the supermolecule with optimized delocalized molecular orbitals excluding correlation. It is not to be confused with the HALMO polarization (discussed in §4.5.2).

$$\Delta E_{\text{pol}}^{\text{LMO}} = \left(E_{\text{cl}}\left[\Psi_X\right] + E_{\text{x}}\left[\Psi_X\right]\right) - \left(E_{\text{cl}}\left[\Psi_{X*}\right] + E_{\text{x}}\left[\Psi_{X*}\right]\right) \tag{4.5.5}$$

The dispersion component is the change in correlation energy when going from isolated fragments to the supermolecule with optimized delocalized molecular orbitals. It is defined as

$$\Delta E_{\text{disp}}^{\text{LMO}} = E_{\text{c}}\left[\Psi_X\right] - \sum_{J \in \text{F}(\tilde{X})} E_{\text{c}}\left[\Psi_J\right] \tag{4.5.6}$$

and does not have a corresponding component in HALMO EDA (cf. §4.5.2).

4.5.2 HALMO EDA

HALMO EDA decomposes the interacting energy of a system into three main components: frozen density, polarization, and charge transfer. Further decomposition of the frozen-density contribution is based on (but not equivalent to) LMO EDA. The decomposition of the interaction energy, ΔE_{int}, into HALMO-EDA components (Figure 4.2) is

$$\Delta E_{\text{int}} = \Delta E_{\text{frz}}^{\text{HALMO}} + \Delta E_{\text{pol}}^{\text{HALMO}} + \Delta E_{\text{ct}}^{\text{HALMO}} \tag{4.5.7}$$

where frozen density is decomposed as

$$\Delta E_{\text{frz}}^{\text{HALMO}} = \Delta E_{\text{es}}^{\text{HALMO}} + \Delta E_{\text{ex}}^{\text{HALMO}} + \Delta E_{\text{rep}}^{\text{HALMO}} + \Delta E_{\text{corr}}^{\text{HALMO}} \tag{4.5.8}$$

and charge transfer is separated into a delocalization term and BSSE correction. As for LMO EDA, each HALMO-EDA component is defined as the energy difference between two intermediate quantum states (cf. §4.4). When possible, a HALMO-EDA component will be expressed in terms of the corresponding or analogous LMO-EDA component. In HALMO EDA, molecular orbitals are always localized for the fragments regardless of whether BSSE is corrected, making $\mathbf{M}_{\tilde{X}}$ always block diagonal (4.3.3c).

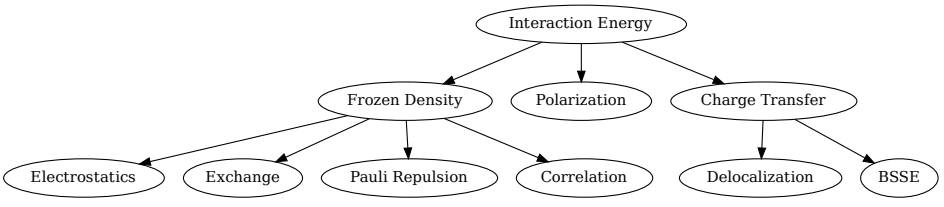

FIGURE 4.2: Decomposition of interaction energy in HALMO EDA.

The electrostatics, exchange, and Pauli-repulsion components are defined to be equal to the corresponding components in LMO EDA with localized molecular orbitals, respectively as $\Delta E_{\text{es}}^{\text{HALMO}} = \Delta E_{\text{ele}}^{\text{LMO}}$, $\Delta E_{\text{ex}}^{\text{HALMO}} = \Delta E_{\text{ex}}^{\text{LMO}}$, and $\Delta E_{\text{rep}}^{\text{HALMO}} = \Delta E_{\text{rep}}^{\text{LMO}}$. Despite the different names, HALMO Pauli repulsion is the same as LMO repulsion.

The correlation component is the change in correlation energy when going from isolated fragments to the supermolecule with orthonormal molecular orbitals. It is defined as

$$\Delta E_{\text{corr}}^{\text{HALMO}} = E_{\text{c}}\left[\Psi_{X*}\right] - \sum_{J \in \text{F}(\tilde{X})} E_{\text{c}}\left[\Psi_{J}\right] \tag{4.5.9}$$

In terms of LMO dispersion with localized molecular orbitals for the isolated fragments (4.5.6), HALMO correlation is equivalent to

$$\Delta E_{\text{corr}}^{\text{HALMO}} = \Delta E_{\text{disp}}^{\text{LMO}} + \left(E_{\text{c}}\left[\Psi_{X*}\right] - E_{\text{c}}\left[\Psi_{X}\right]\right) \tag{4.5.10}$$

The HALMO polarization component is the change in energy when going from the supermolecule with orthonormal molecular orbitals to the supermolecule with SCF-MI optimized molecular orbitals (discussed in §6). It is not to be confused with LMO polarization (4.5.5), which is a fundamentally different EDA component. HALMO polarization is defined as

$$\Delta E_{\text{pol}}^{\text{HALMO}} = E\left[\Psi_{\widehat{X}}\right] - E\left[\Psi_{X*}\right] \tag{4.5.11}$$

The charge-transfer component is the change in energy when going from the supermolecule with SCF-MI optimized molecular orbitals to the supermolecule with optimized delocalized molecular orbitals. LMO EDA ignores charge-transfer effects and, hence, has no counterpart. It is defined as

$$\Delta E_{\text{ct}}^{\text{HALMO}} = \Delta E_{\text{deloc}}^{\text{HALMO}} + \Delta E^{\text{BSSE}} \tag{4.5.12}$$

where

$$\Delta E_{\text{deloc}}^{\text{HALMO}} = E\left[\Psi_{X}\right] - E\left[\Psi_{\widehat{X}}\right] \tag{4.5.13}$$

is the delocalization term, and ΔE^{BSSE} is BSSE correction. If no BSSE correction is requested, ΔE^{BSSE} is treated as 0. The BSSE correction is added as part of charge transfer

as opposed to other components, since BSSE results from the delocalization of molecular orbitals of the fragments when the basis functions of other fragments are included. In ONETEP, BSSE is eliminated [20], so the delocalization term is effectively the charge transfer in ONETEP's implementation of HALMO EDA.

4.5.3 CLMO EDA

4.5.3.1 Formulation

CLMO (Combined Localized Molecular Orbitals) is an EDA scheme that is compatibly based on LMO EDA (discussed in §4.5.1) with the modification made in this work that segregates and incorporates BSSE corrections into the polarization and dispersion terms of LMO EDA. LMO EDA performs two energy decompositions to correct all of its components for BSSE. Interpreting the resulting two sets of LMO-EDA components is not intuitive, since the BSSE correction is spread across all components by using delocalized molecular orbitals for the fragments at the start of the BSSE-corrected energy decomposition. In CLMO EDA, the two sets of LMO-EDA components are combined into one by using localized molecular orbitals for the fragments and incorporating two separate BSSE corrections into the polarization and dispersion components. Unlike LMO EDA, CLMO EDA produces only one energy decomposition with localized molecular orbitals for the fragments, regardless of whether BSSE correction is requested.

The decomposition of interaction energy, ΔE_{int}, into CLMO-EDA components (Figure 4.3) is

$$\Delta E_{\text{int}} = \Delta E_{\text{ele}}^{\text{CLMO}} + \Delta E_{\text{ex}}^{\text{CLMO}} + \Delta E_{\text{rep}}^{\text{CLMO}} + \Delta E_{\text{pol}}^{\text{CLMO}} + \Delta E_{\text{disp}}^{\text{CLMO}} \tag{4.5.14}$$

where all components are the same as the BSSE-uncorrected LMO-EDA components except polarization and dispersion. CLMO dispersion is the same as BSSE-corrected LMO dispersion. However, CLMO polarization is not the same as BSSE-corrected LMO polarization. The difference is due to BSSE-corrected LMO polarization not including the BSSE corrections to electrostatics, exchange, and repulsion, whereas CLMO polarization does.

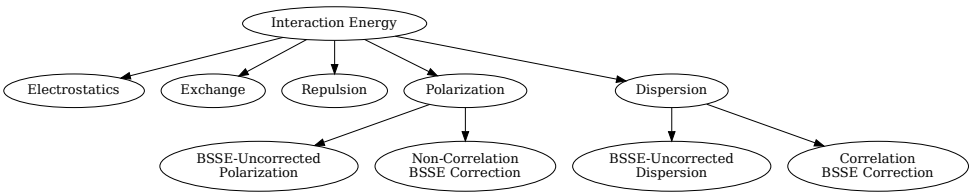

FIGURE 4.3: Decomposition of interaction energy in CLMO EDA.

The CLMO decomposition first follows the same route as that of BSSE-uncorrected LMO EDA. Two BSSE corrections are then computed: one for the interaction energy, and the other for the dispersion component. Inspecting (4.5.6), the BSSE correction for the dispersion component is actually the BSSE correction for correlation energy. The BSSE correction for the classical-like and exchange (i.e., non-correlation) parts of the interaction energy is simply the BSSE correction for the interaction energy minus the BSSE correction for the dispersion component, and it becomes the BSSE correction that is incorporated in CLMO polarization.

The CLMO-EDA components can be derived solely from BSSE-uncorrected and BSSE-corrected LMO-EDA components. CLMO electrostatics, exchange, and repulsion are the same as in the BSSE-uncorrected LMO EDA:

$$\Delta E_{\text{ele}}^{\text{CLMO}} = \Delta E_{\text{ele}}^{\text{LMO}} \tag{4.5.15a}$$

$$\Delta E_{\text{ex}}^{\text{CLMO}} = \Delta E_{\text{ex}}^{\text{LMO}} \tag{4.5.15b}$$

$$\Delta E_{\text{rep}}^{\text{CLMO}} = \Delta E_{\text{rep}}^{\text{LMO}} \tag{4.5.15c}$$

On the other hand, CLMO dispersion is equivalent to the BSSE-corrected LMO dispersion:

$$\Delta E_{\text{disp}}^{\text{CLMO}} = \left(\Delta E_{\text{disp}}^{\text{LMO}}\right)^{\text{CP}} \tag{4.5.16a}$$

$$= \Delta E_{\text{disp}}^{\text{LMO}} + \Delta E_{\text{c}}^{\text{BSSE}} \tag{4.5.16b}$$

where $\Delta E_{\text{c}}^{\text{BSSE}}$ is the BSSE correction to the correlation energy (using the counterpoise method in LMO EDA). Unlike other CLMO components, CLMO polarization has no

direct counterpart in LMO EDA but can be defined in terms of BSSE-uncorrected LMO polarization as

$$\Delta E_{\text{pol}}^{\text{CLMO}} = \Delta E_{\text{pol}}^{\text{LMO}} + \Delta E_{\text{nc}}^{\text{BSSE}} \tag{4.5.17}$$

where

$$\Delta E_{\text{nc}}^{\text{BSSE}} = \Delta E^{\text{BSSE}} - \Delta E_{\text{c}}^{\text{BSSE}} \tag{4.5.18}$$

is the BSSE correction to the non-correlation parts of the interaction energy. $\Delta E_{\text{nc}}^{\text{BSSE}}$ is equivalent to the sum of the BSSE corrections to all components except dispersion in LMO EDA. As such, it is important to note that $\Delta E_{\text{pol}}^{\text{CLMO}} \neq \left(\Delta E_{\text{pol}}^{\text{LMO}}\right)^{\text{CP}}$, since $\left(\Delta E_{\text{pol}}^{\text{LMO}}\right)^{\text{CP}}$ excludes BSSE corrections to other non-correlation EDA components.

CLMO EDA has been implemented alongside ONETEP. Since ONETEP does not exhibit BSSE [9], CLMO EDA with ONETEP is effectively LMO EDA with localized molecular orbitals for the fragments. For GAMESS-US, CLMO-EDA components are derived from BSSE-uncorrected and BSSE-corrected LMO EDA, and are used in lieu of LMO-EDA components in this work. CLMO-EDA components contain essentially the same information as that of LMO EDA except that the individual BSSE corrections to electrostatics, exchange, and repulsion are lost by merging into the polarization term. The trade-off for such minor loss of information is that there is only one set of EDA components with a more intuitive interpretability of BSSE.

CLMO EDA with ONETEP presents some important capabilities and novel possibilities compared to the implementation of LMO EDA in GAMESS-US by Su and Li [14]. GAMESS-US is a cubic-scaling software package. Despite the conceptual simplicity of LMO EDA, GAMESS-US LMO EDA poses difficulties when applied to systems of only around 100 atoms. On the other hand, ONETEP is linear scaling, and CLMO EDA maintains the conceptual simplicity of LMO EDA. As mentioned, since ONETEP does not exhibit BSSE, running CLMO EDA with ONETEP is essentially running LMO EDA but with linear-scaling computational costs instead. The implementation was validated by comparing with GAMESS-US LMO EDA in Appendix A.

4.6 Linear-Scaling Orthogonalization of Molecular Orbitals

Constructing $\mathbf{K}_{X*}$ from $\mathbf{K}_{\tilde{X}}$ usual begins with solving for the expansion coefficients as an eigenvalue problem for each fragment J:

$$\mathbf{K}_J \mathbf{S}_J \mathbf{M}_J = \mathbf{M}_J \mathbf{f}_J \tag{4.6.1}$$

where $\mathbf{S}_J = \mathbf{\Phi}_J^\dagger \mathbf{\Phi}_J$. The expansion-coefficient matrices and occupation numbers can then be used in forming $\mathbf{K}_{X*}$. The disadvantage of this method is that it requires diagonalization, which is cubic scaling. An alternative, linear-scaling approach can be used in constructing $\mathbf{K}_{X*}$ from $\mathbf{K}_{\tilde{X}}$ for a ground-state system, since $\mathbf{f}_J$ becomes an identity matrix when the unoccupied molecular orbitals are removed.

The linear-scaling alternative is an indirect method that uses McWeeny purification [30]. It was implemented in ONETEP by Phipps et al. [19], but no proof or justification was offered as to why this linear-scaling method of orthogonalizing molecular orbitals should work. For this present work, a mathematical proof for it is developed.

From (2.2.56) and letting $\widetilde{\mathbf{K}}_0 \equiv \mathbf{K}_{\tilde{X}}$,

$$\widetilde{\mathbf{K}}_1 = 3\widetilde{\mathbf{K}}_0 \mathbf{S} \widetilde{\mathbf{K}}_0 - 2\widetilde{\mathbf{K}}_0 \mathbf{S} \widetilde{\mathbf{K}}_0 \mathbf{S} \widetilde{\mathbf{K}}_0 \tag{4.6.2a}$$

$$= \mathbf{M}_{\tilde{X}} \left(3\sigma_{\tilde{X}} - 2\sigma_{\tilde{X}}\sigma_{\tilde{X}}\right) \mathbf{M}_{\tilde{X}}^\dagger \tag{4.6.2b}$$

$$= \mathbf{M}_{\tilde{X}} \mathbf{W}_0 \mathbf{M}_{\tilde{X}}^\dagger \tag{4.6.2c}$$

where $\mathbf{S} = \mathbf{\Phi}^\dagger \mathbf{\Phi}$, and $\sigma_{\tilde{X}} = \mathbf{\Psi}_{\tilde{X}}^\dagger \mathbf{\Psi}_{\tilde{X}}$. Repeated application of McWeeny purification yields a pattern:

$$\widetilde{\mathbf{K}}_{n+1} = \mathbf{M}_{\tilde{X}} \mathbf{W}_n \mathbf{M}_{\tilde{X}}^\dagger \tag{4.6.3a}$$

$$\mathbf{W}_0 = 3\sigma_{\tilde{X}} - 2\sigma_{\tilde{X}}\sigma_{\tilde{X}} \tag{4.6.3b}$$

$$\mathbf{W}_{n+1} = 3\mathbf{W}_n \sigma_{\tilde{X}} \mathbf{W}_n - 2\mathbf{W}_n \sigma_{\tilde{X}} \mathbf{W}_n \sigma_{\tilde{X}} \mathbf{W}_n \tag{4.6.3c}$$

for $n \geq 0$. Proof by mathematical induction is used. Assume (4.6.3) is true for $\widetilde{\mathbf{K}}_\xi$. Applying McWeeny purification on $\widetilde{\mathbf{K}}_\xi$ gives

$$\widetilde{\mathbf{K}}_{\xi+1} = 3\widetilde{\mathbf{K}}_\xi \mathbf{S} \widetilde{\mathbf{K}}_\xi - 2\widetilde{\mathbf{K}}_\xi \mathbf{S} \widetilde{\mathbf{K}}_\xi \mathbf{S} \widetilde{\mathbf{K}}_\xi \tag{4.6.4a}$$

$$= \mathbf{M}_{\tilde{X}} \left(3\mathbf{W}_{\xi-1} \boldsymbol{\sigma}_{\tilde{X}} \mathbf{W}_{\xi-1} - 2\mathbf{W}_{\xi-1} \boldsymbol{\sigma}_{\tilde{X}} \mathbf{W}_{\xi-1} \boldsymbol{\sigma}_{\tilde{X}} \mathbf{W}_{\xi-1} \right) \mathbf{M}_{\tilde{X}}^\dagger \tag{4.6.4b}$$

$$= \mathbf{M}_{\tilde{X}} \mathbf{W}_\xi \mathbf{M}_{\tilde{X}}^\dagger \tag{4.6.4c}$$

From (4.6.2c) and since (4.6.4c) is true for $\xi = 1$, (4.6.3) is true for $n \geq 0$. Let $\mathbf{K}_{\text{pure}} = \mathbf{M}_{\tilde{X}} \mathbf{W}_{\text{pure}} \mathbf{M}_{\tilde{X}}^\dagger$ when $n \to \infty$ in (4.6.3). $\mathbf{K}_{\text{pure}}$ would then satisfy the idempotency condition:

$$\mathbf{K}_{\text{pure}} \mathbf{S} \mathbf{K}_{\text{pure}} = \mathbf{K}_{\text{pure}} \tag{4.6.5a}$$

$$\mathbf{M}_{\tilde{X}} \mathbf{W}_{\text{pure}} \boldsymbol{\sigma}_{\tilde{X}} \mathbf{W}_{\text{pure}} \mathbf{M}_{\tilde{X}}^\dagger = \mathbf{M}_{\tilde{X}} \mathbf{W}_{\text{pure}} \mathbf{M}_{\tilde{X}}^\dagger \tag{4.6.5b}$$

Since (4.6.5) must hold true for any $\mathbf{M}_{\tilde{X}}$,

$$\mathbf{W}_{\text{pure}} \boldsymbol{\sigma}_{\tilde{X}} \mathbf{W}_{\text{pure}} = \mathbf{W}_{\text{pure}} \tag{4.6.6}$$

The invertibility of $\mathbf{W}_{\text{pure}}$ is not apparent at this point. However, (4.6.6) can be rewritten as

$$\mathbf{W}_{\text{pure}} \boldsymbol{\sigma}_{\tilde{X}} \mathbf{W}_{\text{pure}} = \left(\mathbf{W}_{\text{pure}} \boldsymbol{\sigma}_{\tilde{X}} \mathbf{W}_{\text{pure}} \right) \boldsymbol{\sigma}_{\tilde{X}} \mathbf{W}_{\text{pure}} \tag{4.6.7a}$$

$$\mathbf{W}_{\text{pure}} \left(\boldsymbol{\sigma}_{\tilde{X}} - \boldsymbol{\sigma}_{\tilde{X}} \mathbf{W}_{\text{pure}} \boldsymbol{\sigma}_{\tilde{X}} \right) \mathbf{W}_{\text{pure}} = \mathbf{0} \tag{4.6.7b}$$

Since $\mathbf{W}_{\text{pure}} \neq \mathbf{0}$,

$$\boldsymbol{\sigma}_{\tilde{X}} = \boldsymbol{\sigma}_{\tilde{X}} \mathbf{W}_{\text{pure}} \boldsymbol{\sigma}_{\tilde{X}} \tag{4.6.8}$$

$\boldsymbol{\sigma}_{\tilde{X}}$ is assumed to be invertible. As such, $\mathbf{W}_{\text{pure}}$ must also be invertible:

$$\boldsymbol{\sigma}_{\tilde{X}}^{-1} = \boldsymbol{\sigma}_{\tilde{X}}^{-1} \mathbf{W}_{\text{pure}}^{-1} \boldsymbol{\sigma}_{\tilde{X}}^{-1} \tag{4.6.9}$$

Therefore,

$$\mathbf{W}_{\text{pure}} = \sigma_{\tilde{X}}^{-1} \tag{4.6.10}$$

Substituting (4.6.10) into $\mathbf{K}_{\text{pure}}$ and comparing with (4.4.12) at the ground state gives

$$\mathbf{K}_{X*} = \mathbf{K}_{\text{pure}} \tag{4.6.11a}$$

$$= \mathbf{M}_{\tilde{X}} \sigma_{\tilde{X}}^{-1} \mathbf{M}_{\tilde{X}}^{\dagger} \tag{4.6.11b}$$

Although now mathematically proven, it is still not apparent as to how (4.6.11a) works from a physical perspective. One possible explanation is that $\mathbf{K}_{\tilde{X}}$ goes against the Pauli exclusion principle due to the overlapping (nonorthogonal) molecular orbitals. This suggests that the occupation numbers would not be in the range $[0, 1]$. By purifying the density kernel, the occupation numbers would be driven to either 0 or 1 and could correspond to the removal of the overlaps.

Chapter 5

Orthogonalization of Orbitals

Two methods of orthogonalization are discussed: symmetric orthogonalization (SO, also known as Löwdin orthogonalization) and weighted orthogonalization (WO). The iterated classical Gram-Schmidt (ICGS) process is an essential method for the WO used in this work but is however not discussed due to its role as an already extensively studied method of orthogonalization and QR decomposition [59]. This work implements the efficient and numerically stable ICGS as proposed by Björck [59] without modification and is utilized as the preliminary orthogonalization method for WO.

5.1 Symmetric Orthogonalization (SO)

Symmetric orthogonalization is commonly used in orthogonalizing molecular orbitals. Let $\mathbf{V}_{\mathcal{L}}$ be a ket matrix that is the symmetric orthogonalization of a ket row matrix $\mathbf{V}$ such that

$$\mathbf{V}_{\mathcal{L}}^{\dagger}\mathbf{V}_{\mathcal{L}} = \mathbf{I} \tag{5.1.1}$$

Suppose that $\mathbf{V}_{\mathcal{L}}$ can be expanded as

$$\mathbf{V}_{\mathcal{L}} = \mathbf{V}\mathbf{A} \tag{5.1.2}$$

for some coefficient matrix $\mathbf{A}$. (5.1.1) is rewritten as

$$\mathbf{A}^\dagger \mathbf{V}^\dagger \mathbf{V} \mathbf{A} = \mathbf{I} \tag{5.1.3}$$

which is satisfied if

$$\mathbf{A} = \left(\mathbf{V}^\dagger \mathbf{V}\right)^{-\frac{1}{2}} \mathbf{B} \tag{5.1.4}$$

where $\mathbf{B}$ is an arbitrary unitary matrix. Letting $\mathbf{B} = \mathbf{I}$ gives the method of symmetric orthogonalization of $\mathbf{V}$:

$$\mathbf{V}_{\mathcal{L}} = \mathbf{V} \left(\mathbf{V}^\dagger \mathbf{V}\right)^{-\frac{1}{2}} \tag{5.1.5}$$

The above derivation is similar to Szczepanik and Mrozek [71] and does not suggest that the original nonorthogonal kets correspond to the symmetrically orthogonalized ones in the same order in any way. However, Carlson and Keller [72] proved that symmetric orthogonalization satisfies the least-squares problem of

$$\arg\min_{\mathbf{V}'} \sum_i \left| V_i' - V_i \right|^2 \tag{5.1.6}$$

where $V_i \in \mathbf{V}$ such that $\mathbf{V}' = \mathbf{V}_{\mathcal{L}}$ satisfies the least squares. This suggests that symmetric orthogonalization can be regarded as a method that maintains the correspondence between the nonorthogonalized molecular orbitals and the orthogonalized ones.

5.2 Weighted Orthogonalization (WO)

Treating all molecular orbitals equally during orthogonalization would be inconsistent with their relative importance when the associated occupation numbers vary. As a result, some of the orthogonalized molecular orbitals should take higher priority in minimizing their displacements from their nonorthogonalized counterparts in a least-squares fashion. Such orthogonalization can be done using the weighted orthogonalization (WO) developed by West [73]. In general, the priority of a molecular orbital in relation to others depends on the context and the application. For this work, molecular

orbitals are orthogonalized using occupation numbers as weights. Using occupancies for weights lends consistency to how molecular orbitals are orthogonalized in the construction of the projection operators for SCF MI (§6) under EDFT (§8).

5.2.1 Formulation

WO is an orthogonalization process that depends on a preliminary orthogonalization process. Preliminary orthogonalization does not involve weights in any way (otherwise a circular dependency would occur), and it can be one of the following [73]:

- Gram-Schmidt (GS) process
- symmetric orthogonalization (SO)
- canonical orthogonalization

The iterated classical GS (ICGS) process of Björck [59] is chosen for this work due to its practicality, numerical stability, and performance. Implementing a numerically stable GS process also has an important benefit of immediately providing a method of QR decomposition. Canonical orthogonalization is not considered, since it requires diagonalization (which is cubic-scaling) and has narrower applicability compared to ICGS. SO is rendered unnecessary by WO, since it can be obtained when all weights for WO are equal [73]. Furthermore, SO has the undesirable process of determining the inverse square root of an overlap matrix.

Starting with $\mathbf{P} = \begin{pmatrix} |p_1\rangle & |p_2\rangle & \cdots \end{pmatrix}$ as a nonorthogonal and normalized ket matrix of orbitals, it is preliminarily orthogonalized using ICGS (along with Cholesky decomposition if the basis set is nonorthogonal as discussed in §3.1) to yield its QR decomposition as

$$\mathbf{P} = \mathbf{Q}'\mathbf{R} \tag{5.2.1}$$

where $\mathbf{Q}' = \begin{pmatrix} |q'_1\rangle & |q'_2\rangle & \cdots \end{pmatrix}$ is an intermediate ket matrix that is orthogonal. The coefficient matrix, $\mathbf{R}$, is not used. The goal of WO is to transform $\mathbf{Q}'$ to $\mathbf{Q}$ by rotations such

that the weighted overlap sum, OVLPS, is maximized:

$$\text{OVLPS} = \text{tr}\left(\mathbf{w}\mathbf{P}^{\dagger}\mathbf{Q}\right) = \sum_k w_k \langle p_k | q_k \rangle \tag{5.2.2}$$

where $\mathbf{w}$ is a diagonal matrix of orthogonalization weights, and w_k is the weight associated with $|p_k\rangle$. Orthogonalization weights are predefined and must be provided to WO. Maximizing the OVLPS is achieved by performing sweeps of 2-by-2 Givens rotations on all pairs of orbitals until convergence is attained. (5.2.2) is essentially a reformulation of the least-squares problem for orbitals with weights.

$\mathbf{Q}$ is the unknown and can be expressed in terms of the known intermediate ket matrix, $\mathbf{Q}'$. For a pair of orbitals, the Givens rotation angle, θ_{ij}, is evaluated from

$$\begin{pmatrix} |q_i\rangle & |q_j\rangle \end{pmatrix} = \begin{pmatrix} |q_i'\rangle & \left|q_j'\right\rangle \end{pmatrix} \begin{pmatrix} \cos\theta_{ij} & -\sin\theta_{ij} \\ \sin\theta_{ij} & \cos\theta_{ij} \end{pmatrix}^{\mathrm{T}} \tag{5.2.3a}$$

$$|q_i\rangle = |q_i'\rangle \cos\theta_{ij} - \left|q_j'\right\rangle \sin\theta_{ij} \tag{5.2.3b}$$

$$|q_j\rangle = |q_i'\rangle \sin\theta_{ij} + \left|q_j'\right\rangle \cos\theta_{ij} \tag{5.2.3c}$$

which can be multiplied by the nonorthogonal counterparts with weights to obtain the weighted overlap sum for the pair, OVLPS_{ij}:

$$\begin{aligned} \text{OVLPS}_{ij} = {} & w_i \langle p_i | q_i' \rangle \cos\theta_{ij} - w_i \left\langle p_i \middle| q_j' \right\rangle \sin\theta_{ij} \\ & + w_j \langle p_j | q_i' \rangle \sin\theta_{ij} + w_j \left\langle p_j \middle| q_j' \right\rangle \cos\theta_{ij} \end{aligned} \tag{5.2.4}$$

Factoring by the trigonometric functions gives

$$\text{OVLPS}_{ij} = B_{ij}\cos\theta_{ij} + C_{ij}\sin\theta_{ij} \tag{5.2.5}$$

where

$$B_{ij} = w_i \langle p_i | q_i' \rangle + w_j \left\langle p_j \middle| q_j' \right\rangle \tag{5.2.6a}$$

$$C_{ij} = w_j \langle p_j | q_i' \rangle - w_i \left\langle p_i \middle| q_j' \right\rangle \tag{5.2.6b}$$

By using the trigonometric identity

$$\cos\left(\theta_{ij} - \gamma_{ij}\right) = \cos\theta_{ij}\cos\gamma_{ij} + \sin\theta_{ij}\sin\gamma_{ij} \tag{5.2.7}$$

the two terms in (5.2.5) can be combined into one by multiplying (5.2.7) with A_{ij} and comparing it:

$$\text{OVLPS}_{ij} = A_{ij}\cos\left(\theta_{ij} - \gamma_{ij}\right) \tag{5.2.8}$$

where

$$\cos\gamma_{ij} = \frac{B_{ij}}{A_{ij}} \tag{5.2.9a}$$

$$\sin\gamma_{ij} = \frac{C_{ij}}{A_{ij}} \tag{5.2.9b}$$

$$A_{ij} = \sqrt{B_{ij}^2 + C_{ij}^2} \tag{5.2.9c}$$

OVLPS_{ij} is maximized when $\theta_{ij} = \gamma_{ij}$ in (5.2.8). $\cos\gamma_{ij}$ and $\sin\gamma_{ij}$ are used to construct the rotation matrix in (5.2.3a) to determine $|q_i\rangle$ and $|q_j\rangle$. Givens rotations occur in sweeps, where each sweep is a sequence of (5.2.3a) for all pairs of i and j, and the process repeats until convergence is attained. Figure 5.1 illustrates WO of three vectors for one sweep.

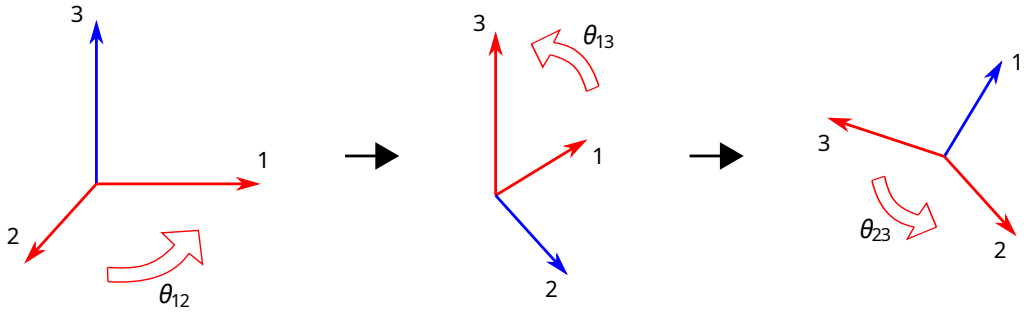

FIGURE 5.1: Weighted orthogonalization of three preliminarily orthonormalized vectors (which are from having performed ICGS) in 3D space for one sweep. Red vectors indicate the pair being rotated, using the blue vector as the rotation axis. Red unfilled arrow indicates the amount of rotation being performed for the pair of red vectors. Throughout the sweep, the orthonormality of the vectors is always preserved after any rotation. The amount of a rotation is determined by Equation (5.2.8).

Orthonormality is preserved throughout the process of WO, regardless of the weights.

This important property is a corollary of (5.2.3a) when multiplied by $\langle q'_k|$ from the left where $\forall k \notin \{i, j\}$:

$$\begin{pmatrix} \langle q'_k|q_i\rangle & \langle q'_k|q_j\rangle \end{pmatrix} = \begin{pmatrix} \langle q'_k|q'_i\rangle & \left\langle q'_k\middle|q'_j\right\rangle \end{pmatrix} \begin{pmatrix} \cos\theta_{ij} & -\sin\theta_{ij} \\ \sin\theta_{ij} & \cos\theta_{ij} \end{pmatrix}^{\mathrm{T}} \tag{5.2.10a}$$

$$= \begin{pmatrix} 0 & 0 \end{pmatrix} \begin{pmatrix} \cos\theta_{ij} & -\sin\theta_{ij} \\ \sin\theta_{ij} & \cos\theta_{ij} \end{pmatrix}^{\mathrm{T}} \tag{5.2.10b}$$

$$= \begin{pmatrix} 0 & 0 \end{pmatrix} \tag{5.2.10c}$$

which states that the result of rotating a pair of kets maintains orthogonality with other kets not participating in the rotation. The two kets undergoing rotation remain orthonormal to each other:

$$\begin{pmatrix} \langle q_i| \\ \langle q_j| \end{pmatrix} \begin{pmatrix} |q_i\rangle & |q_j\end{pmatrix} = \begin{pmatrix} 1 & 0 \\ 0 & 1 \end{pmatrix} \tag{5.2.11}$$

Since the transformation from $\mathbf{Q}'$ to $\mathbf{Q}$ involves such pairwise rotations, (5.2.10c) and (5.2.11) always hold, leading to $\mathbf{Q}$ being orthogonal.

An essential property for deriving and interpreting mathematical terms wherever orbital orthogonalization occurs is called the overlap-equivalence property in this work. To derive this property, the process of WO is first mathematically (but not computationally) abstracted as two transformations [73]:

$$\mathbf{Q}' = \mathbf{P}\mathbf{T}_0 \tag{5.2.12a}$$

$$\mathbf{Q} = \mathbf{Q}'\mathbf{T}_{\mathrm{G}} = \mathbf{P}\mathbf{T}_{\mathrm{W}} \tag{5.2.12b}$$

where $\mathbf{T}_0$ is the transformation matrix for preliminary orthogonalization, $\mathbf{T}_{\mathrm{G}}$ is the transformation matrix for a sequence of Givens rotations, and $\mathbf{T}_{\mathrm{W}}$ is defined as

$$\mathbf{T}_{\mathrm{W}} \equiv \mathbf{T}_0\mathbf{T}_{\mathrm{G}} \tag{5.2.13}$$

Since a GS process is a method of QR decomposition, $\mathbf{T}_0$ is the inverse of the coefficient matrix from (5.2.1):

$$\mathbf{Q}'\mathbf{R} = \mathbf{P} \implies \mathbf{Q}' = \mathbf{P}\mathbf{R}^{-1} = \mathbf{P}\mathbf{T}_0 \tag{5.2.14}$$

which is for mathematical context only. Computationally, neither $\mathbf{R}$ nor its inverse is needed for WO. For comparison, SO has the usual $\mathbf{T}_0 = \left(\mathbf{P}^\dagger\mathbf{P}\right)^{-\frac{1}{2}}$ as its orthogonalizing matrix, which is never used in this work. $\mathbf{T}_\mathrm{G}$ is an orthogonal matrix and represents a sequence of Givens rotations denoted by

$$\mathbf{T}_\mathrm{G} = \prod_k^\infty \mathbf{G}_k^\mathrm{T} \tag{5.2.15}$$

where each $\mathbf{G}_k^\mathrm{T}$ corresponds to the rotation matrix in (5.2.3a) but appropriately extended with ones along the diagonal, and is for mathematical context only. Computationally, $\mathbf{T}_\mathrm{G}$ is never constructed due to the computational cost of repeated multiplications of individual Givens rotations. Instead, (5.2.3a) is used, and the sweeps of 2-by-2 Givens rotations terminate upon convergence.

The overlap of $\mathbf{Q}$ must be an identity and forms the basis for the overlap-equivalence property:

$$\mathbf{Q}^\dagger\mathbf{Q} = \mathbf{I} \tag{5.2.16a}$$

$$\mathbf{T}_\mathrm{W}^\dagger\mathbf{P}^\dagger\mathbf{P}\mathbf{T}_\mathrm{W} = \mathbf{I} \tag{5.2.16b}$$

$$\mathbf{P}^\dagger\mathbf{P} = \left(\mathbf{T}_\mathrm{W}^{-1}\right)^\dagger \mathbf{T}_\mathrm{W}^{-1} \tag{5.2.16c}$$

$$\left(\mathbf{P}^\dagger\mathbf{P}\right)^{-1} = \mathbf{T}_\mathrm{W}\mathbf{T}_\mathrm{W}^\dagger \tag{5.2.16d}$$

where $\mathbf{T}_\mathrm{W}$ is invertible if $\mathbf{T}_0$ is invertible, which is normally the case. It is mathematically valid to simplify $\mathbf{T}_\mathrm{W}\mathbf{T}_\mathrm{W}^\dagger$ as $\mathbf{T}_0\mathbf{T}_0^\dagger$ by taking advantage that $\mathbf{T}_\mathrm{G}$ is an orthogonal matrix. However, such simplification is intentionally avoided, because doing so may inadvertently mislead the interpretation of $\mathbf{Q}$ as if only preliminary orthogonalization has occurred. Practically, such simplification is not useful in most cases, and formulations generally benefit more from the mathematical abstraction of WO transformation

as $\mathbf{T}_\mathrm{W}$. The significance of the overlap-equivalence property arises from the ability to substitute $\mathbf{P}^\dagger\mathbf{P}$ and its inverse with the transformation matrices of WO in a mathematical formulation that originally assumes SO for orbital orthogonalization. Reasons for assuming SO in a formulation could be historical, conventional, or intentional for mathematical amenability.

5.2.2 Performance

5.2.2.1 Theory

It is possible to expand the orbitals in $\mathbf{P}$, $\mathbf{Q}'$, and $\mathbf{Q}$ in terms of a basis set, but it is both mathematically unnecessary and computationally detrimental. Mathematically, expanding the orbitals in a basis set results in cluttered expressions, when instead Cholesky decomposition can be used for directly working with the orbitals themselves without expansion (cf. §3.1). Computationally, performance suffers drastically to the point of WO being unusable very quickly as the number of basis functions increases only moderately. This is due to the fact that if the basis set is nonorthogonal (which is usually the case), evaluating the scalar product of two kets, $\langle a|b\rangle$, requires multiplying the basis overlap, $\mathbf{S} = \mathbf{\Phi}^\dagger\mathbf{\Phi}$, in the middle:

$$\langle a|b\rangle = \begin{pmatrix} a_1'^* & a_2'^* & \cdots \end{pmatrix} \mathbf{S} \begin{pmatrix} b_1' \\ b_2' \\ \vdots \end{pmatrix} \tag{5.2.17}$$

where a_k' and b_k' are expansion coefficients in the basis set.

Implementation, instead, employs Cholesky decomposition to obviate the multiplying of the basis overlap. In this approach, Cholesky decomposition is used to obtain the basis functions, $\mathbf{\Phi}$, as a ket matrix in (3.1.4). With $\mathbf{\Phi}$, the basis functions are effectively

merged into the columns representing the kets:

$$|a\rangle = \mathbf{\Phi} \begin{pmatrix} a'_1 \\ a'_2 \\ \vdots \end{pmatrix} = \begin{pmatrix} a_1 \\ a_2 \\ \vdots \end{pmatrix} \tag{5.2.18a}$$

$$|b\rangle = \mathbf{\Phi} \begin{pmatrix} b'_1 \\ b'_2 \\ \vdots \end{pmatrix} = \begin{pmatrix} b_1 \\ b_2 \\ \vdots \end{pmatrix} \tag{5.2.18b}$$

where a_k and b_k are elements of the corresponding ket matrices representing $|a\rangle$ and $|b\rangle$, and are therefore no longer considered to be expansion coefficients. Multiplying the basis overlap in the middle becomes inherently performed for each evaluation of the scalar product, and the equivalent scalar product, then, is implemented as

$$\langle a|b\rangle = \begin{pmatrix} a_1^* & a_2^* & \dots \end{pmatrix} \begin{pmatrix} b_1 \\ b_2 \\ \vdots \end{pmatrix} \tag{5.2.19}$$

5.2.2.2 Benchmarks

To quantify the improvement in performance that bra-ket matrix and Cholesky decomposition make, random square matrices of sizes from 500×500 to 5000×5000 in increments of 500×500 were generated. To simulate the type of matrices that are involved in SCF MI (which are block-diagonal by nature of the SCF-MI process being fragment-based, cf. §6), each generated matrix is block-diagonal with exactly five random blocks along the diagonal regardless of the matrix size, and off-diagonal blocks are set to zero. For instance, a 1000×1000 matrix has five 200×200 random blocks along the diagonal.

Each block is then orthogonalized using ICGS without regard to other blocks. While each block in a matrix is orthogonal, the matrix itself is not. These matrices with individually orthogonalized blocks serve as the starting point for benchmarking under the two competing scenarios where a basis overlap is or is not multiplied in the middle (as in (5.2.17) and (5.2.19), respectively). The basis overlap used is simply the identity matrix, because it is the difference between having an overlap matrix in the middle and

not having one that matters in this benchmarking, not the performance of Cholesky decomposition itself. In other words, having an overlap matrix (even though it is an identity matrix) would mimic not using Cholesky decomposition and that the orbitals are expanded in a basis set with a coefficient matrix.

The benchmarking process is diagrammed in Figure 5.2 and was performed using 80 cores (at 2 hosts, 10 MPI processes per host, and 4 OpenMP threads per MPI process). Parallelization of ICGS is according to Björck [59], and parallelization of WO is the Givens Relaxation Scheme (GRS, discussed in §5.3).

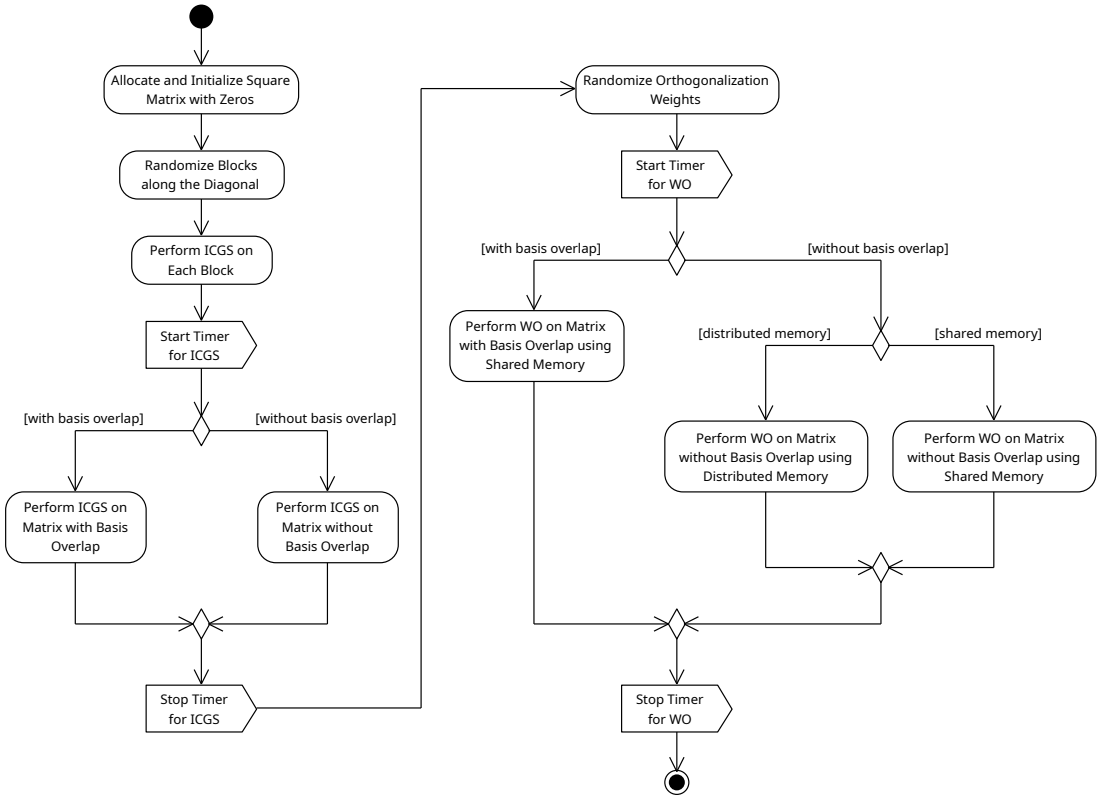

FIGURE 5.2: UML activity diagram of the benchmarking process for ICGS and WO in various implementation scenarios. Timers are used at the indicated points to measure the duration of each implementation. For all branch points, the right branch is the route with the faster implementation. There is no branch for benchmarking the use of distributed memory with a basis overlap, which would be the most conventional implementation, because such combination produces performance so poor that there is no point in measuring the time it takes. Distributed and shared memory models are discussed in §5.3.2.1.

The plot in Figure 5.3 illustrates the ICGS performance difference between implementations that use either (5.2.17) or (5.2.19). Despite employing the same parallelization strategy of Björck [59], having a basis overlap multiplied in the middle of the scalar

products causes a 14-fold slowdown in the ICGS of a 5000×5000 matrix. Even at a relatively large size of 10 000 rows/columns, not having a basis overlap is still 9 times faster than having a basis overlap. This demonstrates the obvious problem that mathematically equivalent formulations with seemingly harmless nuances can have completely different time complexities in implementations.

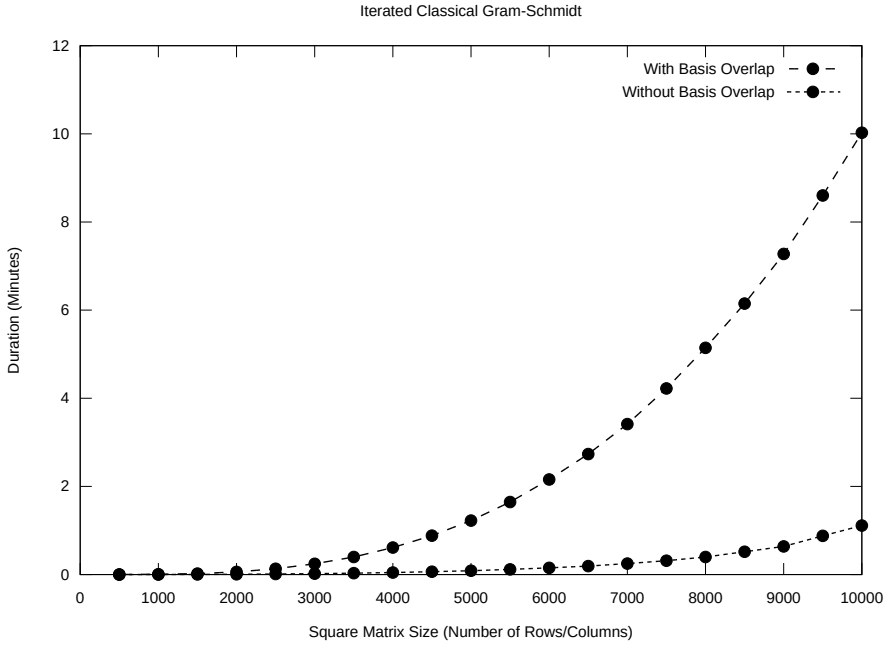

FIGURE 5.3: Performance of ICGS with and without a basis overlap. Parallelization is across 2 hosts, 10 MPI processes per host, and 4 OpenMP threads per MPI process. Numerical values are provided in Table B.1.

Figure 5.4 demonstrates the same problem of having a basis overlap but also with different memory models of GRS (cf. §5.3). While a shared memory model far outperforms a distributed memory model, the extremely poor performance of having a basis overlap still cannot be rescued by a shared memory model. In fact, matrix sizes greater than 5000×5000 are not benchmarked for the case where a basis overlap is used, simply because such benchmarks may never finish within a reasonable amount of time. This is the reason for not measuring the performance of the most conventional implementation where a basis overlap is used with a distributed memory model. Since the reliance on a basis overlap for scalar products and employing a particular memory model are separate bottlenecks of WO, there is no need to benchmark what would be the slowest possible pair.

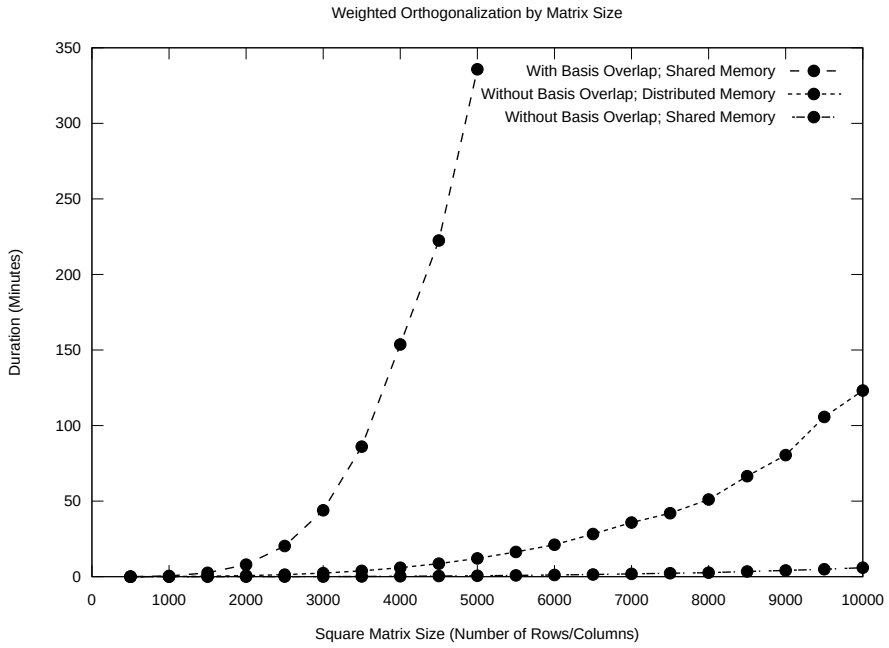

FIGURE 5.4: Performance of WO using GRS (discussed in §5.3) with different memory models. Parallelization is across 2 hosts, 10 MPI processes per host, and 4 OpenMP threads per MPI process. Matrix sizes beyond 5000 are not benchmarked for the implementation where a basis overlap is used due to extremely long durations. Numerical values are provided in Table B.2.

5.3 Givens Relaxation Scheme (GRS)

5.3.1 Introduction

Algorithms that perform mutually dependent operations involve operations whose results are affected by subsequent operations during an iterative process. Examples of such algorithms are weighted orthogonalization (WO, cf. §5.2) and singular value decomposition (SVD). While implementing a serial version is relatively straightforward, parallelizing the same algorithm is not and usually involves heuristic approaches that counteract or mitigate the effects of the mutually dependent operations.

One such parallelization strategy is the Jacobi Relaxation Scheme (JRS) developed by Rajasekaran and Song [74] for carrying out SVD using Jacobi rotations. The central idea of JRS is that each pair of columns or rows is rotated by a fraction of the full (unrelaxed) angle that would be done in a serial version. The fraction is defined by the relaxation parameter, λ, such that the relaxed angle, θ_{relax}, from the unrelaxed angle,

θ_{unrelax}, is

$$\theta_{\text{relax}} = (1 - \lambda)\,\theta_{\text{unrelax}} \tag{5.3.1}$$

with the constraint that $0 \leq \lambda < 1$. A relaxed rotation that stops short of the full angle minimizes the amount of change to a mutually dependent rotation that has been previously done. The relaxed rotations for all pairs of columns or rows can be concurrently calculated using the same untransformed matrix while ignoring the mutual affects, which are now reduced, of the rotations. The matrix is then transformed as a whole by applying the pre-calculated relaxed rotations to the columns or rows. The process repeats until no more pairs of columns or rows need to be rotated. Rajasekaran and Song [74] offers suggestions for the value of λ.

The Givens Relaxation Scheme (GRS) is the parallelization strategy implemented for WO in this work and is closely based on JRS. JRS was originally developed for the parallelization of Jacobi rotations in SVD [74]. GRS separates out the parallelization scheme from the original intent so that any numerical method that also involves mutually dependent rotations of pairs can be parallelized as well. Other than the generalization of the intent, the difference between JRS and GRS is whether the relaxation parameter changes. Relaxation parameter in JRS is fixed throughout the process, whereas it is dynamic in GRS. By making the relaxation parameter adjustable during the process, GRS facilitates the convergence of WO more so than JRS.

5.3.2 Algorithm

GRS is an algorithmic process as opposed to a mathematical one and is diagrammed in Figure 5.5. The description of the implementation will go into the details of the actions in the activity diagram, starting from the initial node to the activity final node with yellow notes anchored at points of interest. Furthermore, the problem of a distributed-memory model compared to a shared-memory model in the context of performance and how it plays a role in GRS is discussed in a dedicated subsection later (§5.3.2.1).

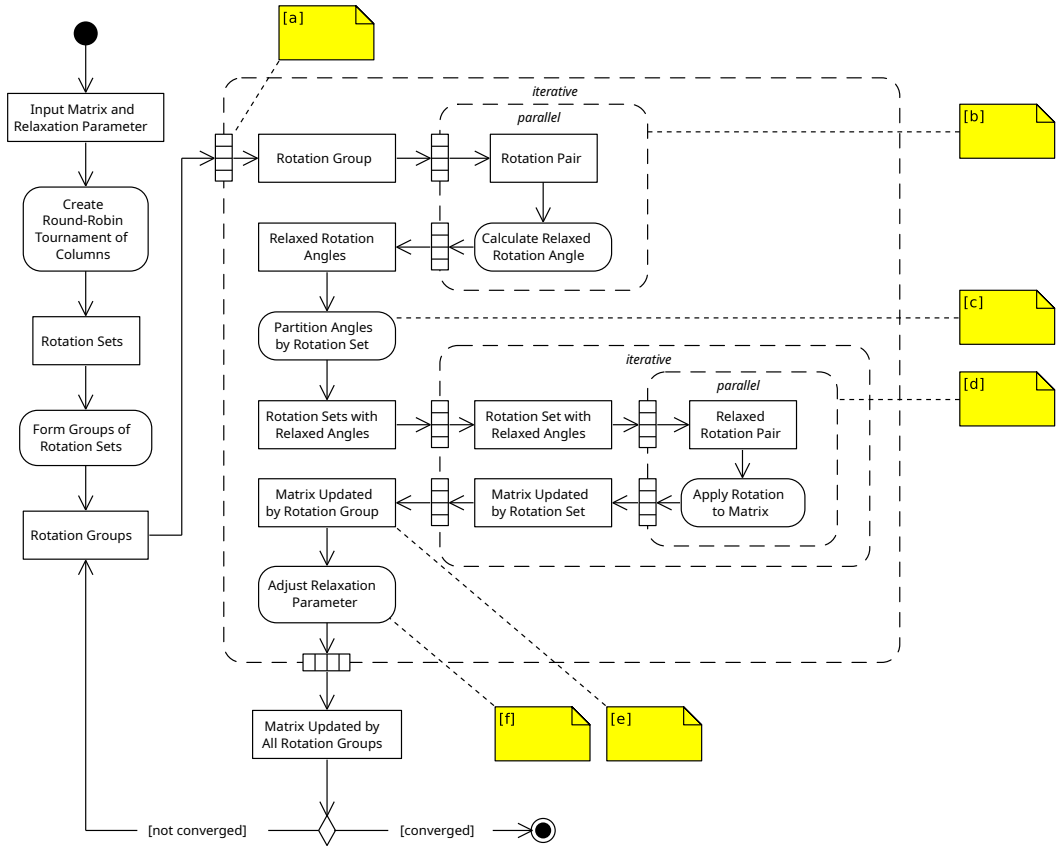

FIGURE 5.5: UML activity diagram of the Givens Relaxation Scheme (GRS) process. Box with round corners is an action. Box with square corners is an object node that indicates data. Dashed box is an expansion region (which can be thought of as a loop) that indicates the activity for each element in an iterative (sequential) or parallel manner with respect to other elements. Yellow notes are anchored to points of interest and are referred from the text.

Starting with an input matrix and an initial relaxation parameter, a round-robin tournament of the column indices is created using the circle method, where each round represents a set of non-conflicting rotations called a rotation set. The circle method is implemented using efficient move operations on contiguous chunks of memory so that the indices can quickly cycle through the slots. For example, Figure 5.6 depicts how the rotation sets for five columns are generated. Rotation sets are then arbitrarily grouped into rotation groups, where having more than one set in a group improves convergence [74]. In this work, the number of rotation groups is set to be the same as the number of MPI processes for convenience.

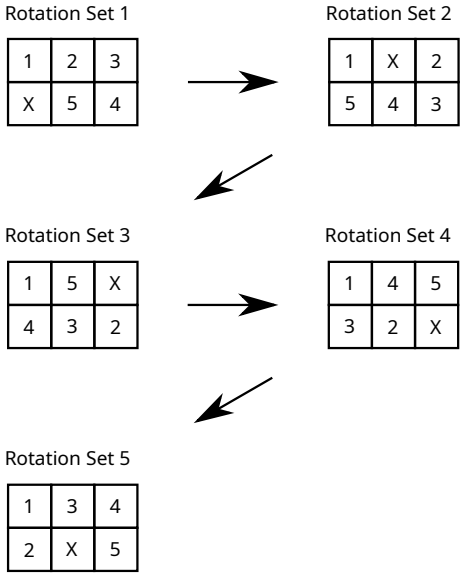

FIGURE 5.6: Rotation sets for five indices determined by round-robin tournament using the circle method. Each rotation set corresponds to a round in round-robin tournament. X denotes a dummy competitor, which is used since there is an odd number of indices. Index 1 is fixed in position, while the other indices (including the dummy competitor) cycle through the slots. A rotation set contains non-conflicting rotation pairs that can be concurrently applied to the matrix. The rotation sets in this example, respectively, are $\{(2,5),(3,4)\}$, $\{(1,5),(2,3)\}$, $\{(1,4),(5,3)\}$, $\{(1,3),(4,2)\}$, and $\{(1,2),(4,5)\}$.

Each rotation group is iteratively processed for the relaxed rotation angles (Figure 5.5, Note [a]). Rotation pairs in the rotation group are concurrently evaluated by a user-defined function for the relaxed rotation angles (5.3.1) without updating the matrix (Figure 5.5, Note [b]). It is the use of a user-defined function that broadens the applicability of GRS beyond the original intent of JRS, which was developed for SVD [74]. The downside to the wider applicability of GRS is that it requires explicit rotation angles, not the sines and cosines of the rotation angles. Concurrent evaluations of the rotation angles occur across all OpenMP threads of all MPI processes with the workload of it being equally distributed in an agnostic manner (i.e., MPI rank and OpenMP thread number are not significant). For this work, the rotation angles are that of WO (cf. §5.2) calculated from (5.2.9) in a user-defined function separate from GRS.

Once the relaxed rotation angles are determined, they are partitioned according to the rotation set that a rotation pair is in (Figure 5.5, Note [c]). The purpose of this partitioning is that the updating of the matrix is performed by rotation set, not by rotation group, since it is a rotation set that contains non-conflicting rotations and, hence, can be applied in a parallel manner. For each rotation set in the rotation group, rotation

pairs with relaxed angles are concurrently applied to the matrix, yielding an updated matrix (Figure 5.5, Note [d]). Applying the rotations from the rotation sets in the rotation group then updates the matrix for the rotation group (Figure 5.5, Note [e]). Even though the rotations in a rotation group conflict with each other and were determined using the non-updated matrix, the relaxation of the rotation angles reduces the affect the rotations have on each other [74].

After updating the matrix for the rotation group, the relaxation parameter is adjusted (Figure 5.5, Note [f]) and is unique to GRS that is not in JRS (which has the relaxation parameter fixed throughout the process). The relaxation parameter is adjusted according to a specified user-defined function, but the adjustment usually decreases the relaxation parameter. Decreasing the relaxation parameter stems from the reasoning that fewer or smaller rotations are needed as the process progresses. As the rotations get fewer or smaller, the rotations can be applied with progressively lesser relaxations, since the matrix is approaching convergence and does not need updates that are as large as during the beginning of the GRS process. With a dynamically decreasing relaxation parameter, the matrix can eventually be updated more directly to the supposed converged matrix. In this work, the relaxation parameter is simply halved after each rotation group is applied.

After all rotation groups have been applied in updating the matrix, convergence is checked by a specified user-defined function to allow flexibility in the convergence criteria. If convergence is not attained, the rotation groups reenter the process of evaluating the relaxed rotation angles and applying the rotations. In this work, the convergence criterion is simply the Frobenius norm of the difference between the previous and current matrices is less than some threshold.

5.3.2.1 Memory Model

Updating the matrix from applying the rotations of a rotation set was unexpectedly the worst bottleneck in the GRS process (Figure 5.5, Note [d]). In a previous implementation of GRS, it was discovered that the poor performance of updating the matrix was caused by the overhead from making many MPI calls in synchronizing the rotated

columns for WO, since each MPI process was updating only a portion of the matrix and many rounds of message passing were being performed just to synchronize the update.

If there is an even number of columns, n, to rotate in pairs, then there are $n-1$ rotation sets. If there is an even number of MPI processes, k, to perform the rotations for one sweep, then the number of rounds (in the style of a round-robin tournament) of data exchanges among the MPI processes for all rotation sets would be $(n-1)(k-1)$. Further worsening the bottleneck is the number of sweeps needed to attain convergence. For transforming a matrix with 5000 columns across 50 MPI processes, the total number of rounds of data exchanges to synchronize the updating of the matrix for only one sweep is approximately 250 000. Since the number of MPI processes normally increases as the size of the matrix increases, this back-of-the-envelope calculation suggests that the amount of message passing might counteract the parallelization of updating the matrix, which was observed to be indeed the case and is demonstrated with benchmarks in §5.3.3.

Since the cause of the bottleneck was from the amount of MPI calls in the updating of the matrix, several approaches were explored to reduce, mitigate, or even obviate the MPI calls. Such approaches included column concatenation (for reducing the number of MPI calls), binary serialization (for increasing read and write speeds), data compression (for reducing the size of data transfer), and distributed caching system like memcached (for storing data to be accessible from any host in the cluster). However, these workarounds either provided little to no improvement in performance or degraded it further. The failed attempts with distributed caching eventually spawned another approach that proved to be a workable solution to the bottleneck, which is the allocation and use of memory that is shared across MPI processes at a host.

Shared memory is allocated at each host in a cluster. To achieve this, each process in an MPI communicator first needs to query for the hostname where the process is located. The original MPI communicator is then split according to host so that the processes in each newly created communicator are at the same host. One process in each communicator would allocate shared memory for the processes at that host. Memory cannot be shared across hosts. Allocated shared memories would serve as the backing storages for particular matrices in GRS.

By using the MPI communicator associated to a specific host, the matrix to be updated can be subdivided among the MPI processes at that host, and the rotations in a rotation set can therefore be applied concurrently without having to send and receive the rotated columns via numerous MPI calls. Modifications to a matrix that uses shared memory are visible to the processes at the host. Because of the sharing of memory, the processes must coordinate their reads from and writes to the matrix, which in GRS is done by subdividing the matrix according to columns and assigning the subdivisions among the MPI processes at each host. Since the rotations in a rotation set are non-conflicting, the subdivisions are non-overlapping by nature. This allows the MPI processes at each host to concurrently apply the rotations in a rotation set without race conditions and obviates mechanisms like mutexes and barriers.

Because memory cannot be shared across hosts, MPI processes at each host must apply all rotations in a rotation set when using shared memory. This has the consequence of scaling well vertically when more cores are utilized at each host to update the matrix, but horizontal scaling from more hosts would apparently be less effective. Nevertheless, the use of distributed memory where rotated columns are exchanged through MPI sends and receives results in very poor performance, whereas the performance boost from using shared memory far outweighs its disadvantage of being less effective in horizontal scaling. Performance differences between using a distributed memory model and a shared memory model were benchmarked in §5.2.2.2.

5.3.3 Performance Benchmarks

Performance of GRS executing weighted orthogonalization (WO, cf. §5.2) with respect to vertical and horizontal scaling is benchmarked using three different matrix sizes: 5000×5000, 7500×7500, and $10\,000 \times 10\,000$. Same as for benchmarking WO in §5.2.2.2, matrices are square matrices with five random blocks along the diagonal. For vertical scaling, exactly one host with the number of MPI processes ranging from 1 to 10 (Figure 5.7). For horizontal scaling, 10 MPI processes are launched for each host with the number of hosts ranging from 1 to 8 (Figure 5.8). In both cases of scaling, each MPI process has 4 OpenMP threads spawned. Unlike the WO performance benchmarks in §5.2.2.2, benchmarking GRS focuses on scalability as opposed to the implementation

variants depicted in Figure 5.2, and the fastest variant (i.e., shared memory and not having a basis overlap) is always used.

As discussed in §5.3.2.1, vertical scaling is expected to have greater improvement in performance compared to horizontal scaling. Figure 5.7 demonstrates a rapid decrease in duration at the beginning when the number of MPI processes at one host is increased, eventually starting to saturate toward 10 MPI processes. The decrease in duration is more dramatic as the size of the matrix increases. Another factor contributing to the speedup is the increase in the number of rotation groups when the number of MPI processes increases. However, the number of rotation groups is arbitrarily defined to be the number of MPI processes (cf. §5.3.2), and therefore, the speedup from the greater number of rotation groups cannot be rigorously determined from these benchmarks alone. Nevertheless, the speedup from grouping rotation sets was demonstrated by Rajasekaran and Song [74] and is not an artifact.

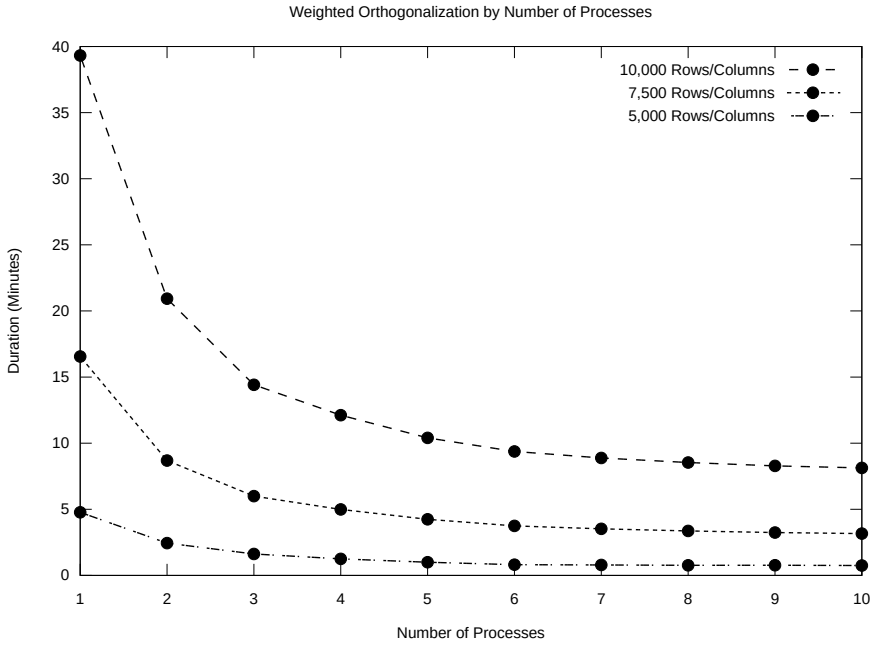

FIGURE 5.7: Performance of GRS executing WO through vertical scaling by increasing number of MPI processes at one host. Each MPI process has 4 OpenMP threads spawned. Numerical values are provided in Table B.3.

Unlike vertical scaling, horizontal scaling of GRS reaches saturation more quickly

when the number of hosts is increased (Figure 5.8). Performance hardly improves beyond using 2 or 3 hosts. However, significant speedup is still observed for larger matrices such as 7500×7500 and $10\,000 \times 10\,000$, whereas the matrix size of 5000×5000 experiences only a miniscule speedup. There are two possible reasons to the initial speedup for larger matrices. The first reason is that increasing the number of rotation groups up to a certain point improves performance. The second reason is that increasing the total number of cores across all hosts for calculating the relaxed rotations (Figure 5.5, Note [b]) improves performance. Calculating the relaxed rotations is independent of the memory model and is done by all OpenMP threads across all hosts.

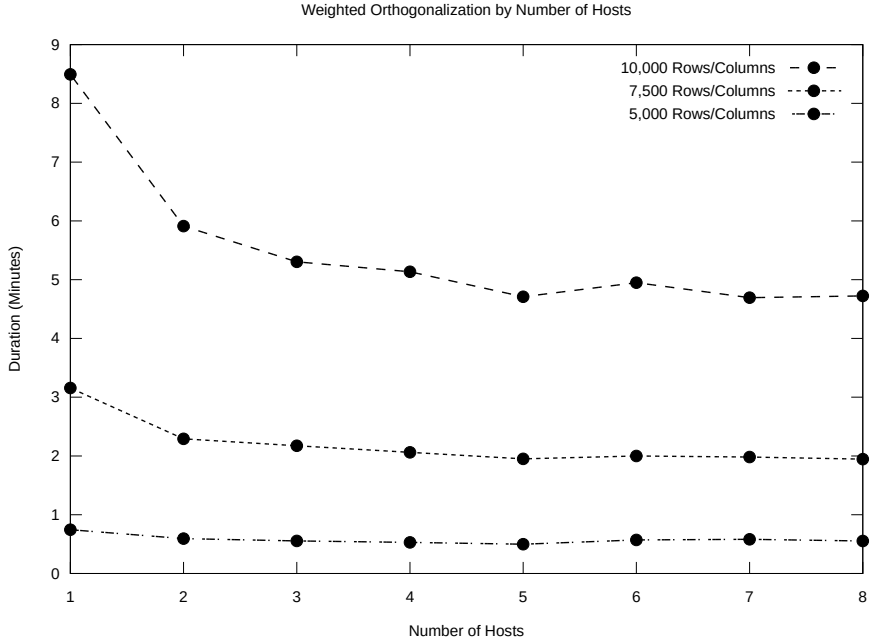

FIGURE 5.8: Performance of GRS executing WO through horizontal scaling by increasing number of hosts. Each host has 10 MPI processes launched. Each MPI process has 4 OpenMP threads spawned. Numerical values are provided in Table B.4.

These benchmark results suggest that horizontal scaling is still beneficial in addition to vertical scaling. When studying systems with large number of molecular orbitals, the number of hosts being used would naturally increase. As Figure 5.8 indicates, the number of hosts at the point of saturation is slightly increased with larger matrix size. But prior to saturation, the speedup remains significant for horizontal scaling.

Chapter 6

Self-Consistent Field for Molecular Interaction (SCF MI)

Basis set superposition error (BSSE) is a problem that has been widely studied with many methods and variations thereof being proposed for eliminating it [75, 76]. Used by some EDA schemes, a family of methods for describing and dealing with this error is the self-consistent field for molecular interaction (SCF MI) [77, 78, 79, 80, 81, 82, 76]. SCF MI constructs molecular orbitals using basis functions from each corresponding fragment only, which reduces charge transfer among fragments [81]. LMO SCF MI is chosen as the SCF-MI method for HALMO EDA due to its mathematical amenability of incorporating fractional occupancies. For ONETEP, BSSE is not exhibited [20], since the NGWFs (cf. §2.2.5) that ONETEP uses for expanding the molecular orbitals are themselves expanded in terms of a plane-wave basis set defined as periodic sinc (psinc) functions [83]. The psinc functions homogeneously span the simulation cell and are not biased by the atomic positions. As such for ONETEP, SCF MI is used exclusively for the purpose of separating out the charge-transfer component [84, 19]. Two SCF-MI methods, locally projected (LP) SCF MI [81] and LMO SCF MI [79], are discussed as representative approaches.

LP SCF MI employs projection operators to constrain the molecular orbitals solved for each fragment [81]. LP SCF MI is not chosen for this work due to its effective Hamiltonian not being Hermitian and the less rigorous means of incorporating fractional occupancies than LMO SCF MI. Despite its shortcomings, LP SCF MI is still considered

as an informative approach and for it being mathematically simpler than LMO SCF MI.

LMO SCF MI minimizes the energy of a quantum state with localized molecular orbitals [79]. The method originally has no name, but it is called LMO SCF MI in this work because of the pervasive use of the term ”localized molecular orbitals” in Stoll et al. [79]. The energy minimum is derived from the differentiation of energy with respect to the fragment-localized molecular orbitals and then casting it into an eigenvalue equation. It has the property that the effective Hamiltonian for each fragment is Hermitian, and hence, the molecular orbitals in each fragment are orthogonal. Despite its coincidental naming, it is not related to LMO EDA (cf. §4.5.1) [14].

The current implementation of HALMO EDA has only LMO SCF MI, but LP SCF MI could also be implemented in future work. While LP SCF MI can accommodate fractional occupancies in theory, LMO SCF MI is continued to be used as the primary SCF-MI method for HALMO EDA due to its more rigorous amenability of incorporating fractional occupancies, which is required when performing EDA with ensemble DFT (EDFT, cf. §8).

6.1 Locally Projected (LP) SCF MI

LP SCF MI was developed by Nagata et al. [81] and uses projection operators to constrain the space that the molecular orbitals are solved in. As a preliminary setup to LP SCF MI itself, more basic equations are first developed in terms of projected molecular orbitals, which in turn can be expanded in a projected basis set. The construct of projected basis functions allows a relationship with the original, non-projected basis functions to be established. This relationship is left implicit in Nagata et al. [81] but provides the starting point for LP SCF MI.

6.1.1 Exclusion of Orbitals

In §4.3, the notation for orbitals of a specific fragment are introduced. Additionally, references to all basis functions or molecular orbitals except those localized to a particular fragment are made in LP SCF MI. To specify such exclusion of orbitals, the notation,

$\mathbf{\Psi}_{J'}$, is defined as all molecular orbitals except those localized to J:

$$\mathbf{\Psi}_{J'} \equiv \begin{pmatrix} \mathbf{\Psi}_A & \cdots & \mathbf{\Psi}_I & \mathbf{\Psi}_K & \cdots \end{pmatrix} \tag{6.1.1}$$

which can be expanded as

$$\mathbf{\Psi}_{J'} = \mathbf{\Phi}_{J'}\mathbf{M}_{J'} \tag{6.1.2}$$

where

$$\mathbf{\Phi}_{J'} = \begin{pmatrix} \mathbf{\Phi}_A & \cdots & \mathbf{\Phi}_I & \mathbf{\Phi}_K & \cdots \end{pmatrix} \tag{6.1.3}$$

and

$$\mathbf{M}_{J'} = \begin{pmatrix} \mathbf{M}_A & \mathbf{0} & \mathbf{0} & \mathbf{0} & \cdots \\ \mathbf{0} & \ddots & \mathbf{0} & \mathbf{0} & \cdots \\ \mathbf{0} & \mathbf{0} & \mathbf{M}_I & \mathbf{0} & \cdots \\ \mathbf{0} & \mathbf{0} & \mathbf{0} & \mathbf{M}_K & \cdots \\ \vdots & \vdots & \vdots & \vdots & \ddots \end{pmatrix} \tag{6.1.4}$$

The omission of $\mathbf{\Psi}_J$ is needed in the construction of projection operators (discussed next in §6.1.2) as $1 - \hat{P}_{J'}$ and must be distinguished from the nonequivalent projection operator, $\hat{P}_J$. The nonequivalence is demonstrated later in §6.1.3 using proof by contradiction.

6.1.2 Projection Operators and Projected Molecular Orbitals

For a Fragment J, the projection operator, $\hat{P}_J$, onto the molecular orbitals localized to Fragment J is defined as

$$\hat{P}_J \equiv \mathbf{\Psi}_J \mathbf{T}_{\mathrm{W},J} \mathbf{T}_{\mathrm{W},J}^{\dagger} \mathbf{\Psi}_J^{\dagger} \tag{6.1.5}$$

where $\mathbf{T}_{\mathrm{W},J}$ is the transformation matrix from weighted orthogonalization of the molecular orbitals in Fragment J using occupation numbers as weights (cf. §5.2). The projection operator, $\hat{P}_{J'}$, onto the molecular orbitals not localized to Fragment J is defined as

$$\hat{P}_{J'} \equiv \mathbf{\Psi}_{J'} \mathbf{T}_{\mathrm{W},J'} \mathbf{T}_{\mathrm{W},J'}^{\dagger} \mathbf{\Psi}_{J'}^{\dagger} \tag{6.1.6}$$

where $\mathbf{T}_{\mathrm{W},J'}$ is similar to $\mathbf{T}_{\mathrm{W},J}$ but for all molecular orbitals not localized to Fragment J.

Unlike using the conventional description with summations, the projection operators in bra-ket matrices (cf. §3) allow multi-component systems to be considered directly without having to develop the method for a binary system first as a preliminary step and then generalizing it as was done in Nagata et al. [81]. Projection operators can be defined differently [85], but the projection operators defined in this work follow that of Nagata et al. [81] as well as in other works [82].

Molecular orbitals of Fragment J projected outside the space spanned by the molecular orbitals of all other fragments not J is denoted as

$$\widehat{\mathbf{\Psi}}_J = \left(1 - \hat{P}_{J'}\right) \mathbf{\Psi}_J \tag{6.1.7}$$

which can be expanded in terms of the projected basis functions as

$$\widehat{\mathbf{\Psi}}_J = \left(1 - \hat{P}_{J'}\right) \mathbf{\Phi}_J \mathbf{M}_J \tag{6.1.8a}$$

$$= \widehat{\mathbf{\Phi}}_J \, \mathbf{M}_J \tag{6.1.8b}$$

where

$$\widehat{\mathbf{\Phi}}_J = \left(1 - \hat{P}_{J'}\right) \mathbf{\Phi}_J \tag{6.1.9}$$

is the projected basis functions for the molecular orbitals localized to Fragment J, and $\mathbf{M}_J$ is the corresponding expansion coefficients. (6.1.7) and (6.1.8b) provide different representations of the same thing.

6.1.3 Eigenvalue Equation

Molecular orbitals and their associated orbital energies for each fragment can be established as an eigenvalue equation. For a Fragment J, the eigenvalue equation has projected molecular orbitals, $\widehat{\mathbf{\Psi}}_J$, as the eigenfunctions and orbital energies, $\boldsymbol{\varepsilon}_J$, as the associated eigenvalues.

$$\hat{H}\,\widehat{\mathbf{\Psi}}_J = \widehat{\mathbf{\Psi}}_J\,\boldsymbol{\varepsilon}_J \tag{6.1.10}$$

Using (6.1.8b), (6.1.10) can be expressed in terms of the projected basis functions:

$$\hat{H}\,\widehat{\mathbf{\Phi}}_J\,\mathbf{M}_J = \widehat{\mathbf{\Phi}}_J\,\mathbf{M}_J\boldsymbol{\varepsilon}_J \tag{6.1.11}$$

Multiplying by $\widehat{\mathbf{\Phi}}_J^{\dagger}$ from the left, the eigenvalue equation for Fragment J is

$$\widehat{\mathbf{\Phi}}_J^{\dagger}\,\hat{H}\,\widehat{\mathbf{\Phi}}_J\,\mathbf{M}_J = \widehat{\mathbf{\Phi}}_J^{\dagger}\widehat{\mathbf{\Phi}}_J\,\mathbf{M}_J\boldsymbol{\varepsilon}_J \tag{6.1.12}$$

which is re-expressed in the non-projected basis functions using (6.1.9) as

$$\mathbf{\Phi}_J^{\dagger}\left(1-\hat{P}_{J'}\right)\hat{H}\left(1-\hat{P}_{J'}\right)\mathbf{\Phi}_J\mathbf{M}_J = \mathbf{\Phi}_J^{\dagger}\left(1-\hat{P}_{J'}\right)\mathbf{\Phi}_J\mathbf{M}_J\boldsymbol{\varepsilon}_J \tag{6.1.13}$$

(6.1.13) is the working equation of LP SCF MI. If an implementation employs bra-ket matrices (cf. §3), (6.1.13) can be directly solved without the need for further manipulation of the eigenvalue equation (discussed further in §6.2). Because of $\mathbf{\Phi}_J^{\dagger}\left(1-\hat{P}_{J'}\right)\mathbf{\Phi}_J$ on the right-hand side, the resulting molecular orbitals are nonorthogonal in each fragment.

However, if an implementation is a conventional one that does not use bra-ket matrices, then (6.1.13) cannot be solved as is, and further manipulation into an expression with only ordinary matrices is necessary. To obtain the same eigenvalue equation without bra-ket matrices, the operators are first distributed to give a generalized eigenvalue

problem in terms of the operators:

$$\left(\mathbf{\Phi}_J^\dagger \hat{H} \mathbf{\Phi}_J - \mathbf{\Phi}_J^\dagger \hat{P}_{J'} \hat{H} \mathbf{\Phi}_J - \mathbf{\Phi}_J^\dagger \hat{H} \hat{P}_{J'} \mathbf{\Phi}_J + \mathbf{\Phi}_J^\dagger \hat{P}_{J'} \hat{H} \hat{P}_{J'} \mathbf{\Phi}_J\right) \mathbf{M}_J = \left(\mathbf{S}_J - \mathbf{\Phi}_J^\dagger \hat{P}_{J'} \mathbf{\Phi}_J\right) \mathbf{M}_J \boldsymbol{\varepsilon}_J \tag{6.1.14}$$

Substituting the projection operators with their bra-ket matrices and letting $\mathbf{H}_{JK} = \mathbf{\Phi}_J^\dagger \hat{H} \mathbf{\Phi}_K$ give

$$\left(\mathbf{H}_J - \mathbf{S}_{JJ'} \mathbf{D}_{J'} \mathbf{H}_{J'J} - \mathbf{H}_{JJ'} \mathbf{D}_{J'} \mathbf{S}_{J'J} + \mathbf{S}_{JJ'} \mathbf{D}_{J'} \mathbf{H}_{J'} \mathbf{D}_{J'} \mathbf{S}_{J'J}\right) \mathbf{M}_J = \left(\mathbf{S}_J - \mathbf{S}_{JJ'} \mathbf{D}_{J'} \mathbf{S}_{J'J}\right) \mathbf{M}_J \boldsymbol{\varepsilon}_J \tag{6.1.15}$$

where $\mathbf{S}_{JK} = \mathbf{\Phi}_J^\dagger \mathbf{\Phi}_K$, and $\mathbf{D}_{J'} \equiv \mathbf{M}_{J'} \mathbf{T}_{\mathrm{W},J'} \mathbf{T}_{\mathrm{W},J'}^\dagger \mathbf{M}_{J'}^\dagger$. Factoring the parenthetical expressions on both sides as block matrices and writing the equation more similarly in form to (6.1.13) give

$$\begin{pmatrix} \mathbf{I}_{\phi_J} \\ -\mathbf{D}_{J'} \mathbf{S}_{J'J} \end{pmatrix}^\dagger \begin{pmatrix} \mathbf{H}_J & \mathbf{H}_{JJ'} \\ \mathbf{H}_{J'J} & \mathbf{H}_{J'} \end{pmatrix} \begin{pmatrix} \mathbf{I}_{\phi_J} \\ -\mathbf{D}_{J'} \mathbf{S}_{J'J} \end{pmatrix} \mathbf{M}_J = \begin{pmatrix} \mathbf{I}_{\phi_J} \\ -\mathbf{D}_{J'} \mathbf{S}_{J'J} \end{pmatrix}^\dagger \begin{pmatrix} \mathbf{S}_J \\ \mathbf{S}_{J'J} \end{pmatrix} \mathbf{M}_J \boldsymbol{\varepsilon}_J \tag{6.1.16}$$

which can be solved using a conventional implementation now that the equation no longer has bra-ket matrices. (6.1.16) is the same eigenvalue equation as derived by Nagata et al. [81] but with (6.1.10) as the starting equation. Since bra-ket matrices are utilized throughout the derivation, (6.1.16) is applicable to multi-component systems without first deriving for the binary system as was originally done by Nagata et al. [81].

The increase in complexity from (6.1.13) to (6.1.16) is manifested in implementation as well as formulation. A conventional implementation without bra-ket matrices would most likely need to construct the block matrices in (6.1.16) via extracting and inserting blocks in a mosaic manner. On the other hand, (6.1.13) can be readily constructed from just sums and products of bra-ket matrices without the much error-prone bookkeeping and buffer management associated with block manipulation.

The process of LP SCF MI repeats until self-consistency of the molecular orbitals is achieved, which can be checked for similarity to

$$\mathbf{\Psi}_{J'}^\dagger \left(1 - \hat{P}_{J'}\right) \mathbf{\Psi}_J = \mathbf{0} \tag{6.1.17}$$

for all J. To prove (6.1.17), $\hat{P}_{J'}$ is expressed in bra-ket matrices using (6.1.6), and the left-hand side is distributed:

$$\boldsymbol{\Psi}_{J'}^{\dagger}\left(1-\hat{P}_{J'}\right)\boldsymbol{\Psi}_{J}=\boldsymbol{\Psi}_{J'}^{\dagger}\left(1-\boldsymbol{\Psi}_{J'}\mathbf{T}_{\mathrm{W},J'}\mathbf{T}_{\mathrm{W},J'}^{\dagger}\boldsymbol{\Psi}_{J'}^{\dagger}\right)\boldsymbol{\Psi}_{J} \tag{6.1.18a}$$

$$=\boldsymbol{\Psi}_{J'}^{\dagger}\boldsymbol{\Psi}_{J}-\left(\boldsymbol{\Psi}_{J'}^{\dagger}\boldsymbol{\Psi}_{J'}\right)\left(\mathbf{T}_{\mathrm{W},J'}\mathbf{T}_{\mathrm{W},J'}^{\dagger}\right)\boldsymbol{\Psi}_{J'}^{\dagger}\boldsymbol{\Psi}_{J} \tag{6.1.18b}$$

$$=\boldsymbol{\Psi}_{J'}^{\dagger}\boldsymbol{\Psi}_{J}-\boldsymbol{\sigma}_{J'}\boldsymbol{\sigma}_{J'}^{-1}\boldsymbol{\Psi}_{J'}^{\dagger}\boldsymbol{\Psi}_{J} \tag{6.1.18c}$$

$$=\boldsymbol{\Psi}_{J'}^{\dagger}\boldsymbol{\Psi}_{J}-\boldsymbol{\Psi}_{J'}^{\dagger}\boldsymbol{\Psi}_{J} \tag{6.1.18d}$$

$$=\mathbf{0} \tag{6.1.18e}$$

where the overlap-equivalence property (5.2.16) is used. (6.1.17) can also be used to prove the counterintuitive inequality of $1-\hat{P}_{J'}\neq\hat{P}_{J}$, thereby further justifying the form of (6.1.13). Using proof by contradiction, assume that $1-\hat{P}_{J'}=\hat{P}_{J}$, and substitute it in the left-hand side of (6.1.17):

$$\boldsymbol{\Psi}_{J'}^{\dagger}\left(1-\hat{P}_{J'}\right)\boldsymbol{\Psi}_{J}\implies\boldsymbol{\Psi}_{J'}^{\dagger}\hat{P}_{J}\boldsymbol{\Psi}_{J} \tag{6.1.19a}$$

$$=\boldsymbol{\Psi}_{J'}^{\dagger}\left(\boldsymbol{\Psi}_{J}\mathbf{T}_{\mathrm{W},J}\mathbf{T}_{\mathrm{W},J}^{\dagger}\boldsymbol{\Psi}_{J}^{\dagger}\right)\boldsymbol{\Psi}_{J} \tag{6.1.19b}$$

$$=\boldsymbol{\Psi}_{J'}^{\dagger}\boldsymbol{\Psi}_{J}\left(\mathbf{T}_{\mathrm{W},J}\mathbf{T}_{\mathrm{W},J}^{\dagger}\right)\left(\boldsymbol{\Psi}_{J}^{\dagger}\boldsymbol{\Psi}_{J}\right) \tag{6.1.19c}$$

$$=\boldsymbol{\Psi}_{J'}^{\dagger}\boldsymbol{\Psi}_{J}\boldsymbol{\sigma}_{J}^{-1}\boldsymbol{\sigma}_{J} \tag{6.1.19d}$$

$$=\boldsymbol{\Psi}_{J'}^{\dagger}\boldsymbol{\Psi}_{J} \tag{6.1.19e}$$

Since $\boldsymbol{\Psi}_{J'}^{\dagger}\boldsymbol{\Psi}_{J}\neq\mathbf{0}$ due to the nonorthogonality of the molecular orbitals, the logical statement of (6.1.19a) leads to a contradiction with (6.1.17). Therefore, the assumption that $1-\hat{P}_{J'}=\hat{P}_{J}$ must be false.

6.2 Localized Molecular Orbitals (LMO) SCF MI

LMO SCF MI was developed by Stoll et al. [79] and uses a constrained energy minimization that produces orthogonal molecular orbitals on each fragment expanded only

in the basis functions of the respective fragment. It is the SCF-MI method that is implemented and generalized in this work with the inclusion of occupation numbers. Unlike the original derivation by Stoll et al. [79], LMO SCF MI is derived here using bra-ket matrices and matrix calculus, which together provide a novel and fundamentally different approach that is more mathematically disciplined in the manner of derivation. The working equation of LMO SCF MI is the eigenvalue equation of (6.2.37) with the effective Hamiltonian as (6.2.33).

The original case of a pure state, where the molecular orbitals are fully occupied, is derived first. The derivations for an ensemble state are treated separately in order to demonstrate the additional mathematical complexities for an ensemble state, and how weighted orthogonalization (WO, cf. §5.2) can play a role with the occupation numbers.

Regardless of whether the derivation is for a pure state or an ensemble state, some definitions and expressions common to both are presented first. Matrix derivatives are in numerator layout. Derivations are for one of the spin functions, $\omega \in \{\alpha, \beta\}$ only, but ω is omitted throughout for convenience.

Basis functions and molecular orbitals are denoted, respectively, as $\mathbf{\Phi} = \begin{pmatrix} |\phi_1\rangle & |\phi_2\rangle & \cdots \end{pmatrix}$ and $\mathbf{\Psi} = \begin{pmatrix} |\psi_1\rangle & |\psi_2\rangle & \cdots \end{pmatrix}$, both of which are ket matrices (cf. §3). Molecular orbitals are always assumed to be normalized. Dual (also called reciprocal) molecular orbitals are defined as

$$\tilde{\mathbf{\Psi}} \equiv \mathbf{\Psi}\boldsymbol{\sigma}^{-1} \tag{6.2.1}$$

where $\boldsymbol{\sigma} = \mathbf{\Psi}^\dagger\mathbf{\Psi}$ is the overlap matrix of molecular orbitals. The differential of the dual molecular orbitals is

$$\begin{aligned}
\delta\tilde{\mathbf{\Psi}} &= (\delta\mathbf{\Psi})\,\boldsymbol{\sigma}^{-1} + \mathbf{\Psi}\delta\boldsymbol{\sigma}^{-1} && \text{(6.2.2a)}\\
&= (\delta\mathbf{\Psi})\,\boldsymbol{\sigma}^{-1} - \mathbf{\Psi}\boldsymbol{\sigma}^{-1}\,(\delta\boldsymbol{\sigma})\,\boldsymbol{\sigma}^{-1} && \text{(6.2.2b)}\\
&= \left(\delta\mathbf{\Psi} - \mathbf{\Psi}\boldsymbol{\sigma}^{-1}\delta\boldsymbol{\sigma}\right)\boldsymbol{\sigma}^{-1} && \text{(6.2.2c)}\\
&= \left(\delta\mathbf{\Psi} - \tilde{\mathbf{\Psi}}\delta\boldsymbol{\sigma}\right)\boldsymbol{\sigma}^{-1} && \text{(6.2.2d)}
\end{aligned}$$

where the matrix differential

$$\delta \mathbf{A}^{-1} = \mathbf{A}^{-1} \left(\delta \mathbf{A} \right) \mathbf{A}^{-1} \tag{6.2.3}$$

for an inverse matrix is used. The density operator, $\hat{\rho}$, and its differential are

$$\hat{\rho} = \tilde{\mathbf{\Psi}} \mathbf{f} \mathbf{\Psi}^{\dagger} = \mathbf{\Psi} \mathbf{f} \tilde{\mathbf{\Psi}}^{\dagger} \tag{6.2.4a}$$

$$\delta \hat{\rho} = \left(\delta \tilde{\mathbf{\Psi}} \right) \mathbf{f} \mathbf{\Psi}^{\dagger} + \tilde{\mathbf{\Psi}} \mathbf{f} \delta \mathbf{\Psi}^{\dagger} \tag{6.2.4b}$$

where $\mathbf{f}$ is a square diagonal matrix of occupation numbers and is assumed to be constant with respect to an infinitesimal change in the molecular orbitals. $\mathbf{f}$ is an identity matrix when at a pure state but not so for an ensemble state. The energy, E, to be minimized and its differential are

$$E = \mathrm{tr} \left(\hat{H} \hat{\rho} \right) \tag{6.2.5a}$$

$$\delta E = \delta \, \mathrm{tr} \left(\hat{H} \hat{\rho} \right) = \mathrm{tr} \left(\hat{H} \delta \hat{\rho} \right) \tag{6.2.5b}$$

where the Hamiltonian, $\hat{H}$, is treated as a constant with respect to the differential. The goal of LMO SCF MI is to find the energy minimum with respect to the localized molecular orbitals as

$$\frac{\partial E}{\partial \mathbf{M}} = \mathbf{0} \tag{6.2.6}$$

where $\mathbf{M}$ is the coefficient matrix of the localized molecular orbitals expanded in the basis functions of their respective fragments only and serves as the constraint in the energy minimization. (6.2.6) is the stationary point problem of LMO SCF MI, and an analytical expression of it is separately derived for a pure state and an ensemble state.

6.2.1 Energy Minimization for Pure States

The derivative of the energy with respect to a molecular orbital is derived with the assumption of a pure state as in Stoll et al. [79]. Because of the idempotency of the density operator, the density operator becomes mathematically indistinguishable from

the projection operator. The result of such a derivation prohibits it from being adapted to an ensemble state with occupation numbers that can be fractional. Nevertheless, the derivation for a pure state is presented first in order to illustrate the difficulties that arise from considering a nonidempotent density operator later in §6.2.2.

Proceeding from (6.2.2d), the differential of the overlap matrix must be replaced, which can be done with an additional independent equation. An independent equation can be formulated by applying the density operator (with $\mathbf{f}$ being an identity matrix) to the dual molecular orbitals and then taking its differential:

$$\hat{\rho}\tilde{\mathbf{\Psi}} = \tilde{\mathbf{\Psi}} \tag{6.2.7a}$$

$$(\delta\hat{\rho})\,\tilde{\mathbf{\Psi}} = \delta\tilde{\mathbf{\Psi}} - \hat{\rho}\delta\tilde{\mathbf{\Psi}} \tag{6.2.7b}$$

$$= (1-\hat{\rho})\,\delta\tilde{\mathbf{\Psi}} \tag{6.2.7c}$$

$$= (1-\hat{\rho})\left(\delta\mathbf{\Psi} - \tilde{\mathbf{\Psi}}\delta\boldsymbol{\sigma}\right)\boldsymbol{\sigma}^{-1} \tag{6.2.7d}$$

$$= (1-\hat{\rho})\,(\delta\mathbf{\Psi})\,\boldsymbol{\sigma}^{-1} - (1-\hat{\rho})\,\tilde{\mathbf{\Psi}}\,(\delta\boldsymbol{\sigma})\,\boldsymbol{\sigma}^{-1} \tag{6.2.7e}$$

$$= (1-\hat{\rho})\,(\delta\mathbf{\Psi})\,\boldsymbol{\sigma}^{-1} \tag{6.2.7f}$$

where the last equation results from $(1-\hat{\rho})\,\tilde{\mathbf{\Psi}} = \mathbf{0}$. Expanding and distributing the differential of the density operator, $\delta\hat{\rho}$, produce

$$\delta\tilde{\mathbf{\Psi}} + \tilde{\mathbf{\Psi}}\,(\delta\mathbf{\Psi})^{\dagger}\,\tilde{\mathbf{\Psi}} = (1-\hat{\rho})\,(\delta\mathbf{\Psi})\,\boldsymbol{\sigma}^{-1} \tag{6.2.8a}$$

$$\delta\tilde{\mathbf{\Psi}} = (1-\hat{\rho})\,(\delta\mathbf{\Psi})\,\boldsymbol{\sigma}^{-1} - \tilde{\mathbf{\Psi}}\,(\delta\mathbf{\Psi})^{\dagger}\,\tilde{\mathbf{\Psi}} \tag{6.2.8b}$$

which is an expression of the differential of dual molecular orbitals without the differential of the molecular-orbital overlap. Substituting (6.2.8b) into (6.2.5b) for minimizing

the energy, while setting $\mathbf{f}$ to be an identity, gives

$$\delta E = \mathrm{tr}\left(\hat{H}\left(\delta\tilde{\mathbf{\Psi}}\right)\mathbf{\Psi}^{\dagger}\right) + \mathrm{tr}\left(\hat{H}\tilde{\mathbf{\Psi}}\left(\delta\mathbf{\Psi}\right)^{\dagger}\right) \tag{6.2.9a}$$

$$= \mathrm{tr}\left(\hat{H}\left(1-\hat{\rho}\right)\left(\delta\mathbf{\Psi}\right)\boldsymbol{\sigma}^{-1}\mathbf{\Psi}^{\dagger} - \hat{H}\tilde{\mathbf{\Psi}}\left(\delta\mathbf{\Psi}\right)^{\dagger}\tilde{\mathbf{\Psi}}\mathbf{\Psi}^{\dagger}\right) + \mathrm{tr}\left(\hat{H}\tilde{\mathbf{\Psi}}\left(\delta\mathbf{\Psi}\right)^{\dagger}\right) \tag{6.2.9b}$$

$$= \mathrm{tr}\left(\hat{H}\left(1-\hat{\rho}\right)\left(\delta\mathbf{\Psi}\right)\tilde{\mathbf{\Psi}}^{\dagger}\right) - \mathrm{tr}\left(\hat{H}\tilde{\mathbf{\Psi}}\left(\delta\mathbf{\Psi}\right)^{\dagger}\hat{\rho}\right) + \mathrm{tr}\left(\hat{H}\tilde{\mathbf{\Psi}}\left(\delta\mathbf{\Psi}\right)^{\dagger}\right) \tag{6.2.9c}$$

Since factors in a trace commute as long as they remain multiplicatively compatible and by (6.2.7a), the last two terms cancel each other out to yield

$$\delta E = \mathrm{tr}\left(\hat{H}\left(1-\hat{\rho}\right)\left(\delta\mathbf{\Psi}\right)\tilde{\mathbf{\Psi}}^{\dagger}\right) \tag{6.2.10a}$$

$$= \sum_{k}\langle\tilde{\psi}_k|\,\hat{H}\left(1-\hat{\rho}\right)\,|\delta\psi_k\rangle \tag{6.2.10b}$$

which is the total differential of the energy. The partial derivative of the energy with respect to one of the molecular orbitals, then, is

$$\frac{\delta E}{\delta\psi}_{i} = \langle\tilde{\psi}_i|\,\hat{H}\left(1-\hat{\rho}\right) \tag{6.2.11}$$

Since $|\psi_i\rangle = \mathbf{\Phi}\mathbf{m}_i \implies \partial\psi_i/\partial\mathbf{m}_i = \mathbf{\Phi}$ and by the chain rule,

$$\frac{\partial E}{\partial\mathbf{m}_i} = \langle\tilde{\psi}_i|\,\hat{H}\left(1-\hat{\rho}\right)\mathbf{\Phi} \tag{6.2.12}$$

Extending to all molecular orbitals gives

$$\frac{\partial E}{\partial\mathbf{M}} = \tilde{\mathbf{\Psi}}^{\dagger}\hat{H}\left(1-\hat{\rho}\right)\mathbf{\Phi} \tag{6.2.13}$$

which is set to zero to obtain the stationary point (6.2.6).

6.2.2 Energy Minimization for Ensemble States

In §6.2.1, the derivative of the energy with respect to a molecular orbital was derived with the assumption of a pure state as in Stoll et al. [79]. For an ensemble state, the density operator is no longer idempotent, and the equivalency between it and the projection operator breaks down. With the density operator being nonidempotent, the

occupation numbers can be fractional and must be taken into account. Stoll et al. [79] never considered this case of having an explicit set of occupation numbers. By assuming a pure state, the original derivation by Stoll et al. [79] conveniently avoids the difficulties associated with a nonidempotent density operator altogether.

It might be tempting to simply include the occupation numbers in the density operator in (6.2.13). However, such incorporation would be naively invalid, since the assumption that the density operator is idempotent was made throughout its derivation. In fact, it is not possible to determine how the occupation numbers should be incorporated through inspection alone. The stationary point (6.2.6) for an ensemble state must be derived anew without assuming idempotency of the density operator. By treating the density operator as nonidempotent, the occupation numbers are mathematically incorporated, and the role of the projection operator is made explicit.

Proceeding from (6.2.2d), the differential of the overlap matrix must be replaced, which can be done with an additional independent equation as in §6.2.1. An independent equation can be formulated by applying the nonidempotent density operator to the dual molecular orbitals and then taking its differential:

$$\hat{\rho}\tilde{\mathbf{\Psi}} = \tilde{\mathbf{\Psi}}\mathbf{f} \tag{6.2.14a}$$

$$(\delta\hat{\rho})\,\tilde{\mathbf{\Psi}} = \left(\delta\tilde{\mathbf{\Psi}}\right)\mathbf{f} - \hat{\rho}\delta\tilde{\mathbf{\Psi}} \tag{6.2.14b}$$

$$= \left(\delta\tilde{\mathbf{\Psi}}\right)\mathbf{f} - \hat{\rho}\left(\delta\mathbf{\Psi} - \tilde{\mathbf{\Psi}}\delta\boldsymbol{\sigma}\right)\boldsymbol{\sigma}^{-1} \tag{6.2.14c}$$

$$= \left(\delta\tilde{\mathbf{\Psi}}\right)\mathbf{f} - \left(\hat{\rho}\delta\mathbf{\Psi} - \tilde{\mathbf{\Psi}}\mathbf{f}\delta\boldsymbol{\sigma}\right)\boldsymbol{\sigma}^{-1} \tag{6.2.14d}$$

where $\mathbf{f}$ is not necessarily an identity matrix. Unlike the case for a pure state, an explicit expression for the differential of molecular-orbital overlap, $\delta\boldsymbol{\sigma}$, is first obtained

by expanding and distributing the differential of the density operator, $\delta\hat{\rho}$:

$$\left(\delta\tilde{\mathbf{\Psi}}\right)\mathbf{f} + \tilde{\mathbf{\Psi}}\mathbf{f}\left(\delta\mathbf{\Psi}\right)^{\dagger}\tilde{\mathbf{\Psi}} = \left(\delta\tilde{\mathbf{\Psi}}\right)\mathbf{f} - \left(\hat{\rho}\delta\mathbf{\Psi} - \tilde{\mathbf{\Psi}}\mathbf{f}\delta\boldsymbol{\sigma}\right)\boldsymbol{\sigma}^{-1} \tag{6.2.15a}$$

$$\tilde{\mathbf{\Psi}}\mathbf{f}\left(\delta\mathbf{\Psi}\right)^{\dagger}\tilde{\mathbf{\Psi}} = -\left(\hat{\rho}\delta\mathbf{\Psi} - \tilde{\mathbf{\Psi}}\mathbf{f}\delta\boldsymbol{\sigma}\right)\boldsymbol{\sigma}^{-1} \tag{6.2.15b}$$

$$\tilde{\mathbf{\Psi}}\mathbf{f}\left(\delta\mathbf{\Psi}\right)^{\dagger}\mathbf{\Psi} = -\left(\hat{\rho}\delta\mathbf{\Psi} - \tilde{\mathbf{\Psi}}\mathbf{f}\delta\boldsymbol{\sigma}\right) \tag{6.2.15c}$$

$$\tilde{\mathbf{\Psi}}\mathbf{f}\delta\boldsymbol{\sigma} = \tilde{\mathbf{\Psi}}\mathbf{f}\left(\delta\mathbf{\Psi}\right)^{\dagger}\mathbf{\Psi} + \hat{\rho}\delta\mathbf{\Psi} \tag{6.2.15d}$$

$$\delta\boldsymbol{\sigma} = \left(\delta\mathbf{\Psi}\right)^{\dagger}\mathbf{\Psi} + \mathbf{f}^{-1}\mathbf{\Psi}^{\dagger}\hat{\rho}\delta\mathbf{\Psi} \tag{6.2.15e}$$

To remove $\delta\boldsymbol{\sigma}$ in (6.2.2d), (6.2.15e) is substituted into it to give

$$\delta\tilde{\mathbf{\Psi}} = \left(\delta\mathbf{\Psi}\right)\boldsymbol{\sigma}^{-1} - \tilde{\mathbf{\Psi}}\left(\delta\mathbf{\Psi}\right)^{\dagger}\mathbf{\Psi}\boldsymbol{\sigma}^{-1} - \tilde{\mathbf{\Psi}}\mathbf{f}^{-1}\mathbf{\Psi}^{\dagger}\hat{\rho}\left(\delta\mathbf{\Psi}\right)\boldsymbol{\sigma}^{-1} \tag{6.2.16a}$$

$$= \left(1 - \tilde{\mathbf{\Psi}}\mathbf{f}^{-1}\mathbf{\Psi}^{\dagger}\hat{\rho}\right)\left(\delta\mathbf{\Psi}\right)\boldsymbol{\sigma}^{-1} - \tilde{\mathbf{\Psi}}\left(\delta\mathbf{\Psi}\right)^{\dagger}\tilde{\mathbf{\Psi}} \tag{6.2.16b}$$

$$= \left(1 - \hat{P}\right)\left(\delta\mathbf{\Psi}\right)\boldsymbol{\sigma}^{-1} - \tilde{\mathbf{\Psi}}\left(\delta\mathbf{\Psi}\right)^{\dagger}\tilde{\mathbf{\Psi}} \tag{6.2.16c}$$

where the projection operator, $\hat{P}$, is defined as

$$\hat{P} \equiv \tilde{\mathbf{\Psi}}\mathbf{f}^{-1}\mathbf{\Psi}^{\dagger}\hat{\rho} = \tilde{\mathbf{\Psi}}\mathbf{\Psi}^{\dagger} \tag{6.2.17}$$

and suggests that molecular orbitals with zero occupation numbers cannot be in $\mathbf{\Psi}$. Throughout the optimization process, the number of molecular orbitals in $\mathbf{\Psi}$ and the number of occupation numbers in $\mathbf{f}$ are allow to vary accordingly depending on whether an occupation is zero. Substitute (6.2.16c) into (6.2.5b) for minimizing the energy:

$$\delta E = \mathrm{tr}\left(\hat{H}\left(\delta\tilde{\mathbf{\Psi}}\right)\mathbf{f}\mathbf{\Psi}^{\dagger}\right) + \mathrm{tr}\left(\hat{H}\tilde{\mathbf{\Psi}}\mathbf{f}\left(\delta\mathbf{\Psi}\right)^{\dagger}\right) \tag{6.2.18a}$$

$$= \mathrm{tr}\left(\hat{H}\left(1 - \hat{P}\right)\left(\delta\mathbf{\Psi}\right)\boldsymbol{\sigma}^{-1}\mathbf{f}\mathbf{\Psi}^{\dagger} - \hat{H}\tilde{\mathbf{\Psi}}\left(\delta\mathbf{\Psi}\right)^{\dagger}\tilde{\mathbf{\Psi}}\mathbf{f}\mathbf{\Psi}^{\dagger}\right) + \mathrm{tr}\left(\hat{H}\tilde{\mathbf{\Psi}}\mathbf{f}\left(\delta\mathbf{\Psi}\right)^{\dagger}\right) \tag{6.2.18b}$$

$$= \mathrm{tr}\left(\hat{H}\left(1 - \hat{P}\right)\left(\delta\mathbf{\Psi}\right)\mathbf{f}\tilde{\mathbf{\Psi}}^{\dagger}\right) - \mathrm{tr}\left(\hat{H}\tilde{\mathbf{\Psi}}\left(\delta\mathbf{\Psi}\right)^{\dagger}\hat{\rho}\right) + \mathrm{tr}\left(\hat{H}\tilde{\mathbf{\Psi}}\mathbf{f}\left(\delta\mathbf{\Psi}\right)^{\dagger}\right) \tag{6.2.18c}$$

Since factors in a trace commute as long as they remain multiplicatively compatible and by (6.2.14a), the last two terms cancel each other out to yield

$$\delta E = \mathrm{tr}\left(\hat{H}\left(1-\hat{P}\right)\left(\delta\boldsymbol{\Psi}\right)\mathbf{f}\tilde{\boldsymbol{\Psi}}^{\dagger}\right) \tag{6.2.19a}$$

$$= \sum_{k} f_k \left\langle\tilde{\psi}_k\right| \hat{H}\left(1-\hat{P}\right)\left|\delta\psi_k\right\rangle \tag{6.2.19b}$$

which is the total differential of the energy. The partial derivative of the energy with respect to one of the molecular orbitals, then, is

$$\frac{\delta E}{\delta\psi_i} = f_i \left\langle\tilde{\psi}_i\right| \hat{H}\left(1-\hat{P}\right) \tag{6.2.20}$$

Since $|\psi_i\rangle = \boldsymbol{\Phi}\mathbf{m}_i \implies \partial\psi_i/\partial\mathbf{m}_i = \boldsymbol{\Phi}$ and by the chain rule,

$$\frac{\partial E}{\partial\mathbf{m}_i} = f_i \left\langle\tilde{\psi}_i\right| \hat{H}\left(1-\hat{P}\right)\boldsymbol{\Phi} \tag{6.2.21}$$

Extending to all molecular orbitals gives

$$\frac{\partial E}{\partial\mathbf{M}} = \mathbf{f}\tilde{\boldsymbol{\Psi}}^{\dagger}\hat{H}\left(1-\hat{P}\right)\boldsymbol{\Phi} \tag{6.2.22}$$

which is set to zero to obtain the stationary point (6.2.6). Note where the occupation numbers are placed and how the density operator, $\hat{\rho}$, in (6.2.13) is replaced by the projection operation, $\hat{P}$. Occupation numbers are fixed with respect to the equations of SCF MI but are instead optimized by, for instance, ensemble DFT (EDFT, discussed in §8) as part of its energy minimization process. Since a pure state is a special case of an ensemble state, the derivative of the energy as (6.2.22) is used henceforth.

6.2.3 Orbital Orthogonality and Partial Star Operator

SCF MI involves equations that relate to fragments. Hence, it is useful to define a matrix that can select consecutive columns that correspond to a fragment, while removing the leading and trailing columns. Such a selection matrix for Fragment J at consecutive

columns would be defined as

$$\mathbf{\Xi}_J = \begin{pmatrix} \mathbf{0} \\ \mathbf{I}_J \\ \mathbf{0} \end{pmatrix} \tag{6.2.23}$$

where the numbers of rows in the top and bottom zero blocks are the numbers of columns before and after the columns of Fragment J, respectively. $\mathbf{\Xi}_J$ has orthonormal columns (i.e., $\mathbf{\Xi}_J^{\mathrm{T}}\mathbf{\Xi}_J = \mathbf{I}_J$) and selects the columns of Fragment J in $\mathbf{A}$ as $\mathbf{A}\mathbf{\Xi}_J$. Correspondingly, $\mathbf{\Xi}_J^{\mathrm{T}}\mathbf{A}$ has the rows of $\mathbf{A}$ being selected instead.

Orthogonalization of molecular orbitals for LMO SCF MI is generalized to allow methods other than symmetric orthogonalization. Orthonormal molecular orbitals are denoted as

$$\mathbf{\Psi}_* \equiv \mathbf{\Psi}\mathbf{T}_{\mathrm{W}} \tag{6.2.24}$$

where $\mathbf{T}_{\mathrm{W}}$ is the transformation matrix of weighted orthogonalization (WO, cf. §5.2) with occupation numbers as weights. The orthonormal molecular orbitals localized to Fragment J are

$$\mathbf{\Psi}_{J*} \equiv \mathbf{\Psi}_*\mathbf{\Xi}_J \tag{6.2.25}$$

It is important to note that the orthogonality of $\mathbf{\Psi}_{J*}$ arises from across all fragments and is not specific to Fragment J. In other words, the fact that $\mathbf{\Psi}_{J*}^\dagger\mathbf{\Psi}_{J*}$ is an identity comes as a consequence of $\mathbf{\Psi}_*^\dagger\mathbf{\Psi}_*$ being an identity:

$$\mathbf{\Psi}_{J*}^\dagger\mathbf{\Psi}_{J*} = \mathbf{\Xi}_J^{\mathrm{T}}\mathbf{\Psi}_*^\dagger\mathbf{\Psi}_*\mathbf{\Xi}_J \tag{6.2.26a}$$

$$= \mathbf{\Xi}_J^{\mathrm{T}}\mathbf{\Xi}_J \tag{6.2.26b}$$

$$= \mathbf{I}_J \tag{6.2.26c}$$

In order to construct an effective Hamiltonian that is Hermitian (§6.2.4), an operator, $\hat{\Omega}_J$, called the partial star operator for Fragment J is defined as

$$\hat{\Omega}_J \equiv \mathbf{\Psi}_{J*}\mathbf{\Psi}_J^\dagger \tag{6.2.27a}$$

$$= \mathbf{\Psi}\mathbf{T}_\mathrm{W}\mathbf{\Xi}_J\mathbf{\Xi}_J^\mathrm{T}\mathbf{\Psi}^\dagger \tag{6.2.27b}$$

which is based on what Stoll et al. [79] defines and calls the partial density matrix, $\rho^{(J)}$:

$$\rho^{(J)} \equiv \tilde{\mathbf{\Psi}}_J\mathbf{\Psi}_J^\dagger \tag{6.2.28a}$$

$$= \mathbf{\Psi}\sigma^{-1}\mathbf{\Xi}_J\mathbf{\Xi}_J^\mathrm{T}\mathbf{\Psi}^\dagger \tag{6.2.28b}$$

$$= \mathbf{\Psi}\mathbf{T}_\mathrm{W}\mathbf{T}_\mathrm{W}^\dagger\mathbf{\Xi}_J\mathbf{\Xi}_J^\mathrm{T}\mathbf{\Psi}^\dagger \tag{6.2.28c}$$

where the overlap-equivalence property (5.2.16) is invoked. However, the partial density matrix is not used, since the dual molecular orbitals, $\tilde{\mathbf{\Psi}}$, in the original stationary point of Stoll et al. [79] are replaced by $\mathbf{\Psi}_*$ in this work. Another related reason for not using the partial density matrix is that $\mathbf{T}_\mathrm{W}$ would have to be explicitly known, which can be easily determined by treating $\mathbf{\Psi}\mathbf{T}_\mathrm{W} = \mathbf{\Psi}_*$ as a system of equations but just causes unnecessary computation in the implementation. Furthermore, partial density matrix is a misnomer due to it being neither a matrix nor Hermitian, and it actually acts like a projection operator other than a density operator when the system is not a pure state. Unlike the partial density matrix, the partial star operator is not idempotent. Like the partial density matrix, the partial star operator is not Hermitian. The partial star operator is called as such, because it puts or removes the asterisk next to the fragment label of the operand.

The partial star operator has the property of

$$\hat{\Omega}_J\mathbf{\Psi}_J = \mathbf{\Psi}_{J*}\left(\mathbf{\Psi}_J^\dagger\mathbf{\Psi}_J\right) \tag{6.2.29a}$$

$$= \mathbf{\Psi}_{J*}\mathbf{I}_J \tag{6.2.29b}$$

$$= \mathbf{\Psi}_{J*} \tag{6.2.29c}$$

which puts a star in the notation. The assumption that $\mathbf{\Psi}_J^\dagger \mathbf{\Psi}_J$ is an identity comes from Stoll et al. [79] and is justified by circular reasoning that the effective Hamiltonian for Fragment J will be Hermitian (6.2.33), which means the fragment-localized molecular orbitals solved from it are orthogonal and $\mathbf{\Psi}_J$ would have orthonormal orbitals after normalization. The counterpart property is

$$\hat{\Omega}_J^\dagger \mathbf{\Psi}_{J*} = \mathbf{\Psi}\mathbf{\Xi}_J \mathbf{\Xi}_J^\mathsf{T} \mathbf{T}_\mathrm{W}^\dagger \mathbf{\Psi}^\dagger \mathbf{\Psi} \mathbf{T}_\mathrm{W} \mathbf{\Xi}_J \tag{6.2.30a}$$

$$= \mathbf{\Psi}\mathbf{\Xi}_J \mathbf{\Xi}_J^\mathsf{T} \mathbf{\Xi}_J \tag{6.2.30b}$$

$$= \mathbf{\Psi}\mathbf{\Xi}_J \tag{6.2.30c}$$

$$= \mathbf{\Psi}_J \tag{6.2.30d}$$

which removes the star in the notation. Along with the selection matrix, these two properties of partial star operator are used in constructing an effective Hamiltonian for each fragment in LMO SCF MI (§6.2.4).

6.2.4 Eigenvalue Equation

The stationary point of (6.2.6) using the derivative of the energy for an ensemble state (6.2.22) must be expressed in the form of an eigenvalue equation. Although an optimization method could use the derivative to find the energy minimum, the occupation numbers, which are determined from the Fermi-Dirac distribution using orbital energies, would not be available. Therefore, an eigenvalue equation where the molecular orbitals and associated orbital energies as eigenvalues can be solved from an effective Hamiltonian is still required.

Using the derivative of the energy for an ensemble state, the stationary point is

$$\mathbf{\Phi}^\dagger \left(1 - \hat{P}\right) \hat{H} \mathbf{\Psi}_* = \mathbf{0} \tag{6.2.31}$$

where $\mathbf{f}$ and $\mathbf{T}_\mathrm{W}^\dagger$ are respectively canceled out by multiplying their inverses.

Multiplying by the selection matrix (6.2.23), the stationary point for Fragment J is

$$\boldsymbol{\Xi}_J^{\mathrm{T}} \boldsymbol{\Phi}^{\dagger} \left(1 - \hat{P}\right) \hat{H} \boldsymbol{\Psi}_* \boldsymbol{\Xi}_J = \mathbf{0} \tag{6.2.32a}$$

$$\boldsymbol{\Phi}_J^{\dagger} \left(1 - \hat{P}\right) \hat{H} \boldsymbol{\Psi}_{J*} = \mathbf{0} \tag{6.2.32b}$$

With the stationary point (6.2.32b) and partial star operator (6.2.27) established, an effective Hamiltonian that is Hermitian can be constructed. The goal is to cast (6.2.31) into an eigenvalue equation such that $\boldsymbol{\Psi}_J$ contains the eigenfunctions and $\boldsymbol{\varepsilon}_J$ contains the associated orbital energies.

By inspection [79], the effective Hamiltonian for Fragment J, $\hat{\tilde{H}}_J$, is preemptively defined as

$$\hat{\tilde{H}}_J \equiv \left(1 - \hat{P} + \hat{\Omega}_J^{\dagger}\right) \hat{H} \left(1 - \hat{P} + \hat{\Omega}_J\right) \tag{6.2.33}$$

which is Hermitian and is defined differently than in Stoll et al. [79] so as to accommodate WO. Its role as an effective Hamiltonian is validated by direct proof. The eigenfunctions and eigenvalues of $\hat{\tilde{H}}_J$ are determined from

$$\hat{\tilde{H}}_J \boldsymbol{\Psi}_J = \boldsymbol{\Psi}_J \boldsymbol{\varepsilon}_J \tag{6.2.34}$$

To see how (6.2.34) can satisfy the stationary point (6.2.31), the left-hand side is expanded and distributed:

$$\begin{aligned}
\hat{\tilde{H}}_J \boldsymbol{\Psi}_J &= \left(1 - \hat{P} + \hat{\Omega}_J^{\dagger}\right) \hat{H} \left(1 - \hat{P} + \hat{\Omega}_J\right) \boldsymbol{\Psi}_J && \text{(6.2.35a)} \\
&= \left(1 - \hat{P} + \hat{\Omega}_J^{\dagger}\right) \hat{H} \left(\boldsymbol{\Psi}_J - \hat{P}\boldsymbol{\Psi}_J + \hat{\Omega}_J \boldsymbol{\Psi}_J\right) && \text{(6.2.35b)} \\
&= \left(1 - \hat{P} + \hat{\Omega}_J^{\dagger}\right) \hat{H} \boldsymbol{\Psi}_{J*} && \text{(6.2.35c)} \\
&= \left(1 - \hat{P}\right) \hat{H} \boldsymbol{\Psi}_{J*} + \hat{\Omega}_J^{\dagger} \hat{H} \boldsymbol{\Psi}_{J*} && \text{(6.2.35d)} \\
&= \left(1 - \hat{P}\right) \hat{H} \boldsymbol{\Psi}_{J*} + \hat{\Omega}_J^{\dagger} \boldsymbol{\Psi}_{J*} \boldsymbol{\varepsilon}_J && \text{(6.2.35e)} \\
&= \left(1 - \hat{P}\right) \hat{H} \boldsymbol{\Psi}_{J*} + \boldsymbol{\Psi}_J \boldsymbol{\varepsilon}_J && \text{(6.2.35f)}
\end{aligned}$$

where $\hat{P}\mathbf{\Psi}_J = \mathbf{\Psi}_J$, and $\hat{H}\mathbf{\Psi}_{J*} = \mathbf{\Psi}_{J*}\boldsymbol{\varepsilon}_J$ (from the variational principle with $\boldsymbol{\varepsilon}_J$ as the Lagrange multiplier). Because of (6.2.34), (6.2.35f) is equal to $\mathbf{\Psi}_J\boldsymbol{\varepsilon}_J$. Therefore,

$$\left(1-\hat{P}\right)\hat{H}\mathbf{\Psi}_{J*} = \mathbf{0} \tag{6.2.36}$$

which is the stationary point (6.2.31) and concludes the direct proof that (6.2.33) is a definition of an effective Hamiltonian that is Hermitian and whose eigenfunctions satisfy the stationary condition.

If an implementation employs bra-ket matrices (cf. §3), the eigenvalue equation to solve is simply (6.2.34) with $\mathbf{\Phi}_J^\dagger$ multiplied from the left:

$$\mathbf{\Phi}_J^\dagger\hat{\hat{H}}_J\mathbf{\Phi}_J\mathbf{M}_J = \mathbf{S}_J\mathbf{M}_J\boldsymbol{\varepsilon}_J \tag{6.2.37}$$

where $\mathbf{S}_J = \mathbf{\Phi}_J^\dagger\mathbf{\Phi}_J$, and $\mathbf{M}_J$ is the coefficient matrix of $\mathbf{\Psi}_J$ expanded in $\mathbf{\Phi}_J$. However, if an implementation is a conventional one that does not use bra-ket matrices, then the operators in $\hat{\hat{H}}_J$ need to be reformulated as matrix representations in $\mathbf{\Phi}_J$. The matrix representations are obtained by first expanding $\hat{\hat{H}}_J$ into its constituent operators as

$$\begin{aligned}\hat{\hat{H}}_J = \hat{H} - \hat{H}\hat{P} + \hat{H}\hat{\Omega}_J \\ - \hat{P}\hat{H} + \hat{P}\hat{H}\hat{P} - \hat{P}\hat{H}\hat{\Omega}_J \\ + \hat{\Omega}_J^\dagger\hat{H} - \hat{\Omega}_J^\dagger\hat{H}\hat{P} + \hat{\Omega}_J^\dagger\hat{H}\hat{\Omega}_J\end{aligned} \tag{6.2.38}$$

and then expressing them in $\mathbf{\Phi}_J$ to become

$$\begin{aligned}\tilde{\mathbf{H}}_J = \mathbf{\Phi}_J^\dagger\hat{\hat{H}}_J\mathbf{\Phi}_J = \mathbf{H}_J - \mathbf{H}_J\mathbf{\bullet}\mathbf{D}\mathbf{S}_{\bullet J} + \mathbf{H}_J\mathbf{\bullet}\mathbf{D}_J\mathbf{S}_J \\ - \mathbf{S}_J\mathbf{\bullet}\mathbf{D}\mathbf{H}_{\bullet J} + \mathbf{S}_J\mathbf{\bullet}\mathbf{D}\mathbf{H}\mathbf{D}\mathbf{S}_{\bullet J} - \mathbf{S}_J\mathbf{\bullet}\mathbf{D}\mathbf{H}\mathbf{D}_J\mathbf{S}_J \\ + \mathbf{S}_J^\dagger\mathbf{D}_J^\dagger\mathbf{H}_{\bullet J} - \mathbf{S}_J^\dagger\mathbf{D}_J^\dagger\mathbf{H}\mathbf{D}\mathbf{S}_{\bullet J} + \mathbf{S}_J^\dagger\mathbf{D}_J^\dagger\mathbf{H}\mathbf{D}_J\mathbf{S}_J\end{aligned} \tag{6.2.39}$$

with the definitions of

$$\mathbf{S}_{J\bullet} \equiv \mathbf{\Phi}_J^\dagger \mathbf{\Phi} \tag{6.2.40a}$$

$$\mathbf{S}_{\bullet J} \equiv \mathbf{\Phi}^\dagger \mathbf{\Phi}_J \tag{6.2.40b}$$

$$\mathbf{H}_{J\bullet} \equiv \mathbf{\Phi}_J^\dagger \hat{H} \mathbf{\Phi} \tag{6.2.40c}$$

$$\mathbf{H}_{\bullet J} \equiv \mathbf{\Phi}^\dagger \hat{H} \mathbf{\Phi}_J \tag{6.2.40d}$$

$$\mathbf{D} \equiv \mathbf{M}\mathbf{T}_\mathrm{W}\mathbf{T}_\mathrm{W}^\dagger\mathbf{M}^\dagger \tag{6.2.40e}$$

$$\mathbf{D}_J \equiv \mathbf{M}\mathbf{T}_\mathrm{W}\mathbf{\Xi}_J\mathbf{M}_J^\dagger \tag{6.2.40f}$$

(6.2.39) is drastically more complicated than just $\mathbf{\Phi}_J^\dagger \hat{\tilde{H}}_J \mathbf{\Phi}_J$, mainly due to the expansion and distribution of all the operators. The importance of bra-ket matrices in constructing and solving the eigenvalue equation for LMO SCF MI in a direct manner is even more demonstrative compared to LP SCF MI (cf. §6.1). Implementing the effective Hamiltonian as (6.2.39) would involve countless buffers, great difficulty in variable naming, and an extremely convoluted sequence of operations on matrices. In stark contrast, constructing the effective Hamiltonian as an operator using bra-ket matrices in code involves only sums and products directly as how (6.2.33) is mathematically expressed without any extraneous matrix manipulations.

For implementing LMO SCF MI (and similarly for LP SCF MI) using bra-ket matrices in a programming language that supports operator overloading, the effective Hamiltonian (6.2.33) is coded like an ordinary matrix. This is achieved by having all operators implemented as ordinary matrices in code (i.e., not as instances of dedicated or tailored classes) using Cholesky decomposition for the basis functions and then (3.1.4). With the operators stored and manipulated as ordinary matrices, operator overloading is employed to concisely indicate the operations among the operators. For example, the factor, $1 - \hat{P} + \hat{\Omega}_J$, that appears in (6.2.33) would be directly coded as an identity matrix minus the projection operator plus the partial star operator for Fragment J. Multiplying operators is similarly achieved through operator overloading.

Chapter 7

Analysis of DNA Interactions and GC Content with EDA

This adapted chapter was published in the journal Physical Chemistry Chemical Physics (PCCP) of the Royal Society of Chemistry (see Chen and Skylaris [1]).

7.1 Nucleobase Interactions and the Applicability of EDA

Hydrogen bonding represents a significant contribution to the stability of a double-stranded DNA (dsDNA). Adenine-thymine (A-T) contributes two hydrogen bonds, and guanine-cytosine (G-C) contributes three hydrogen bonds. As such, the amount of energy required to denature double-stranded DNA depends on the GC content, which is the percentage of nucleobases that are guanine or cytosine. Base stacking represents another significant contribution due to the π-π interactions [4]. Since base stacking occurs for neighboring base pairs, the interaction energy and stability of a DNA structure does not depend on GC content alone. The ordering of the base pairs in addition to the GC content is therefore also a factor in the stability of DNA.

Due to the importance of interacting biomolecules in a supermolecular system, determining the various factors that contribute to the interaction energy of a biomolecular system would aid in the understanding of some biological phenomena. For instance, mRNA transcription involves the opening and unwinding of the DNA helix by RNA polymerase along with the aid of many transcription factors. The interactions within

and their contributions to the interaction energy of the DNA strands affect the transcription process and efficiency [86]. Another example is CG islands, which are regions of high GC content often associated with the beginning of a gene. GC content affects the interaction energy of the DNA helical region. Since it can be near or within the promoters of many genes, understanding how the GC content affects the interaction energy in CG islands near such genes can elucidate some of the aspects of transcription initiation and promoter escape [87, 88].

Understanding such biomolecular interactions is a motivation for using and furthering computational chemistry methods. Density-functional theory (DFT) examines the electronic structure of chemical systems with many atoms. Due to computational costs, DFT is often applied to small systems that are either simple or simplified models of biomolecules so that biomolecular interactions can be studied and then extrapolated to real systems. An example of such systems is the pairing of stacked amino acids, where their orientations relative to each other determine the stability and interaction energy [5]. Also regarding stacking interactions, drugs fragments and moieties have been studied in the context of binding to different DNA base pairs [6]. Stacking interactions and hydrogen bonding are often the theme in DFT-based studies of biomolecules, since they serve as important noncovalent contributors to the stabilization of the supermolecule.

Often such studies involve very simple or simplified versions of real biomolecules. DFT calculations are expensive, and conventional software packages are cubic-scaling in terms of the computation time it takes and the number of atoms in the system being studied. Biological molecules, such as proteins and nucleic acids, are usually large or part of a larger complex of interacting units, which exceed reasonable limits in the computational time that a cubic-scaling software package takes on such systems.

ONETEP (Order-*N* Electronic Total Energy Package) [8] is a DFT software package based on a plane-wave, pseudo-potential approach that utilizes the electronic localization inherent in systems with a non-vanishing band gap. As such, the computational cost of a ONETEP DFT calculation scales linearly with the number of atoms and the number of processors when parallelized [9]. Due to its linear scaling, ONETEP is suitable for studying biological systems on the order of thousands of atoms [10]. On the other hand, cubic-scaling calculations in general can only handle up to hundreds of

atoms at best. In addition to the size of the system, the variability of a class of systems, such as nucleic acids with different sequences, presents combinatorial issues for setting up and running large number of calculations and is exacerbated if the calculations are cubic-scaling.

DFT has been applied to the study of DNA molecules in the context of ligand complexes and disease prevention. Ligand binding to DNA has impacts on the stability of DNA, such as increasing the susceptibility of DNA to cleavage and altering its thermodynamic properties [89]. Ligand binding to DNA has also been examined for electronic absorption spectra and charge transfer using time-dependent DFT (TDDFT) [90]. However, as noted, such complexes are usually small enough for cubic-scaling calculations.

While the DFT method aims to estimate the total energy of a system, the main objectives of Energy Decomposition Analysis (EDA) is to partition the interaction energy of a multi-fragment supermolecule into their chemical origins [11], such as electrostatics, exchange-correlation contributions, polarization, charge transfer, and other relevant chemical phenomena. Hence, EDA is an important analytical tool that partitions the interaction energy into chemically interpretable components.

EDA is a family of decomposition methods, each of which is known as an EDA scheme. The EDA schemes can be categorized according to the nature of their underlying theory [11]. There are two major categories of EDA schemes: variational-based and perturbation-based. Variational-based schemes are typically derived from the early forms of EDA. The interaction energy is decomposed by the use of intermediate wave functions. LMO [14], ALMO [13], and BLW [15, 16] schemes are in this category. Perturbation-based schemes approach EDA from the popular, symmetry-adapted perturbation theory (SAPT) scheme [91, 92]. The interactions among the fragments are seen as perturbations to the non-interacting description and are constructed as corrections resulting from different physical effects. EDA can also facilitate the creation of new force fields in molecular mechanics by parameterization against EDA data, thereby yielding force fields that are more accurate and transferable [93, 94].

There have been other works on applying DFT and EDA to simple biomolecules in understanding some of the stabilization interactions common in biological systems and with drugs. Usually, the types of biomolecules being studied are DNA base pairs,

amino acids, or interactions between them. In order to facilitate the studies or computations, oftentimes simplified versions of biomolecules with some functional groups (such as the phosphate backbone) removed are used when studying interactions between pairs and for avoiding confounding factors due to other subunits and other types of biological interactions [17, 4]. While the decomposition of the interactions of base pairs, base stacking, and base pairs with amino acids on small scales serve as important starting points, studies of such interactions on larger and nontrivial systems would provide deeper insights into how the variety of nucleobases in nucleic acids or the domains of a protein come into play in biological systems and complexes [18].

In the present work, the HALMO-EDA scheme is used in decomposing the interstrand interactions of dsDNA into various factors and how such factors contribute to the variability of interaction energies despite having the same GC content. Linear-scaling DFT in the ONETEP scientific package and a brief overview of HALMO EDA are presented. The pipeline in which dsDNA is generated, optimized, and decomposed for chemical interactions is developed and applied in conjunction with DFT and EDA, alongside a molecular-mechanics interpretation of the energy decomposition as supporting data.

7.2 Computational Procedure with DNA Structures

To generate structures and perform classical molecular dynamics (MD) simulations of DNA fragments, we have used AmberTools, which is a distribution of programs that are independently developed as part of the Amber Project and is the free distribution that is built upon by Amber [95] for additional programs and parallelization. The version of AmberTools used here is 18, and the three programs of it used in this work are NAB (Nucleic Acid Builder), LEaP, and sander.

To study how the interaction energy is affected by sequence and sequence length, all possible four-base-pair (4bp) sequences were generated for optimization and energy determination. 2bp and 3bp sequences were not considered due to their lower sample sizes. Naive generation of DNA sequences would result in redundant structures, causing unnecessary computations on equivalent sequences. By standard convention, a

nucleic acid sequence without the strand direction being indicated is always presented in the 5′-to-3′ direction. If a sequence is presented in the 3′-to-5′ direction, the 3′ and 5′ ends must be indicated. Since each DNA sequence has a reverse complementary sequence and could be a palindrome, two generated sequences that give the same structure are reduced to one unique sequence by removing one of them. For example, `TAAT` and its reverse complement `ATTA` give the same structure and are treated as if they are the same sequence. The famous `TATA` (for a TATA box) is a palindromic sequence and, hence, has a reverse complement that happens to be the same.

Removing such redundant sequences based on sequence alone would only remove redundancies due to palindromic sequences, since each of which has a reverse complement that is the same. It would not remove non-palindromic sequences that are reverse complements of each other. Therefore, the implementation of the uniqueness of two sequences based on reverse complementarity was also taken into consideration. This resulted in 136 unique 4bp sequences. With the unique sequences generated, NAB with the BSC1 DNA force field was used for creating 136 dsDNA structures *in silico* without optimizing the resulting structure, which was done later in the pipeline.

dsDNA alone is a negatively charged system due to the phosphates in its backbone. Sodium counterions were added to the dsDNA structures in order to neutralize the negative charges using LEaP, which is an AmberTools program that creates new or modifies existing systems. However, adding the counterions to the dsDNA structures would obfuscate the association of counterions to individual strands, since LEaP considers dsDNA as a whole. Because the interaction energy of the two DNA strands coupled with counterions will be decomposed using EDA, the counterion-strand association is necessary in defining the fragments for EDA.

To keep track of which counterions are associated to which DNA strand, each dsDNA created from NAB was separated into its individual strands. The sodium counterions are then added to each strand in isolation. The counterions are tracked before recombining them back into double-stranded form. Although not needed during the optimization of the dsDNA structures, the counterion-strand associations were book-kept throughout the process. This allows the optimized structures to be used for HALMO EDA later, which requires the counterion-strand associations in order to define each

counterion-neutralized single-stranded DNA (ssDNA) as a fragment.

Depending on the length or possibly the DNA sequence itself, automatic determination by LEaP on the number of sodium counterions to add sometimes do not actually neutralize all the negative charges. However, LEaP offers an option to explicitly specify the number of counterions to add and, thus, allows a workaround to the issue. Before adding the counterions in LEaP, the negative charge of a DNA strand is determined and then negated to give the number of sodium counterions needed to neutralize all of the negative charges. The number of counterions to add are explicitly passed to LEaP so that LEaP does not determine it automatically in an occasionally erroneous way.

sander is a program in AmberTools for geometry optimization and molecular dynamics. In this work, it is used exclusively for optimizing the dsDNA structures in implicit water. For implicit water, the implicit-solvation model used [96, 97, 98] corresponds to the sander `IGB` value of `1`. Other configuration parameters for sander that are used have the values `imin = 1` (performs energy minimization), `maxcyc = 10000` (maximum number of cycles of minimization), `ncyc = 5000` (number of cycles after which to switch from steepest descent to conjugate gradient), and `ntb = 0` (no periodicity is applied). sander's `cut` parameter is dynamically determined, and the lower-bound value for `drms` is set to 1.0×10^{-6}, both of which are discussed below.

In addition to sander's optimization (which shall now be considered as the inner loop of optimization), an algorithm for the outer loop outside of AmberTools was developed that utilizes Brent's method [99] to minimize a structure's energy with a specified desired RMS (root mean square) as the lower bound and before the maximum number of steps is encountered. Furthermore, dynamically determining the cutoff distances for each dsDNA structure in an iterative fashion is implemented as part of the algorithm to avoid arbitrary cutoff distances. The nesting of the inner optimization by sander with the outer optimization yields negative interaction energies for all dsDNA structures, suggesting that the method gives more credible results than using sander alone, which would produce positive interaction energies for some of the structures.

The implementation of Brent's method used in the outer optimization is part of the Apache Commons Math, which is a Java library developed by the Apache Software Foundation. Given a user-specified lower-bound RMS and the maximum number of

steps, the outer optimization executes sander's optimization as if it is an energy function of desired RMS to be minimized. Without falling below the lower-bound RMS, the RMS passed to the energy function is the desired RMS for sander to optimized the DNA structure by. The RMS passed to the energy function is adjusted by Brent's method until the minimum of the energy function, which would be the energy of the properly optimized DNA structure, is found. The energy function is a programmatically generated function based on the DNA sequence, the implicit solvation environment, and the various configurations needed by sander.

To systematically determine cutoff distances without predefining them with arbitrarily large ones, cutoff distances are decided dynamically and iteratively as part of the outer optimization. The criterion for a cutoff distance used in this work is that it is no shorter than the largest distance between any two atoms in a supposedly optimized DNA structure. Achieving this criterion begins with an initial guess based on the distances of the atoms in an unoptimized DNA structure and is then used as the first cutoff distance for sander in the inner optimization. The largest distance in the supposedly optimized DNA is checked against the cutoff distance used. If the cutoff distance turns out to be shorter than the largest atom distance, a new cutoff distance is established by increasing from the previous cutoff distance in the outer optimization, and the inner optimization process with sander is performed again with the new cutoff distance. The procedure repeats until the criterion that the cutoff distance used for the inner optimization is no shorter than the largest atom distance in the resulting dsDNA structure is satisfied.

7.3 Variability of Energies within a GC-Content Category

All possible and unique 4bp sequences were generated, resulting in 136 sequences. These 136 sequences are constructed *in silico* as dsDNA in B form by NAB along with the addition of sodium counterions, and were then geometry optimized by sander in implicit water. Using the optimized structures, energy calculations were done by both

sander (with the BSC1 force field) and ONETEP (with PBE+D2 and B97M-V exchange-correlation functionals), with ONETEP also having performed HALMO EDA in vacuum. Descriptive statistics of the interaction energies and their HALMO-EDA components are calculated for the 4bp dsDNA structures in order to compare and contrast differences and variabilities for a fixed a GC content.

To study the significance of the ordering of the base pairs in addition to the amount of hydrogen bonding between the two strands of a dsDNA, the sequences are categorized by their GC content, which is the percentage of bases that are G or C. The possible GC contents for 4bp sequences are 0%, 25%, 50%, 75%, and 100%. Categorizing the 136 4bp sequences according to GC contents results in 10, 32, 52, 32, and 10 sequences, respectively. The purpose of GC-content categorization is to observe how base stacking and any other effects besides hydrogen bonding affect the interaction energies and their HALMO-EDA components.

For each of the dsDNA structures, ONETEP was used to calculate the interaction energy and HALMO-EDA components. Similarly, sander was used to calculate the interaction energy, electrostatics, and vdW energies in vacuum and in implicit water. Since implicit solvation with HALMO EDA is not supported in ONETEP, HALMO EDA was done in vacuum only (Tables 7.3 and 7.4). However, single-point energy calculations with implicit solvation is supported in ONETEP, and the overall interaction energies in implicit solvation were computed (Table 7.2).

Table 7.1 demonstrates the variabilities, through median absolute deviation (MAD), in the interaction energies within each GC-content group in vacuum. The spread in the interaction energies exists in both ONETEP and AmberTools. On the other hand, Table 7.2 indicates that the implicit solvation of dsDNA makes the spread in the interaction energies of the DNA strands much less pronounced. For both in vacuum and in implicit water, the median of interaction energies becomes more negative as GC content increases as expected from the estimates based on GC content alone discussed below. However, the MAD in a GC-content group can be large enough to suggest that there are sequence-dependent interactions, and the variability of interaction energies within a GC-content group deserves further dissection by EDA.

TABLE 7.1: Interaction energies for 4bp dsDNA in vacuum from ONETEP categorized by GC content. All energy values are in kcal/mol. Abbreviations: MAD, median absolute deviation; est., estimate from additive one-bp interactions

GC	PBE			B97M-V			BSC1	
Content	Median	MAD	Est.	Median	MAD	Est.	Median	MAD
0%	-58.7	5.1	-63.0	-55.6	4.3	-58.1	-45.6	5.8
25%	-80.3	12.8	-79.9	-77.1	11.5	-75.7	-64.2	11.0
50%	-97.4	8.6	-96.9	-95.4	8.6	-93.3	-81.8	9.3
75%	-115.9	8.8	-113.9	-115.4	9.3	-110.9	-105.0	12.8
100%	-134.5	10.9	-130.9	-133.7	10.6	-128.5	-120.4	14.5

TABLE 7.2: Interaction energies for 4bp dsDNA in implicit water from ONETEP categorized by GC content. All energy values are in kcal/mol. Abbreviations: MAD, median absolute deviation; est., estimate from additive one-bp interactions

GC	PBE			B97M-V			BSC1	
Content	Median	MAD	Est.	Median	MAD	Est.	Median	MAD
0%	-43.2	0.7	-35.6	-41.4	1.0	-30.2	-31.2	1.0
25%	-49.0	1.2	-39.1	-47.1	2.4	-34.0	-37.1	1.2
50%	-53.7	1.8	-42.7	-51.9	3.0	-37.8	-42.3	1.3
75%	-58.3	2.4	-46.3	-56.2	3.0	-41.6	-47.5	1.1
100%	-64.5	2.6	-49.9	-64.1	4.3	-45.4	-53.5	1.0

Interaction energies and EDA components are also estimated by adding the interaction energies of 1bp based solely on the GC content and not on the sequence. Such additive energies often underestimate the stability of a dsDNA, particularly for those in implicit water, and suggests that GC content alone often does not account for base stacking interactions. This further suggests there could be other interactions besides just hydrogen bonding that are contributing to the interaction energies being more negative than the corresponding estimates (Tables 7.1 and 7.2).

To examine which part or parts of an interaction energy that exhibit the majority of the variability, HALMO EDA was applied to the same dsDNA structures in vacuum (Tables 7.3 and 7.4 with histograms in Appendix C). DFT-D2 was not applied (i.e., 0.0) when the B97M-V functional was used, since B97M-V already accounts for dispersion interactions [42]. The largest contributor to the variability of interaction energies based on the MAD appears to be frozen density (Table 7.3). Since there is much less variability in the interaction energies for implicit water, the observation that frozen density is the most important contributor is in accordance with the fact that electrostatic forces are involved in the different environments between vacuum and implicit solvation due to the screening effects in the presence of a solvent.

TABLE 7.3: Frozen density and DFT-D2 dispersion correction for 4bp dsDNA in vacuum from HALMO EDA categorized by GC content. All energy values are in kcal/mol. Abbreviations: MAD, median absolute deviation; est., estimate from additive one-bp interactions

GC Content	Frozen Density						DFT-D2			
	PBE			B97M-V			PBE			B97M-V
	Median	MAD	Est.	Median	MAD	Est.	Median	MAD	Est.	
0%	21.2	5.4	4.8	-4.5	4.7	-8.8	-22.5	1.1	-12.7	0.0
25%	8.4	16.3	-1.3	-17.1	13.3	-16.7	-24.1	0.8	-13.4	0.0
50%	4.6	6.2	-7.4	-23.3	6.2	-24.6	-24.9	1.4	-14.0	0.0
75%	-0.3	5.2	-13.5	-33.4	6.0	-32.4	-25.9	1.2	-14.7	0.0
100%	-6.8	8.8	-19.6	-41.4	7.7	-40.3	-27.0	1.3	-15.4	0.0

TABLE 7.4: Polarization and charge transfer for 4bp dsDNA in vacuum from HALMO EDA categorized by GC content. All energy values are in kcal/mol. Abbreviations: MAD, median absolute deviation; est., estimate from additive one-bp interactions

GC Content	Polarization						Charge Transfer					
	PBE			B97M-V			PBE			B97M-V		
	Median	MAD	Est.	Median	MAD	Est.	Median	MAD	Est.	Median	MAD	Est.
0%	-17.2	0.8	-15.1	-16.1	0.8	-14.3	-39.2	0.3	-39.9	-34.5	0.3	-35.0
25%	-25.2	1.2	-21.3	-23.7	1.1	-20.4	-44.2	1.1	-44.0	-38.9	1.0	-38.6
50%	-31.4	1.9	-27.5	-29.5	2.3	-26.5	-48.4	0.9	-48.0	-42.8	0.7	-42.2
75%	-37.5	3.5	-33.8	-35.5	3.3	-32.7	-52.3	1.1	-52.0	-46.3	0.9	-45.8
100%	-42.0	3.0	-40.0	-40.4	3.0	-38.8	-55.1	1.0	-56.0	-49.0	1.0	-49.4

Since charge transfer is often considered to be a measure of covalency among fragments [13], the electron transfer portion of hydrogen bonding can be considered as part of charge transfer. By energy decomposition, the effects of hydrogen bonding can be segregated in the analysis. According to EDA results in the present work, hydrogen bonding is not the sole contributor to the strengthening of the interaction between the two DNA strands, which would offer computational support to the hypothesis that GC content alone cannot explain the thermal adaptability of single-celled and multicellular organisms [3, 21]. Furthermore, the estimates of charge transfer from additive one base pairs are very close to the corresponding value for the dsDNA structures calculated as a whole (Table 7.4). Cross base stacking may be a contributor to the increase in stability between DNA strands. Since a sufficiently long nucleic acid can fold back on itself, the overall 3D structure of a nucleic acid could further affect its stabilization. Additionally, proteins that stabilize a nucleic acid may also affect the perceived interaction energy, and some of these proteins are sequence-specific, structure-specific, or discriminate differently based on the different classes of nucleic acids.

In HALMO EDA, polarization and charge transfer are not further decomposed. Frozen density, on the other hand, is decomposed into subcomponents, allowing more fine-grained dissection of the interaction energy to better pinpoint the sources of the

TABLE 7.5: Electrostatics and Pauli repulsion for 4bp in vacuum from HALMO EDA categorized by GC content. All energy values are in kcal/mol. Abbreviations: MAD, median absolute deviation; est., estimate from additive one-bp interactions

GC Content	Electrostatics						Pauli Repulsion					
	PBE			B97M-V			PBE			B97M-V		
	Median	MAD	Est.	Median	MAD	Est.	Median	MAD	Est.	Median	MAD	Est.
0%	-71.8	5.5	-85.5	-101.3	6.1	-99.1	159.2	2.2	150.6	166.9	10.6	155.0
25%	-94.2	12.7	-102.4	-125.3	16.3	-117.2	177.0	2.6	167.8	185.0	44.4	172.7
50%	-108.7	5.8	-119.2	-138.8	8.8	-135.3	194.2	3.3	184.9	202.6	8.1	190.4
75%	-126.3	5.0	-136.1	-158.8	7.4	-153.4	212.4	3.0	202.1	223.0	5.9	208.0
100%	-144.4	8.6	-153.0	-179.5	9.5	-171.5	230.2	4.5	219.2	246.1	10.2	225.7

TABLE 7.6: Exchange and correlation for 4bp in vacuum from HALMO EDA categorized by GC content. All energy values are in kcal/mol. Abbreviations: MAD, median absolute deviation; est., estimate from additive one-bp interactions

GC Content	Exchange						Correlation					
	PBE			B97M-V			PBE			B97M-V		
	Median	MAD	Est.	Median	MAD	Est.	Median	MAD	Est.	Median	MAD	Est.
0%	-37.5	0.5	-36.7	-61.9	3.2	-56.9	-28.8	0.8	-23.6	-9.2	0.4	-7.9
25%	-41.7	0.8	-40.4	-69.1	3.8	-64.0	-31.2	0.6	-26.3	-21.1	12.4	-8.2
50%	-45.4	1.0	-44.1	-75.9	2.7	-71.1	-33.7	0.9	-28.9	-10.1	0.6	-8.5
75%	-49.3	0.9	-47.8	-85.1	1.6	-78.3	-36.5	0.7	-31.6	-10.4	0.5	-8.8
100%	-53.6	1.3	-51.6	-93.1	2.8	-85.4	-39.4	1.3	-34.2	-11.0	0.7	-9.1

variability. The descriptive statistics for 4bp dsDNA grouped by GC content (Tables 7.5 and 7.6) offer a demonstrative interpretation that electrostatics and Pauli repulsion play larger roles in the variability of the interaction energies among sequences with the same GC content compared to exchange and correlation.

To demonstrate the effects of frozen density, polarization, and charge transfer, HALMO EDA provides visualizations of the electron-density differences (EDDs) among these components. For the sequence `TA`, Figure 7.1 depicts the change in going from frozen density to polarization, whereas Figure 7.2 depicts the change in going from polarization to the variationally optimized state. For instance, the electron transfer portion of hydrogen bonding can be visualized by the charge-transfer component, illustrated by the increase in electron density between the base pairs in Figure 7.2. In fact, the majority of charge transfer comes from the electron transfer between bases from opposing strands where the hydrogen bonding occurs. Observing the EDD in going from frozen density to polarization, the change in electron densities reflects some of the pre-hydrogen bonding aspects, where the electrons on the oxygen that is partaking the hydrogen bonding have accumulated toward its companion hydrogen as if it is preparing for the electron transfer that occurs in the charge-transfer component.

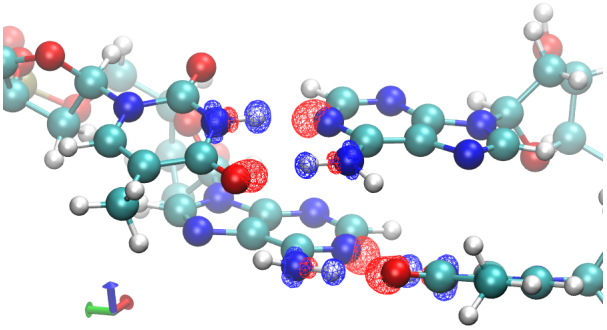

FIGURE 7.1: Change in electron densities from frozen density to polarization for the sequence TA in vacuum. Red indicates an increase in electron density; blue, decrease. Isovalue is set at $\pm 0.02\,e/Å^3$.

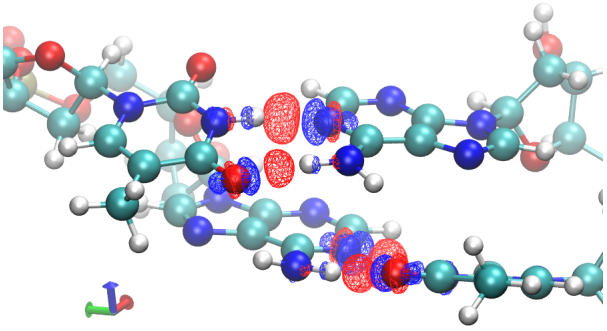

FIGURE 7.2: Change in electron densities from polarization to supermolecule with variationally optimized molecular orbitals across the supermolecule for the sequence TA in vacuum. Red indicates an increase in electron density; blue, decrease. Isovalue is set at $\pm 0.02\,e/Å^3$.

Analogous to ONETEP's HALMO EDA, AmberTools offers a molecular-mechanics version of energy decomposition. For the counterion-coupled dsDNA structures studied in this work, the two components that make up the entire interaction energy according to the BSC1 force field are electrostatics and vdW. As for HALMO EDA, the statistics calculated for these components can also be grouped by GC content (Table 7.8). For these dsDNA structures, BSC1 decomposes the interaction energy into electrostatics, vdW, and solvation energy. Solvation energy is zero in vacuum and is non-zero in implicit water. Electrostatics and vdW are the same regardless of whether a dsDNA structure is in vacuum or in implicit water.

Similar to HALMO EDA, electrostatics is also the major contributor to the variability of interaction energies according to BSC1 and substantially outweighs that of vdW. The

TABLE 7.7: Interaction and solvation energies for 4bp dsDNA using the BSC1 force field categorized by GC content. All energy values are in kcal/mol. Abbreviations: MAD, median absolute deviation

GC Content	Vacuum		Solvation		Implicit Water	
	Median	MAD	Median	MAD	Median	MAD
0%	-45.6	5.8	12.4	5.7	-31.2	1.0
25%	-64.2	11.0	27.3	11.5	-37.1	1.2
50%	-81.8	9.3	39.6	8.3	-42.3	1.3
75%	-105.0	12.8	56.8	12.5	-47.5	1.1
100%	-120.4	14.5	67.9	13.9	-53.5	1.0

decrease in the variability in the overall interaction energy between in vacuum and in implicit water is substantial, which can be seen in Table 7.7 by their MAD statistics. For any comparison in this study, caution should be taken when comparing MAD statistics between overall interaction energies and specific energy components. While an interaction energy provides an indication of the thermal stability of dsDNA as a whole from multiple contributing factors, a particular energy component's susceptibility to neighboring base interactions is a reflection of that component only.

Non-vdW and vdW energies for 4bp dsDNA in vacuum from the BSC1 force field are compared and contrasted with that of HALMO EDA (Table 7.8). Overall interaction energy is composed of non-vdW and vdW parts. In BSC1, there is a dedicated vdW component, and electrostatics makes up the remaining portion of the interaction energy as the non-vdW part. In HALMO EDA, there is no component specific to vdW, so vdW is defined either as the correlation component in HALMO EDA or as the empirical dispersion correction [100] depending on whether the exchange-correlation functional intrinsically includes dispersion interactions. This definition used in the present work was arrived by calculating 2^7 possible combinations of the components of HALMO EDA (which has six, Figure 4.2) and empirical dispersion correction, which is non-zero for PBE and zero for B97M-V. The calculated values were then compared with the vdW component of BSC1 to determine which of the combinations of HALMO-EDA components and empirical dispersion correction give values that are closer to the vdW component of BSC1 while still maintaining chemical interpretability. A definition of vdW from EDA components varies between different EDA schemes and different studies, where, for instance, an alternative definition of vdW [101, 102] includes charge transfer, which in turn is counterintuitively claimed to be related to covalency [13]. Differences in the

TABLE 7.8: Non-vdW and vdW energies for 4bp dsDNA in vacuum using HALMO EDA and BSC1 force field categorized by GC content. Interaction energy is composed of non-vdW and vdW parts. In HALMO EDA, vdW is defined either as the empirical dispersion correction (for PBE) or as the correlation component (for B97M-V). In BSC1, the non-vdW part is equivalent to the electrostatics component for the dsDNA structures in this work. All energy values are in kcal/mol. Abbreviations: MAD, median absolute deviation

GC Content	Non-VdW						VdW					
	PBE		B97M-V		BSC1		PBE		B97M-V		BSC1	
	Median	MAD	Median	MAD	Median	MAD	Median	MAD	Median	MAD	Median	MAD
0%	-36.4	6.5	-44.3	6.9	-27.6	6.0	-22.5	1.1	-9.2	0.4	-17.8	0.8
25%	-57.5	13.4	-50.4	46.0	-47.1	10.9	-24.1	0.8	-21.1	12.4	-17.4	0.9
50%	-73.8	9.0	-80.3	12.5	-65.3	8.3	-24.9	1.4	-10.1	0.6	-17.2	1.3
75%	-90.2	8.4	-95.1	18.4	-87.9	12.0	-25.9	1.2	-10.4	0.5	-16.9	1.1
100%	-106.5	11.2	-104.6	19.4	-104.4	15.4	-27.0	1.3	-11.0	0.7	-17.2	0.9

definitions of vdW contributions are attributed to the differing components in various EDA schemes and the methodologies of establishing such definitions.

By defining vdW in terms of HALMO-EDA components as done in the present work, similar variabilities (by MAD) for each GC-content group compared to BSC1 are exhibited in PBE and B97M-V, with the exception of the 25% GC-content group for B97M-V that is also apparent in the overall interaction energy in vacuum. For PBE, the vdW contribution to the interaction energy is significantly overestimated in a consistent manner compared to both BSC1 and B97M-V. For B97M-V not in the 25% GC-content group, the vdW contribution is underestimated compared to BSC1, roughly by the same magnitude in the opposite direction relative to PBE. To provide a comparison with an SAPT-based approach, we also give vdW components between the two fragments for each dsDNA structure from vdW2017 [94], an SAPT-based force field for vdW contributions, in Appendix C. These further demonstrate the non-uniqueness in the partitioning of energy components among EDA schemes.

The much greater variability in vdW contributions for the 25% GC-content group using the B97M-V functional lends itself to future studies in determining whether the variability is an artifact of the way this exchange-correlation functional operates or is due to actual sequence-dependent interactions. If the latter, such interactions are apparently more pronounced when the GC content is 25% for 4bp and could serve as a useful category for future studies of interactions that depend on neighboring base pairs.

7.4 Conclusions

We have applied energy decomposition analysis (EDA) methods to dissect the interactions within double-stranded DNA (dsDNA) to examine how much sequence-dependent interactions affect the interaction energies of dsDNA molecules. For this work, we have analyzed all 136 combinations of four-base-pair (4bp) sequences, which we have categorized based on their GC content.

Hybrid Absolutely Localized Molecular Orbitals (HALMO) EDA has shown to be a useful tool in conjunction with molecular mechanics in decomposing the interaction energies into components for comparisons and analysis. It has been demonstrated by this work and the works of other researchers that GC content is an important property of DNA in the context of its stability. Despite its importance, it is not the sole factor in determining the stability of nucleic acids, since substantial variabilities can exist for nucleic acids with the same GC content. This suggests that the hydrogen bonding between two bases should not be considered as the only or even the most important factor in the interactions between two complementary DNA strands.

This work has provided a new paradigm and tool for the study and analysis of nucleic acid interactions using EDA within large-scale quantum chemistry calculations. Future work can involve more in-depth study of intramolecular interactions that exist within nucleic acids and also the interaction of nucleic acids with other entities, such as proteins and drug molecules.

Chapter 8

EDA Method for Metallic Systems

This adapted chapter was published in the journal Physical Chemistry Chemical Physics (PCCP) of the Royal Society of Chemistry (see Chen and Skylaris [2]).

8.1 EDA with Ensemble DFT (EDFT)

Density-functional theory (DFT) aims to estimate the total energy of a system. Complementing DFT or wave-function methods, the main objectives of energy decomposition analysis (EDA) is to partition the interaction energy of a supermolecule into their chemical origins in a similar vein to mono- and diatomic centers [103, 104] but for fragments containing an arbitrary number of atoms instead. Examples of the components of an EDA scheme often include electrostatics, exchange-correlation contributions, polarization, and any other relevant chemical phenomena. Hence, EDA is an analytical tool that partitions the interaction energy into chemically interpretable components.

Whenever the interaction energy is concerned, basis set superposition error (BSSE) must be taken into account. There are many approaches to addressing BSSE [75], but a common approach taken by some EDA schemes is the self-consistent field for molecular interaction (SCF MI), which optimizes the molecular orbitals in the presence of all fragments without BSSE [80]. Essentially, SCF MI expands the molecular orbitals of each fragment in the basis functions of the fragment only, which minimizes the amount of charge transfer that occurs among the fragments [81]. As such, SCF MI can also be used for computing the energy arising from charge transfer, which is evaluated by

taking the difference between applying and not applying SCF MI. In the context of EDA, charge transfer is a useful and interpretable component that indicates the amount of charge that is transferred from one fragment to another [13]. While different approaches to SCF MI have been proposed, the method of localized molecular orbitals (LMO) SCF MI [79] is chosen here for its amenability to fractional occupancies inherent in species with sufficiently small band gaps at finite electronic temperatures.

In the family of finite-temperature DFT methods, various approaches have been employed to study systems under finite electronic temperatures [105, 106], at excited states [107, 108], or open systems that have fractional electron numbers [109]. For the validation of metallic systems presented in this work, the finite-temperature DFT algorithm of ensemble DFT (EDFT) [22, 23] in the ONETEP software package [9, 8] is used to optimize a set of sample metallic systems with sufficiently small or no band gaps that produces fractional occupancies at specific electronic temperatures. Without EDA, metallic systems can be fragmented into subsystems in order to obtain the interaction energy, but nothing beyond such a coarse-grained energy value would be available. EDA methods serve to decompose the interaction energy but are normally developed for pure states where the occupancies are integral. EDA schemes, particularly those that require SCF MI as in ALMO/HALMO EDA, pose difficulties in decomposing the interaction energy of a metallic system due to the fractional occupancies that are part of the optimization process in EDFT. Hence, fractional occupancies must also be incorporated in the SCF-MI optimization process of the fragmented system.

Although EDA is normally developed and applied to non-conducting species at pure states, developing EDA for species that have a conduction band or have fragments that interact with each other through the conduction of charge necessitates the incorporation of EDA in EDFT, such that the interactions (which could possibly involve covalent bonding) can be dissected into contributing factors as EDA components. Other than EDFT in ONETEP [23], the methods presented in this work are applicable to wave-function-based approaches (e.g., Hartree-Fock methods) as well. Separate and independent from ONETEP, the implementation of HALMO EDA makes no distinction between DFT and wave-function methods. EDA and EDFT are first given an overview. The problem of extending SCF MI to fractional occupancies in EDA for each fragment

with weighted orthogonalization (WO) [73] is then discussed. WO is essential in orthogonalizing the molecular orbitals based on their differing fractional occupancies for the projection operators needed by SCF MI. Finally, motivation of and results from EDA with EDFT applied to sample metallic systems with small band gaps are presented.

8.1.1 Theory of EDFT

Ensemble DFT (EDFT) as in ONETEP treats a supermolecule as a whole without the concept of fragmentation as in EDA. EDFT involves occupancies that are fractional, since a species is no longer evaluated at a pure state and, hence, the density operator is no longer idempotent. The lack of idempotency complicates SCF MI due to the fact that SCF-MI methods were originally developed under the pervasive assumption of a pure state. Therefore, SCF MI must be extended to include fractional occupancies. Before considering EDFT with fragmentation and under the constraints of SCF MI, an overview of EDFT is given first.

A system of interacting electrons [23] satisfies the Kohn-Sham (KS) equation,

$$\hat{H}\,|\psi_i\rangle = |\psi_i\rangle\,\varepsilon_i \tag{8.1.1}$$

where $\{\psi_i\}$ are molecular orbitals, $\{\varepsilon_i\}$ are orbital energies as eigenvalues, and $\hat{H}$ is the Hamiltonian as

$$\hat{H} = \hat{T} + \hat{V}_{\text{ext}} + \hat{V}_{\text{H}}\,[n] + \hat{V}_{\text{xc}}\,[n] \tag{8.1.2}$$

Here, $\hat{T}$ is the kinetic energy operator, $\hat{V}_{\text{ext}}$ is the potential operator due to the field of the nucleus, $\hat{V}_{\text{H}}$ is the Hartree potential operator, $\hat{V}_{\text{xc}}$ is the exchange-correlation potential operator, and

$$n\,(\mathbf{r}) = \sum_i f_i \psi_i^*\,(\mathbf{r})\,\psi_i\,(\mathbf{r}) \tag{8.1.3}$$

is the electron density with $\{f_i\}$ as the occupancies of the molecular orbitals.

The occupancy, f, of a molecular orbital is determined from the Fermi-Dirac distribution as a function of its orbital energy, ε:

$$f(\varepsilon;\mu) = \frac{1}{e^{(\varepsilon-\mu)/(k_B T)} + 1} \tag{8.1.4}$$

where k_B is the Boltzmann constant, T is a non-zero electronic temperature, and μ is the Fermi level as a parameter. Also called the chemical potential, a Fermi level is determined algorithmically (as in ONETEP [23]) from a known number of electrons and a given set of orbital energies. For a fixed set of orbital energies at a specified electronic temperature, the search begins with an initial guess of the Fermi level and calculates the occupancies of the molecular orbitals using Equation (8.1.4). If the sum of the occupancies differs from the expected number of electrons, the search adjusts the Fermi level in the appropriate direction and recalculates the occupancies. The algorithm repeats and adjusts the Fermi level until the occupancies computed from the Fermi-Dirac distribution sum to the number of electrons, thereby determining the Fermi level of the species.

Since the Fermi-Dirac distribution assumes negligible interactions among electrons, the EDFT implementation in ONETEP as of this writing is not applicable to strongly correlated systems unless it is modified to use a generalization of Fermi-Dirac distribution [110]. Coulomb holes for electron pairs that are positionally close to each other and have opposite spins are the primary reason for electron correlation being excluded in the Hartree-Fock wave function [37]. In a correlated system, Coulomb holes are no longer negligible, and the movement of one electron strongly depends on the positions and movements of other electrons due to Coulomb interaction [111]. The emergent behavior from such complex interactions among electrons can induce fractional occupancies that do not obey the Fermi-Dirac distribution, and a generalization of the distribution would have to be used.

The entropy, $\mathcal{S}$, depends on the occupancies according to

$$\mathcal{S}\left(\{f_i\}\right) = -k_B \sum_i \left(f_i \ln f_i + (1-f_i)\ln\left(1-f_i\right)\right) \tag{8.1.5}$$

The Helmholtz free energy, A, relates the KS energy and the entropy via the electronic temperature, T, by

$$\begin{aligned} A\left[\{\psi_i\},\{f_i\};T\right] = & \sum_i f_i \left\langle \psi_i \middle| \hat{T} + \hat{V}_{\text{ext}} \middle| \psi_i \right\rangle \\ & + E_{\text{H}}[n] + E_{\text{xc}}[n] - T\mathcal{S}\left(\{f_i\}\right) \end{aligned} \tag{8.1.6}$$

where E_{H} is the Hartree energy functional, and E_{xc} is the exchange-correlation energy functional. Equation (8.1.6) can be expressed in terms of NGWFs, $\{\phi_k\}$, and expansion coefficients, $\left\{M^k{}_i\right\}$, as

$$\begin{aligned} A\left[\left\{M^k{}_i\right\},\{\phi_k\},\{f_i\};T\right] = & \sum_{k,i} f_i \left(\mathbf{M}^{\dagger}\right)_i{}^k \left\langle \phi_k \middle| \hat{T} + \hat{V}_{\text{ext}} \middle| \phi_k \right\rangle M^k{}_i \\ & + E_{\text{H}}[n] + E_{\text{xc}}[n] - T\mathcal{S}\left(\{f_i\}\right) \end{aligned} \tag{8.1.7}$$

In minimizing the energy, the process of optimizing the Hamiltonian is performed by a line-search algorithm described in Appendix D.

8.1.1.1 Incorporating Fractional Occupancies

Many EDA schemes were developed for a pure state. By assuming a pure state, an EDA scheme and its implementation can simplify what otherwise could be a complicated scheme. HALMO EDA removes this assumption by incorporating fractional occupancies as part of the optimization process, with a pure state being a special case. In contrast, recent developments of ALMO EDA for excited systems involve adapting its EDA scheme in a way that has its EDA components tailored for excited systems [112]. Although excited systems are not studied in this work, HALMO EDA addresses the similar difficulties of decomposing the interaction energy of a system not at a pure state by allowing occupancies to be fractional. The result of this generalization is that HALMO EDA with EDFT can be applied to systems in ensemble states at finite electronic temperatures without modifying the EDA scheme itself.

For incorporating ensemble-state calculations into EDA, the fractional occupancies that are part of the density kernel are included in the implementation of SCF MI. The

problem of performing ensemble-state calculations as part of an EDA scheme then becomes a problem of determining the fractional occupancies during the energy decomposition. Determining the fractional occupancies themselves is performed by the existing implementation of EDFT in ONETEP [23] using the Fermi-Dirac distribution, and the HALMO-EDA scheme itself remains unmodified with the same components.

The density kernel varies depending on the quantum state of the system. Specifically, the molecular orbitals differ via the expansion coefficients, and the molecular orbitals would have another set of orbital energies. In turn, occupancies depend on the orbital energies [32, 31, 23]. Therefore, the density kernel must be reconstructed along with a changing set of occupancies throughout an EDA calculation. According to the Fermi-Dirac distribution for fragmented systems, the occupancy, f_{Ji}, of a molecular orbital localized to Fragment J as a function of its orbital energy, ε_{Ji}, is

$$f_{Ji} = f(\varepsilon_{Ji}; \mu_J) = \frac{1}{e^{\left(\varepsilon_{Ji} - \mu_J\right)/(k_B T)} + 1} \tag{8.1.8}$$

where μ_J is the Fermi level of Fragment J as the parameter. The number of electrons in each fragment is known from the optimization of the fragments in isolation. For each fragment, its own Fermi level is determined, followed by calculating the desired occupancies. By evaluating the Fermi-Dirac distribution for each fragment, the SCF-MI constraint of disallowing charge transfer to take place is satisfied, and the occupancies of the molecular orbitals in a fragment are calculated without the orbital energies from other fragments. Despite the different Fermi levels across fragments, charge flow does not occur among fragments, since SCF MI restricts charge transfer. The process of incorporating occupancies from EDFT in SCF MI is diagrammed in Figure 8.1.

SCF MI with WO bears some similarities and important differences to the related method of molecular-orbital localization with intrinsic fragment orbitals (IFOs) [113, 114]. Both approaches utilize orbitals that are expanded in the basis functions localized on respective fragments and perform 2-by-2 rotations to maximize an objective function. However, an SCF-MI method formulates [79, 81] a solution to the expansion coefficients of the fragment-localized orbitals and the needed orbital energies by affecting the eigenvalue spectrum [85], whereas the approach of IFOs does not and simply specifies the general form of the resulting orbitals. Another distinguishing nature of

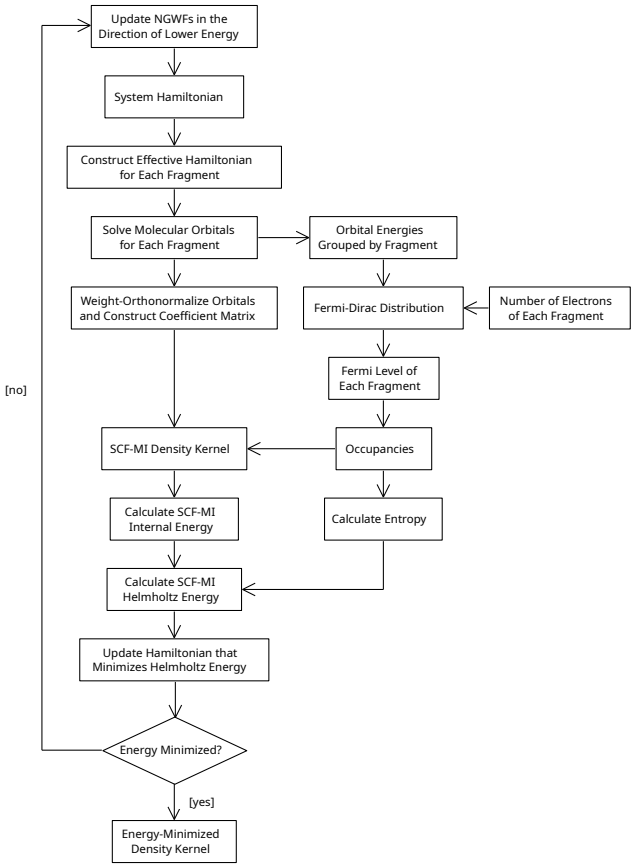

FIGURE 8.1: LMO SCF MI with occupancies from EDFT. EDFT uses the Fermi-Dirac distribution to calculate the occupancies of the molecular orbitals. Once calculated, the occupancies are incorporated into the density kernel. From the density kernel and occupancies, the internal and Helmholtz energies are evaluated. The Helmholtz energy is used in the line search of EDFT to find the energy minimum.

IFOs is that the projector matrices implicitly assume symmetric orthogonalization (SO) of some reference fragment orbitals based on how the overlap matrices are used in their definitions, while LMO SCF MI has its projection operators naturally arising from the derivation of energy minimization [79]. Finally, the objective function being maximized is different in WO compared to the construction of localized molecular orbitals (LMOs) from IFOs. Specifically, the LMOs formed from IFOs have the number of electrons in each fragment raised to the fourth power maximized [114], but WO has the more general aim of maximizing the weighted overlap sum defined by (5.2.2). Hence, WO and SCF MI remain more applicable than IFOs by allowing orbital occupancies to serve as orthogonalization weights in the construction of a projection operator.

8.2 EDA of Sample Metallic Systems

HALMO EDA with EDFT was performed for Pt_{13}-CO(atop), Pt_{55}-CO(atop), anatase-Pt_{13}-CO(atop), Pt_{210}-phenol, and Li_{12}-graphite. These systems have sufficiently small band gaps that they exhibit fractional occupancies at finite electronic temperatures and, therefore, serve as test systems for HALMO EDA with EDFT. All systems were analyzed at the electronic temperature of 0.1 eV (1160 K) except Pt_{210}-phenol, which was analyzed at the electronic temperature of 0.086 eV (1000 K). Furthermore, in relevance to the interactions that occur in heterogeneous catalysis, fragmentation of each system for EDA occurs at the bonds between the adsorbate and the catalyst.

The frozen-density component of HALMO EDA contains electrostatics, exchange, Pauli repulsion, and correlation as its subcomponents. For all species in this study, the frozen-density components exhibit similar characteristics. Energy values of electrostatics, exchange, and correlation are negative, indicating that the interactions from these factors are favorable. Energy values of Pauli repulsion, however, are positive and large, which stems from the unfavorable exclusion repulsions caused by overlapping molecular orbitals.

For Pt_{13}-CO(atop), Pt_{55}-CO(atop), and anatase-Pt_{13}-CO(atop), a carbon-monoxide molecule is bonded to the platinum portion of the system. In anatase-Pt_{13}-CO(atop), the platinum nanoparticle is supported by titanium dioxide (TiO_2, also called titania) [115]. These systems are depicted in Figure 8.2. HALMO EDA was performed for each of the species fragmented at the bond between carbon monoxide and the platinum nanoparticle (Table 8.1) except anatase-Pt_{13}-CO(atop), which has an additional fragmentation scheme between the platinum nanoparticle and the anatase support (Table 8.2). RPBE exchange-correlation functional was used for its improved adsorption energies compared to those of PBE [116]. Electronic temperature of 0.1 eV was used as in the original studies by Ellaby et al. [115], with the possible relation to the stability of anatase. HALMO-EDA results for these systems demonstrate some trends among them (Table 8.1). Unlike the Helmholtz interaction energy, the internal interaction energy does not contain the entropic term due to electronic temperature. As such, any fractional occupancies result in the two types of interaction energies being different. Indeed, the three platinum species are expected to have fractional occupancies at the

specified finite electronic temperature and have unequal internal and Helmholtz interaction energies. From SCF MI, the large charge-transfer energies suggest that the covalency between the carbon monoxide and the platinum is substantial [13], which is to be expected for heterogeneous catalysis in general.

To get a sense of the charge distribution in relation to the charge-transfer energy, Mulliken population analysis was also performed for each of the platinum-nanoparticle systems in the last part of their respective calculations where charge transfer has occurred (Table 8.3). Charges of the atoms in each subspecies were summed to give the charge of the subspecies. For the HALMO polarized state from SCF MI, the Mulliken charge of each fragment is zero (data not shown), which is in accordance with a constraint of SCF MI where the delocalization of electrons among fragments is disallowed. Pt_{13}-CO(atop) has a charge-transfer energy of $-92.3\,\mathrm{kcal/mol}$, and Pt_{55}-CO has a less negative value of $-90.9\,\mathrm{kcal/mol}$. This correlates with the Mulliken charge of carbon monoxide not being as negative in Pt_{55}-CO(atop) (-0.126) as compared to Pt_{13}-CO(atop) (-0.130). Anatase-Pt_{13}-CO(atop), however, does not agree with the trend. A possible explanation is that some of the charge has transferred from anatase to carbon monoxide and made the covalent bonding between carbon monoxide and the platinum nanoparticle less stable. If instead the fragmentation is between the platinum nanoparticle and anatase (Table 8.2), the charge-transfer energy is much more negative than any of the species in Table 8.1, and the Mulliken charge on anatase agrees with the charge-transfer energy being more negative.

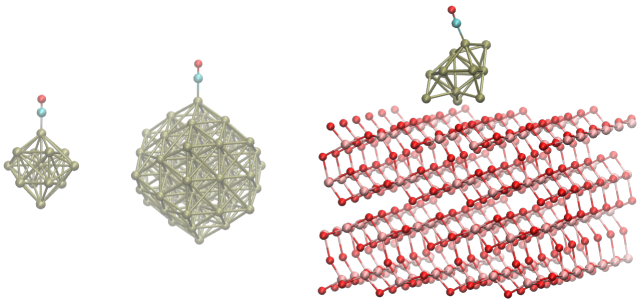

FIGURE 8.2: Pt_{13}-CO(atop), Pt_{55}-CO(atop), and anatase-Pt_{13}-CO(atop). Red atom is oxygen, light blue atom is carbon, gold atom is platinum, and pink atom is titanium.

Visualizing the major EDA components can be done with electron-density differences (EDD) [18]. Figure 8.3 illustrates the polarization and charge-transfer components for Pt_{13}-CO(atop). Polarization can be thought of as the change in quantum state

TABLE 8.1: HALMO EDA with EDFT of Pt_{13}-CO(atop), Pt_{55}-CO(atop), and anatase-Pt_{13}-CO(atop) using the RPBE exchange-correlation functional at electronic temperature of 0.1 eV. Fragmentation is indicated by the bracketing. All energy values are in kcal/mol.

EDA Component	[Pt_{13}][CO(Atop)]	[Pt_{55}][CO(Atop)]	[Anatase-Pt_{13}][CO(Atop)]
Electrostatics	−36.1	−38.3	−39.7
Exchange	−56.3	−53.9	−56.6
Pauli repulsion	214.2	216.9	220.1
Correlation	−22.1	−22.1	−22.8
Polarization	−78.2	−68.4	−45.6
Charge transfer	−92.3	−90.9	−87.8
Internal interaction energy	−70.9	−56.7	−32.5
Helmholtz interaction energy	−67.5	−54.0	−30.5

TABLE 8.2: HALMO EDA with EDFT of anatase-Pt_{13}-CO(atop) using the RPBE exchange-correlation functional at electronic temperature of 0.1 eV. Fragmentation is between the platinum nanoparticle and the anatase support, indicated by the bracketing. All energy values are in kcal/mol.

EDA Component	[Anatase][Pt_{13}-CO(Atop)]
Electrostatics	−130.0
Exchange	−87.2
Pauli repulsion	418.2
Correlation	−61.0
Polarization	−88.6
Charge transfer	−145.2
Internal interaction energy	−93.9
Helmholtz interaction energy	−92.4

TABLE 8.3: Mulliken population analyses of Pt_{13}-CO(atop), Pt_{55}-CO(atop), and anatase-Pt_{13}-CO(atop) for the optimized supermolecule state after charge transfer has occurred.

Subspecies	Pt_{13}-CO(Atop)	Pt_{55}-CO(Atop)	Anatase-Pt_{13}-CO(Atop)
Carbon Monoxide	−0.130	−0.126	−0.137
Platinum Nanoparticle	0.130	0.126	0.558
Anatase	N/A	N/A	−0.421

where the fragments in the supermolecule are preparing for electron transfer among each other. This can be visualized as an increase in the electron density close to the nucleophilic carbon atom on the side facing the electrophilic platinum atom. During charge transfer, the region between the carbon atom and the platinum atom experiences an increase in electron density as the two atoms form a covalent bond. A corresponding decrease in electron density is observed at the face of the carbon atom, indicating that the electrons migrated from the carbon atom toward the bonding region with the

platinum atom. This suggests that the energy decomposition of Pt_{13}-CO(atop) is qualitatively reasonable with the covalency between the Pt nanoparticle and carbon monoxide.

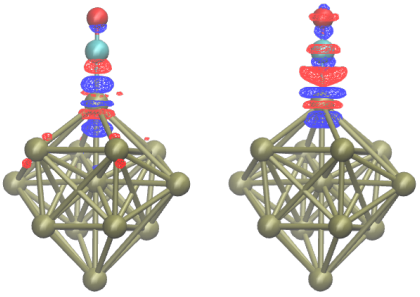

FIGURE 8.3: Difference in electron densities for polarization (left) and for charge transfer (right) of Pt_{13}-CO(atop). Red atom is oxygen, light blue atom is carbon, and gold atom is platinum. Red wireframe indicates an increase in electron density; blue wireframe, decrease. Isovalue is set at $\pm 0.05\,e\,Å^{-3}$.

Pt_{210}-phenol is another heterogeneous catalysis system (Figure 8.4) that was tested with HALMO EDA (Table 8.4). optB88-vdW exchange-correlation functional was used for its inclusion of van der Waal contributions [117], which are important in accurately assessing the binding strengths of aromatic adsorbates [118, 119]. Electronic temperature of 0.086 eV was used at the suggestion of Bramley et al. [119] and happens to place the Fermi level in proximity to the energy of the highest occupied state in the supermolecule at absolute zero temperature. However, there is nothing that argues against using a different electronic temperature, such as a temperature as high as 0.2 eV used in the studies by Chaudhary et al. [118]. Fragmentation is along the binding between Pt_{210} (the slab) and phenol (the adsorbate). Similar to the other systems tested, Pt_{210}-phenol exhibits large negative charge-transfer energy (-238.1 kcal/mol) according to HALMO EDA, indicating that there is significant transfer of electrons and, hence, covalency between the two fragments. The relatively small difference (1.3 kcal/mol) between the internal and Helmholtz interaction energies implies that the interaction due to entropic effects from electronic temperature is not very substantial. This in turn indicates that the interaction between Pt_{210} and phenol stems significantly from their binding. From this HALMO EDA, the improvement of a catalysis system similar to Pt_{210}-phenol would benefit from optimizing the interaction between the slab and the adsorbate such that the interaction is more favorable for catalysis.

TABLE 8.4: HALMO EDA with EDFT of Pt_{210}-phenol using the optB88-vdW exchange-correlation functional at electronic temperature of 0.086 eV. Fragmentation is indicated by the bracketing. All energy values are in kcal/mol.

EDA Component	[Pt_{210}][Phenol]
Electrostatics	−139.3
Exchange	−307.7
Pauli repulsion	756.6
Correlation	−39.0
Polarization	−147.8
Charge transfer	−238.1
Internal interaction energy	−115.3
Helmholtz interaction energy	−114.0

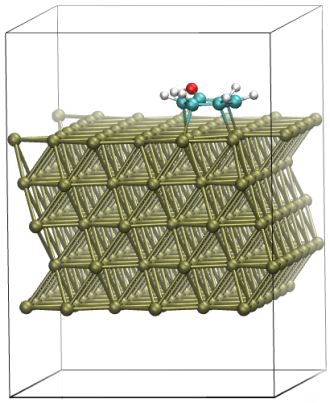

FIGURE 8.4: Pt_{210}-phenol with its periodic unit cell.

As a final example, HALMO EDA with EDFT of lithium nucleation at graphite models of battery electrodes was performed. Lithium metal plating is an undesired side effect in lithium-ion cells and decreases the lifetime of the battery [120]. Plating is caused by the nucleation of lithium ions on the graphite. Increasing the nucleation barrier would be desirable in the design of lithium-ion cells so that a battery's lifetime can be improved. Since lithium nucleation can be viewed as an interaction between lithium ions and graphite, EDA is suitable for examining the factors that contribute to such interaction and could offer some insight on which factors are more prevalent compared to others, otherwise the overall interaction energy would be too coarse-grained. Furthermore, competing designs of lithium-ion cells can also be compared using EDA as part of a methodology that aims to increase the nucleation barrier where some of the EDA components could have an effect on the overall lifetime.

Table 8.5 lists the HALMO-EDA components of graphite and a cluster of 12 lithium atoms (Figure 8.5) in vacuum, with graphite as one fragment and the lithium cluster as

TABLE 8.5: HALMO EDA with EDFT of Li_{12}-graphite in vacuum using the PBE exchange-correlation functional at electronic temperature of 0.1 eV. Fragmentation is indicated by the bracketing. All energy values are in kcal/mol.

EDA Component	[Li_{12}][Graphite]
Electrostatics	−298.9
Exchange	−288.4
Pauli repulsion	951.4
Correlation	−59.5
Polarization	−170.1
Charge transfer	−308.8
DFT-D2	−56.2
Internal interaction energy	−230.6
Helmholtz interaction energy	−216.9

the other. Starting from a nucleation energy of 0 eV for one lithium atom, the nucleation energy increases with increasing number of lithium atoms until the critical point of 12 lithium atoms is reached; the nucleation energy then decreases as the number of lithium atoms continues to increase beyond 12, with negative nucleation energies for clusters of more than 36 lithium atoms [120]. Similar to the other species in this work, the Li_{12}-graphite system exhibits large negative charge-transfer energy (−308.8 kcal/mol) from the interaction between the graphite and lithium cluster. The possibility of making the charge-transfer component less negative could suggest a candidate design that can mitigate the lithium-nucleation effect, which in turn cannot be gleaned from the interaction energy alone. Effects of the finite electronic temperature (0.1 eV) are also exhibited in the difference of 13.7 kcal/mol between internal (−230.6 kcal/mol) and Helmholtz (−216.9 kcal/mol) interaction energies. Electronic temperature lessens the interaction between the lithium ions and graphite due to entropic effects and can be varied in EDFT calculations to study the effects of temperature on the nucleation barrier [120].

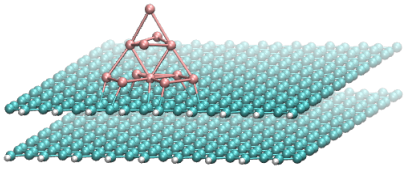

FIGURE 8.5: Li_{12}-graphite.

8.3 Conclusions

Energy decomposition analysis (EDA) has been extended to metallic systems using an implementation alongside a patched version of ONETEP that can dissect the interaction energy of a species in an ensemble state. EDA and self-consistent field for molecular interaction (SCF MI) methods have usually been developed and applied to systems in pure states. In this work, EDA and SCF MI were expanded to species that are studied with ensemble DFT (EDFT).

SCF MI was combined with EDFT by removing the assumptions of a pure state and incorporating fractional occupancies into the implementation of SCF MI. Fractional occupancies determined by EDFT are normally for the supermolecule as a whole using the Fermi-Dirac distribution. However, in order for SCF MI to accommodate the occupancies into its process, the evaluation of Fermi-Dirac distribution was restricted to individual fragments, resulting in each fragment having a different Fermi level.

Throughout the line search of EDFT in finding the minimum energy, the constraints of SCF MI were imposed such that the molecular orbitals and the associated orbital energies are determined from the effective Hamiltonian of LMO SCF MI [79]. The effective Hamiltonian of LMO SCF MI contains projection operators that require weighted orthogonalization (WO) to be constructed due to the fractional occupancies from an ensemble state. Constructing the projection operators was adapted to orthogonalizing the molecular orbitals with fractional occupancies as orthogonalization weights. Using WO, the construction of such SCF-MI projection operators and the level of occupancy of each molecular orbital are therefore made consistent in the formulation and implementation of SCF MI.

The adaptations of EDA and SCF MI to metallic systems were validated using examples in catalysis and batteries, such as carbon-monoxide-bound platinum nanoparticle systems (in vacuum and supported on titania), a platinum slab with phenol adsorbed, and graphite with a lithium cluster, all of which have sufficiently small band gaps. Across these sample metallic systems, HALMO EDA has provided reasonable decompositions of interactions energies and revealed some trends from SCF MI that correlate with charge distributions and chemical intuition.

This work has provided a new paradigm and tool for the study and analysis of metallic systems using a combination of EDA and EDFT within large-scale quantum chemistry calculations. HALMO EDA has shown to be a useful tool in decomposing the interaction energy into components for comparisons and analysis of systems in ensemble states that require EDFT. It has been demonstrated by this work that EDA with SCF MI can be extended and applied to metallic systems at finite electronic temperatures. With such advances, EDA and SCF MI are no longer restricted to species in pure states. Future work can involve more in-depth study of the nature of interactions in some technologically important systems, such as conductors, semiconductors, heterogeneous catalysts, and lithium-ion batteries.

Chapter 9

Conclusions

EDA (cf. §4) serves as an invaluable method for decomposing the interaction energy into its chemically relevant constituents. Biomolecular systems and metallic systems are two different practical motivations for understanding the factors that contribute to the interaction energy. By decomposing the interaction energy of a set of fragments, the factors that contribute to the overall interaction energy can be elucidated. With insights into these factors, the nature of the interactions could be better interpreted, and for metallic systems being manipulated, potential optimizations could be more readily examined in better chemical contexts.

EDA was extended and applied to biomolecular and metallic systems in order to further develop EDA as a method of decomposing the interaction energy into its constituents. For the applications of EDA to biomolecular systems, dsDNA was examined for correlations between GC content and EDA components (cf. §7. For the first extension of EDA to metallic systems, various species containing platinum nanoparticles were used in example calculations to validate the implementations of HALMO EDA and LMO SCF MI for ensemble states (cf. §8).

EDA has shown to be a useful tool in conjunction with molecular mechanics in decomposing the interaction energies of dsDNA into components for comparisons and analysis. It has been demonstrated by this work and the works of other researchers that GC content is an important property of DNA in the context of its stability. Despite its importance, it is not the sole factor in determining the stability of nucleic acids, since

substantial variabilities can exist for nucleic acids with the same GC content. This suggests that the hydrogen bonding between two bases should not be considered as the only or even the most important factor in the interactions between two complementary DNA strands. With a relatively large number of dsDNA structures that were analyzed, the present work also demonstrated data management issues that had to be overcome using automated approaches.

The SCF-MI approach (cf. §6) was made more mathematically transparent and then extended to ensemble states. Beyond insulating systems, LMO SCF MI (cf. §6.2) has been adapted to incorporate fractional occupancies as part of its formulation and implementation. With fractional occupancies taken into account, EDA and LMO SCF MI have been successfully applied to metallic systems with small band gaps at finite electronic temperatures. LMO SCF MI was combined with EDFT by removing the assumptions of a pure state. Fractional occupancies determined by EDFT are normally for the supermolecule as a whole using the Fermi-Dirac distribution. However, in order for SCF MI to accommodate the occupancies into its process, the evaluation of Fermi-Dirac distribution was restricted to individual fragments, resulting in each fragment having a different Fermi level.

Complicating the effort to extend LMO SCF MI to metallic systems, LMO SCF MI requires the use of projection operators that in turn depends on orthogonalization of the molecular orbitals. However, since molecular orbitals are not equally occupied, orthogonalization of the molecular orbitals should also not be uniform. WO (cf. §5.2) is orthogonalization with weights that account for different amounts of overlap with the original set of orbitals. By using fractional occupancies as weights, WO is able to appropriately orthogonalize the molecular orbitals for the projection operators in LMO SCF MI in the context of metallic systems and not just for insulating systems.

In addition to systems in pure states, this work has provided a new paradigm and tool for the study and analysis of metallic systems as well as insulating systems using the combination of EDA and EDFT within large-scale quantum chemistry calculations. HALMO EDA has shown to be a useful tool in decomposing the interaction energy into components for comparison and analysis of systems in pure and ensemble states. It has been demonstrated by this work that EDA with SCF MI can be extended and applied to

metallic systems at finite electronic temperatures. With such advances, EDA and SCF MI are no longer restricted to species in pure states, which has become a special case in the extended version of HALMO EDA.

Chapter 10

Future Work

10.1 LP SCF MI and Other EDA Schemes

Currently, ONETEP only supports LMO SCF MI (cf. §6.2) as originally implemented by Phipps et al. [19]. LMO SCF MI is both conceptually and mathematically much more unintuitive than LP SCF MI. This resulted in a correspondingly complicated implementation of LMO SCF MI in ONETEP. With regards to performing SCF MI for the polarization component of HALMO EDA, convergence can indeed be an issue as reported by Stoll et al. [79]. For such convergence issues, the usual workaround is to simply lower the threshold for convergence. Without an alternative SCF MI method, lowering the convergence threshold is currently the only option.

By implementing LP SCF MI, additional SCF MI methods would be available for determining the polarization component of HALMO EDA. Furthermore, benchmarking among the various SCF MI methods would be useful in comparing convergence, computational costs, and the effects on the charge-transfer component that a particular SCF MI method has. LP SCF MI could also be extended, both in theory and in implementation, to the study of metallic systems.

EDA is a family of methods that decompose the interaction energy into components. These decompositions are not unique, which therefore gives rise to various EDA schemes. Currently, only HALMO EDA and CLMO EDA are implemented such that they can be utilized by ONETEP. If other EDA schemes could also be implemented for

ONETEP, the variety and usefulness of EDA would be broadened, and with linear scaling, many large systems would benefit from the various decompositions of the same interaction energy. With fractional occupancies incorporated in the implementations of HALMO and CLMO EDA, other EDA schemes may be considered for extensions to ensemble states.

10.2 Intramolecular Non-Covalent Interactions

In order to support ONETEP EDA for dealing with intramolecular non-covalent interactions, an EDA implementation must be able to employ spin-polarized calculations. Intramolecular interactions are essential in many biological processes and are often studied in structural biology, where conformational changes of biomolecules are examined at molecular and biochemical levels. Such conformational changes usually involve non-covalent interactions as well as hydrogen bonding within the same molecule. Intramolecular interactions also exist in systems where they serve as a stabilization factor. For nucleic acids, GC content generally shows little to poor correlation with the stability of nucleic acids, although it appears to correlate more for RNA than genomic DNA [3]. Such biological systems would benefit from EDA with a fragmentation scheme that elucidates intramolecular non-covalent interactions [121].

To study intramolecular non-covalent interactions, an implementation EDA must be able to carry out calculations on a fragment that is spin polarized. Fragmentation of a supermolecule to study intramolecular interactions involves single-bond homolysis breaks [121]. The bond breakage is necessary, since EDA schemes are normally for intermolecular interactions. By severing a molecule into more than one fragment for EDA, EDA can treat the interactions among fragments as if they are intermolecular without special modifications to the EDA implementation, even though the fragments originally belong to the same molecule.

In ONETEP, spin polarization involves two density kernels, one for each spin function (cf. (3.4.4b)). However, the implementation of HALMO EDA in ONETEP originally began with the assumption that all fragments are not spin polarized and then

attempts were made at correcting that assumption when at least one fragment is encountered to be spin polarized [19].

Supermolecule density kernels (such as (4.4.9) and (4.4.12)) that involve at least one spin-polarized fragment density kernel would require a spin-polarized calculation as well. If, however, the supermolecule itself is not spin polarized, the molecular-orbital optimization of the supermolecule does not need to be spin polarized. On the other hand, if a species is not spin polarized, the calculation should not be spin polarized for faster calculations. Furthermore, different fragments can have different spin polarizations. This seemingly heterogeneous way of determining whether to carry out a calculation as a spin-polarized one contributed to the complexity of the original HALMO-EDA implementation.

Based on (3.4.4b), a possible simplification in implementing HALMO EDA for spin polarized fragments that is memory efficient, computationally economical, and structurally simpler is to perform spin-polarized calculations for spin-polarized fragments only. When fragments are brought together, calculations for HALMO frozen density and SCF MI would be spin polarized if any of the fragments are spin polarized. This would avoid the complexities in the original HALMO-EDA implementation that attempted, but was incomplete, at enabling spin-polarized calculations via *a posteriori* corrections to the electron densities. The proposed method of implementing spin-polarized HALMO EDA in the future work would instead be *a priori* in accommodating spin-polarized fragments.

Once spin-polarized HALMO EDA is implemented, further investigation of the DNA structures from §7 can be conducted with a fragmentation scheme that treats each base pair (as opposed to each DNA strand) as a fragment. Unlike other works [4, 17] where the phosphate backbone is removed for simplification, using a proper fragmentation scheme with spin-polarized EDA allows base-stacking effects to be studied without the non-native effects caused by a missing phosphate backbone. Furthermore, an error-correction scheme for breaking bonds [18] would become unnecessary.

10.3 EDA, Implicit Solvation, and Biomolecules

EDA in ONETEP currently does not support implicit solvation as part of its calculations. Since EDA has important applications in studying biological systems, enabling or reimplementing parts of EDA in ONETEP for implicit solvation would be beneficial, as biological systems are naturally in solution.

Enabling EDA to be used with implicit solvation would allow each EDA component to be determined in implicit water. This means that the resulting EDA components can be interpreted in the context of implicit solvation and how they are affected by the solvation environment. As an example, vdW can be defined in terms of EDA components [101, 102]. Since ONETEP EDA cannot be performed with implicit solvation, how the solvation environment affects the EDA components and, hence, vdW cannot be elucidated. Furthermore, many force fields and molecular-mechanics (MM) software packages like AmberTools were developed with biomolecules in mind. As such, being able to use EDA with implicit solvation would greatly expand its applicability beyond analyzing interaction energies of biomolecules in the artificial environment of vacuum.

EDA with implicit solvation would allow comparisons with energy decompositions by force fields in MM calculations, which was not possible in §7. Implicit solvation in EDA would contribute to the understanding of how drugs may interact differently with a target biomolecule if the system is in solution as opposed to vacuum, which is an artificial environment that can skew interactions and could thus lead to inaccurate interpretations based on such artificially induced interactions.

If enabled in ONETEP, EDA with implicit solvation could be applied to the same dsDNA structures in §7 to revisit the variability of each EDA component but in implicit water. Since implicit solvation affects the individual EDA components as well as the overall interaction energy, dissecting the interactions among fragments in implicit solvent given a fragmentation scheme would provide insights into the nature of biomolecular interactions and accelerate drug design through better understanding of the interactions.

References

[1] Han Chen and Chris-Kriton Skylaris. Analysis of DNA interactions and GC content with energy decomposition in large-scale quantum mechanical calculations. *Physical Chemistry Chemical Physics*, 23:8891–8899, 2021.

[2] Han Chen and Chris-Kriton Skylaris. Energy decomposition analysis method for metallic systems. *Physical Chemistry Chemical Physics*, 24:1702–1711, 2022.

[3] Laurence Hurst and Alexa Merchant. High guanine-cytosine content is not an adaptation to high temperature: a comparative analysis amongst prokaryotes. *Royal Society*, 268:493–497, 2001.

[4] Marcel Swart, Tushar van der Wijst, Célia Fonseca Guerra, and F. Matthias Bickelhaupt. π-π stacking tackled with density functional theory. *Journal of Molecular Modeling*, 13:1245–1257, 2007.

[5] AN Bootsma, AC Doney, and SE Wheeler. Predicting the Strength of Stacking Interactions between Heterocycles and Aromatic Amino Acid Side Chains. *Journal of the American Chemical Society*, 141:11027–11035, 2019.

[6] HA Toupkanloo and Z Rahmani. An in-depth study on noncovalent stacking interactions between DNA bases and aromatic drug fragments using DFT method and AIM analysis: conformers, binding energies, and charge transfer. *Applied Biological Chemistry*, 61:209–226, 2018.

[7] Peter Haynes, Chris-Kriton Skylaris, Arash Mostofi, and Mike Payne. ONETEP: linear-scaling density-functional theory with local orbitals and plane waves. *Physica Status Solidi B*, 243:2489–2499, 2006.

[8] Joseph C. A. Prentice, Jolyon Aarons, James C. Womack, Alice E. A. Allen, Lampros Andrinopoulos, Lucian Anton, Robert A. Bell, Arihant Bhandari, Gabriel A. Bramley, Robert J. Charlton, Rebecca J. Clements, Daniel J. Cole, Gabriel Constantinescu, Fabiano Corsetti, Simon M.-M. Dubois, Kevin K. B. Duff, José María Escartín, Andrea Greco, Quintin Hill, Louis P. Lee, Edward Linscott, David D. O'Regan, Maximillian J. S. Phipps, Laura E. Ratcliff, Álvaro Ruiz Serrano, Edward W. Tait, Gilberto Teobaldi, Valerio Vitale, Nelson Yeung, Tim J. Zuehlsdorff, Jacek Dziedzic, Peter D. Haynes, Nicholas D. M. Hine, Arash A. Mostofi, Mike C. Payne, and Chris-Kriton Skylaris. The ONETEP linear-scaling density functional theory program. *Journal of Chemical Physics*, 152:174111, 2020.

[9] Chris-Kriton Skylaris, Peter Haynes, Arash Mostofi, and Mike Payne. Introducing ONETEP: Linear-scaling density functional simulations on parallel computers. *Journal of Chemical Physics*, 122:084119, 2005.

[10] Jacek Dziedzic, Stephen Fox, Thomas Fox, Christofer Tautermann, and Chris-Kriton Skylaris. Large-Scale DFT Calculations in Implicit Solvent—A Case Study on the T4 Lysozyme L99A/M102Q Protein. *International Journal of Quantum Chemistry*, 113:771–785, 2013.

[11] Maximillian J. S. Phipps, Thomas Fox, Christofer S. Tautermann, and Chris-Kriton Skylaris. Energy decomposition analysis approaches and their evaluation on prototypical protein-drug interaction patterns. *Chemical Society Reviews*, 44: 3177–3211, 2015.

[12] Kazuo Kitaura and Keiji Morokuma. A new energy decomposition scheme for molecular interactions within the Hartree-Fock approximation. *International Journal of Quantum Chemistry*, 10:325–340, 1976.

[13] Rustam Khaliullin, Erika Cobar, Rohini Lochan, Alexis Bell, and Martin Head-Gordon. Unravelling the Origin of Intermolecular Interactions Using Absolutely Localized Molecular Orbitals. *Journal of Physical Chemistry*, 111:8753–8765, 2007.

[14] Peifeng Su and Hui Li. Energy decomposition analysis of covalent bonds and intermolecular interactions. *Journal of Chemical Physics*, 131:014102, 2009.

[15] Yirong Mo, Jiali Gao, and Sigrid D. Peyerimhoff. Energy decomposition analysis of intermolecular interactions using a block-localized wave function approach. *Journal of Chemical Physics*, 112:5530–5538, 2000.

[16] Yirong Mo, Peng Bao, and Jiali Gao. Energy decomposition analysis based on a block-localized wavefunction and multistate density functional theory. *Physical Chemistry Chemical Physics*, 13:6760–6775, 2011.

[17] Holger Kruse, Pavel Banáš, and Jiri Sponer. Investigations of Stacked DNA Base-Pair Steps: Highly Accurate Stacking Interaction Energies, Energy Decomposition, and Many-Body Stacking Effects. *Journal of Chemical Theory and Computation*, 15:95–115, 2019.

[18] M. J. S. Phipps, T. Fox, C. S. Tautermann, and C.-K. Skylaris. Intuitive Density Functional Theory-Based Energy Decomposition Analysis for Protein-Ligand Interactions. *Journal of Chemical Theory and Computation*, 13:1837–1850, 2017.

[19] M. J. S. Phipps, T. Fox, C. S. Tautermann, and C.-K. Skylaris. Energy Decomposition Analysis Based on Absolutely Localized Molecular Orbitals for Large-Scale Density Functional Theory Calculations in Drug Design. *Journal of Chemical Theory and Computation*, 12:3135–3148, 2016.

[20] P.D. Haynes, C.-K. Skylaris, A.A. Mostofi, and M.C. Payne. Elimination of basis set superposition error in linear-scaling density-functional calculations with local orbitals optimised in situ. *Chemical Physics Letters*, 422:345–349, 2006.

[21] Petr Šmarda, Petr Bureš, Lucie Horová, Ilia J. Leitch, Ladislav Mucina, Ettore Pacini, Lubomír Tichý, Vít Grulich, and Olga Rotreklová. Ecological and evolutionary significance of genomic GC content diversity in monocots. *Proceedings of the National Academy of Sciences*, 111:E4096–E4102, 2014.

[22] N Marzari, D. Vanderbilt, and M. C. Payne. Ensemble Density-Functional Theory for *Ab Initio* Molecular Dynamics of Metals and Finite-Temperature Insulators. *Physical Review Letters*, 79:1337, 1997.

[23] Álvaro Ruiz-Serrano and Chris-Kriton Skylaris. A variational method for density functional theory calculations on metallic systems with thousands of atoms. *Journal of Chemical Physics*, 139:054107, 2013.

[24] H. Toulhoat. Heterogeneous Catalysis: Use of Density Functional Theory. *Reference Module in Materials Science and Materials Engineering*, pages 1–7, 2016.

[25] M Campanati, G Fornasari, and A Vaccari. Fundamentals in the preparation of heterogeneous catalysts. *Catalysis Today*, 77:299–314, 2003.

[26] Graham J. Hutchings. Heterogeneous catalysts—discovery and design. *Journal of Materials Chemistry*, 19:1222–1235, 2009.

[27] Aleksandra Vojvodic and Jens K. Nørskov. New design paradigm for heterogeneous catalysts. *National Science Review*, 2:140–143, 2015.

[28] Attila Szabo and Neil Ostlund. *Modern Quantum Chemistry: Introduction to Advanced Electronic Structure Theory*. Dover Publications, 1996.

[29] Per-Olov Löwdin. Quantum Theory of Many-Particle Systems. *Physical Review*, 97:1474–1489, 1955.

[30] R. McWeeny. Some Recent Advances in Density Matrix Theory. *Reviews of Modern Physics*, 32:335–369, 1960.

[31] Robert Parr and Weitao Yang. *Density-Functional Theory of Atoms and Molecules*. Oxford University Press, 1989.

[32] J. F. Janak. Proof that $\partial E/\partial n_i = \epsilon_i$ in density-functional theory. *Physical Review B*, 18:7165–7168, 1978.

[33] A. J. Coleman. Structure of Fermion Density Matrices. *Reviews of Modern Physics*, 35:668–687, 1963.

[34] P. Hohenberg and W. Kohn. Inhomogenous Electron Gas. *Physical Review*, 136: 864–871, 1964.

[35] W. Kohn and L. J. Sham. Self-Consistent Equations Including Exchange and Correlation Effects. *Physical Review*, 140:1133–1138, 1965.

[36] John P. Perdew, Adrienn Ruzsinszky, Jianmin Tao, Viktor N. Staroverov, Gustavo E. Scuseria, and Gábor I. Csonka. Prescription for the design and selection of density functional approximations: More constraint satisfaction with fewer fits. *Journal of Chemical Physics*, 123:062201, 2005.

[37] Takao Tsuneda. *Density Functional Theory in Quantum Chemistry*. Springer, 2014.

[38] S. H. Vosko, L. Wilk, and M. Nusair. Accurate spin-dependent electron liquid correlation energies for local spin density calculations: a critical analysis. *Canadian Journal of Physics*, 58:1200–1211, 1980.

[39] John P. Perdew and Yue Wang. Accurate and simple analytic representation of the electron-gas correlation energy. *Physical Review B*, 45:13244–13249, 1992.

[40] Axel D. Becke. Density-functional thermochemistry. V. Systematic optimization of exchange-correlation functionals. *Journal of Chemical Physics*, 107:8554–8560, 1997.

[41] John P. Perdew, Kieron Burke, and Matthias Ernzerhof. Generalized Gradient Approximation Made Simple. *Physical Review Letters*, 77:3865–3868, 1996.

[42] James Womack, Narbe Mardirossian, Martin Head-Gordon, and Chris-Kriton Skylaris. Self-consistent implementation of meta-GGA functionals for the ONETEP linear-scaling electronic structure package. *Journal of Chemical Physics*, 145:204114, 2016.

[43] Troy Van Voorhis and Gustavo E. Scuseria. A novel form for the exchange-correlation energy functional. *Journal of Chemical Physics*, 109:400–410, 1998.

[44] John P. Perdew, Stefan Kurth, Aleš Zupan, and Peter Blaha. Accurate Density Functional with Correct Formal Properties: A Step Beyond the Generalized Gradient Approximation. *Physical Review Letters*, 82:2544–2547, 1999.

[45] Jianmin Tao, John P. Perdew, Viktor N. Staroverov, and Gustavo E. Scuseria. Climbing the Density Functional Ladder: Nonempirical Meta-Generalized Gradient Approximation Designed for Molecules and Solids. *Physical Review Letters*, 91:146401, 2003.

[46] Narbe Mardirossian and Martin Head-Gordon. Mapping the genome of meta-generalized gradient approximation density functionals: The search for B97M-V. *Journal of Chemical Physics*, 142:074111, 2015.

[47] Cesare Franchini. Hybrid functionals applied to perovskites. *Journal of Physics*, 26:253202, 2014.

[48] Axel D. Becke. A new mixing of Hartree-Fock and local density-functional theories. *Journal of Chemical Physics*, 98:1372–1377, 1993.

[49] Carlo Adamo and Vincenzo Barone. Toward reliable density functional methods without adjustable parameters: The PBE0 model. *Journal of Chemical Physics*, 110: 6158–6170, 1999.

[50] Jochen Heyd, Gustavo E. Scuseria, and Matthias Ernzerhof. Hybrid functionals based on a screened Coulomb potential. *Journal of Chemical Physics*, 118:8207–8215, 2003.

[51] A. D. Becke. Density-functional exchange-energy approximation with correct asymptotic behavior. *Physical Review A*, 38:3098–3100, 1988.

[52] Chengteh Lee, Weitao Yang, and Robert G. Parr. Development of the Colle-Salvetti correlation-energy formula into a functional of the electron density. *Physical Review B*, 37:785–789, 1988.

[53] E. Prodan and W. Kohn. Nearsightedness of electronic matter. *Proceedings of the National Academy of Sciences*, 102:11635–11638, 2005.

[54] Chris-Kriton Skylaris, Arash Mostofi, Peter Haynes, Oswaldo Diéguez, and Mike Payne. Nonorthogonal generalized Wannier function pseudopotential plane-wave method. *Physical Review*, 66:035119, 2002.

[55] Arash Mostofi, Chris-Kriton Skylaris, Peter Haynes, and Mike Payne. Total-energy calculations on a real space grid with localized functions and a plane-wave basis. *Computer Physics Communications*, 147:788–802, 2002.

[56] X.-P. Li, R. W. Nunes, and David Vanderbilt. Density-matrix electronic-structure method with linear system-size scaling. *Physical Review B*, 47:10891–10894, 1993.

[57] R. W. Nunes and David Vanderbilt. Generalization of the density-matrix method to a nonorthogonal basis. *Physical Review B*, 50:17611–17614, 1994.

[58] P D Haynes, C-K Skylaris, A A Mostofi, and M C Payne. Density kernel optimization in the ONETEP code. *Journal of Physics: Condensed Matter*, 20:294207, 2008.

[59] Å Björck. Numerics of Gram-Schmidt Orthogonalization. *Linear Algebra and its Applications*, 197–198:297–316, 1994.

[60] Keiji Morokuma. Molecular Orbital Studies of Hydrogen Bonds. III. C=O$\cdots$H–O Hydrogen Bond in $H_2CO\cdots H_2O$ and $H_2CO\cdots{}_2H_2O$. *Journal of Chemical Physics*, 55:1236–1244, 1971.

[61] Keiji Morokuma. Why Do Molecules Interact? The Origin of Electron Donor-Acceptor Complexes, Hydrogen Bonding, and Proton Affinity. *Accounts of Chemical Research*, 10:294–300, 1977.

[62] Walter J. Stevens and William H. Fink. Frozen fragment reduced variational space analysis of hydrogen bonding interactions. Application to the water dimer. *Chemical Physics Letters*, 139:15–22, 1987.

[63] Paul S. Bagus, K. Hermann, and Charles W. Bauschlicher. A new analysis of charge transfer and polarization for ligand-metal bonding: Model studies of Al_4CO and Al_4NH_3. *Journal of Chemical Physics*, 80:4378–4386, 1984.

[64] Paul S. Bagus and Francesc Illas. Decomposition of the chemisorption bond by constrained variations: Order of the variations and construction of the variational spaces. *Journal of Chemical Physics*, 96:8962–8970, 1992.

[65] J. P. Foster and F. Weinhold. Natural Hybrid Orbitals. *Journal of the American Chemical Society*, 102:7211–7218, 1980.

[66] Alan E. Reed and Frank Weinhold. Natural localized molecular orbitals. *Journal of Chemical Physics*, 83:1736–1740, 1985.

[67] Eric D. Glendening and Andrew Streitwieser. Natural energy decomposition analysis: An energy partitioning procedure for molecular interactions with application to weak hydrogen bonding, strong ionic, and moderate donor-acceptor interactions. *Journal of Chemical Physics*, 100:2900–2909, 1994.

[68] Eric D. Glendening. Natural Energy Decomposition Analysis: Explicit Evaluation of Electrostatic and Polarization Effects with Application to Aqueous Clusters of Alkali Metal Cations and Neutrals. *Journal of the American Chemical Society*, 118:2473–2482, 1996.

[69] Eric D. Glendening. Natural Energy Decomposition Analysis: Extension to Density Functional Methods and Analysis of Cooperative Effects in Water Clusters. *Journal of Physical Chemistry A*, 109:11936–11940, 2005.

[70] Gregory K. Schenter and Eric D. Glendening. Natural Energy Decomposition Analysis: The Linear Response Electrical Self Energy. *Journal of Physical Chemistry*, 100:17152–17156, 1996.

[71] Dariusz Szczepanik and Janusz Mrozek. Symmetric orthogonalization within linear space of molecular orbitals. *Chemical Physics Letters*, 521:157–160, 2012.

[72] B. Carlson and Joseph Keller. Orthogonalization Procedures and the Localization of Wannier Functions. *Physical Review*, 105:102–103, 1957.

[73] Aaron West. Weighted orthogonalization of atomic orbitals: A stable alternative to the Carlson-Keller method. *Computational and Theoretical Chemistry*, 1045:73–77, 2014.

[74] Sanguthevar Rajasekaran and Mingjun Song. A relaxation scheme for increasing the parallelism in Jacobi-SVD. *Journal of Parallel and Distributed Computing*, 68: 769–777, 2008.

[75] Maciej Gutowski and Grzegorz Chałasiński. Critical evaluation of some computational approaches to the problem of basis set superposition error. *Journal of Chemical Physics*, 98:5540–5554, 1993.

[76] Frank Jensen. Using valence bond methods to estimate intramolecular basis set superposition errors. *Journal of Chemical Physics*, 146:184109, 2017.

[77] Peter Politzer and Harel Weinstein. Some relations between electronic distribution and electronegativity. *Journal of Chemical Physics*, 71:4218–4220, 1979.

[78] G. Del Re, P. Otto, and J. Ladik. Studies on Charge-Transfer Theory Mulliken Population and Measure of Charge Transfer. *Israel Journal of Chemistry*, 19:265–271, 1980.

[79] Hermann Stoll, Gerhard Wagenblast, and Heinzwerner Preuβ. On the Use of Local Basis Sets for Localized Molecular Orbitals. *Theoretical Chemistry Accounts*, 57:169–178, 1980.

[80] E Gianinetti, M Raimondi, and E Tornaghi. Modification of the Roothaan Equations to Exclude BSSE from Molecular Interaction Calculations. *International Journal of Quantum Chemistry*, 60:157–166, 1996.

[81] Takeshi Nagata, Osamu Takahashi, Ko Saito, and Suehiro Iwata. Basis set superposition error free self-consistent field method for molecular interaction in multicomponent systems: Projection operator formalism. *Journal of Chemical Physics*, 115:3553–3560, 2001.

[82] Zsolt Szekeres and Péter Surján. Direct determination of fragment localized molecular orbitals and the orthogonality constraint. *Chemical Physics Letters*, 369: 125–130, 2003.

[83] Arash Mostofi, Peter Haynes, Chris-Kriton Skylaris, and Mike Payne. Preconditioned iterative minimization for linear-scaling electronic structure calculations. *Journal of Chemical Physics*, 119:8842–8848, 2003.

[84] Rustam Khaliullin, Martin Head-Gordon, and Alexis Bell. An efficient self-consistent field method for large systems of weakly interacting components. *Journal of Chemical Physics*, 124:204105, 2006.

[85] S. Huzinaga and A. A. Cantu. Theory of Separability of Many-Electron Systems. *Journal of Chemical Physics*, 55:5543–5549, 1971.

[86] Manchuta Dangkulwanich, Toyotaka Ishibashi, Lacramioara Bintu, and Carlos Bustamante. Molecular Mechanisms of Transcription through Single-Molecule Experiments. *Chemical Reviews*, 114:3203–3223, 2014.

[87] Aimée Deaton and Adrian Bird. CpG islands and the regulation of transcription. *Genes & Development*, 25:1010–1022, 2011.

[88] Navin Elango and Soojin Yi. Functional Relevance of CpG Island Length for Regulation of Gene Expression. *Genetics*, 187:1077–1083, 2011.

[89] Karunganathan Sakthikumar, Jeyaraj Raja, Rajadural Solomon, and Murugesan Sankarganesh. Density functional theory molecular modelling, DNA interactions, antioxidant, antimicrobial, anticancer and biothermodynamic studies of bioactive water soluble mixed ligand complexes. *Journal of Biomolecular Structure and Dynamics*, 37:2498–2514, 2019.

[90] Jun Li, Lian-Cai Xu, Jin-Chan Chen, Kang-Cheng Zheng, and Liang-Nian Ji. Density Functional Theory/Time-dependent DFT Studies on the Structures, Trend in DNA-binding Affinities, and Spectral Properties of Complexes. *Journal of Physical Chemistry A*, 110:8174–8180, 2006.

[91] Bogumil Jeziorski, Robert Moszynski, and Krzysztof Szalewicz. Perturbation Theory Approach to Intermolecular Potential Energy Surfaces of van der Waals Complexes. *Chemical Reviews*, 94:1887–1930, 1994.

[92] Konrad Patkowski. Recent developments in symmetry-adapted perturbation theory. *WIREs Computational Molecular Science*, 10:e1452, 2020.

[93] Jesse McDaniel and J.R. Schmidt. Next-Generation Force Fields from Symmetry-Adapted Perturbation Theory. *Annual Review of Physical Chemistry*, 67:467–488, 2016.

[94] Rui Qi, Qiantao Wang, and Pengyu Ren. General van der Waals potential for common organic molecules. *Bioorganic & Medicinal Chemistry*, 24:4911–4919, 2016.

[95] David A. Case, Thomas E. Cheatham, Tom Darden, Holger Gohlke, Ray Luo, Kenneth M. Merz, Alexey Onufriev, Carlos Simmerling, Bing Wang, and Robert J.

Woods. The Amber Biomolecular Simulation Programs. *Journal of Computational Chemistry*, 26:1668–1688, 2005.

[96] Gregory D. Hawkins, Christopher J. Cramer, and Donald G. Truhlar. Pairwise solute descreening of solute charges from a dielectric medium. *Chemical Physics Letters*, 246:122–129, 1995.

[97] Gregory D. Hawkins, Christopher J. Cramer, and Donald G. Truhlar. Parametrized Models of Aqueous Free Energies of Solvation Based on Pairwise Descreening of Solute Atomic Charges from a Dielectric Medium. *Journal of Physical Chemistry*, 100:19824–19839, 1996.

[98] Vickie Tsui and David A. Case. Theory and Applications of the Generalized Born Solvation Model in Macromolecular Simulations. *Biopolymers (Nucleic Acid Sciences)*, 56:275–291, 2001.

[99] Richard Brent. *Algorithms for Minimization without Derivatives*. Dover, 2002.

[100] Stefan Grimme. Semiempirical GGA-Type Density Functional Constructed with a Long-Range Dispersion Correction. *Journal of Computational Chemistry*, 27:1787–1799, 2006.

[101] Yuezhi Mao, Omar Demerdash, Martin Head-Gordon, and Teresa Head-Gordon. Assessing Ion-Water Interactions in the AMOEBA Force Field Using Energy Decomposition Analysis of Electronic Structure Calculations. *Journal of Chemical Theory and Computation*, 12:5422–5437, 2016.

[102] Yuezhi Mao, Yihan Shao, Jacek Dziedzic, Chris-Kriton Skylaris, Teresa Head-Gordon, and Martin Head-Gordon. Performance of the AMOEBA Water Model in the Vicinity of QM Solutes: A Diagnosis Using Energy Decomposition Analysis. *Journal of Chemical Theory and Computation*, 13:1963–1979, 2017.

[103] I. Mayer. A chemical energy component analysis. *Chemical Physics Letters*, 332: 381–388, 2000.

[104] I. Mayer. An exact chemical decomposition scheme for the molecular energy. *Chemical Physics Letters*, 382:265–269, 2003.

[105] S. Pittalis, C. R. Proetto, A. Floris, A. Sanna, C. Bersier, K. Burke, and E. K. U. Gross. Exact Conditions in Finite-Temperature Density-Functional Theory. *Physical Review Letters*, 107:163001, 2011.

[106] J. C. Smith, A. Pribram-Jones, and K. Burke. Exact thermal density functional theory for a model system: Correlation components and accuracy of the zero-temperature exchange-correlation approximation. *Physical Review B*, 93:245131, 2016.

[107] Tim Gould. Approximately Self-Consistent Ensemble Density Functional Theory: Toward Inclusion of All Correlations. *Journal of Physical Chemistry Letters*, 11: 9907–9912, 2020.

[108] Tim Gould, Gianluca Stefanucci, and Stefano Pittalis. Ensemble Density Functional Theory: Insight from the Fluctuation-Dissipation Theorem. *Physical Review Letters*, 125:233001, 2020.

[109] Bruno Senjean and Emmanuel Fromager. N-centered ensemble density-functional theory for open systems. *International Journal of Quantum Chemistry*, 120:e26190, 2020.

[110] Q.A. Wang. Correlated electrons and generalized statistics. *European Physical Journal B*, 31:75–79, 2003.

[111] M. Angst. Strongly correlated electrons. In *Lectures of the JCNS Laboratory Course*, 2012.

[112] Qinghui Ge, Yuezhi Mao, and Martin Head-Gordon. Energy decomposition analysis for exciplexes using absolutely localized molecular orbitals. *Journal of Chemical Physics*, 148:064105, 2018.

[113] Gerald Knizia. Intrinsic Atomic Orbitals: An Unbiased Bridge between Quantum Theory and Chemical Concepts. *Journal of Chemical Theory and Computation*, 9: 4834–4843, 2013.

[114] Bruno Senjean, Souloke Sen, Michal Repisky, Gerald Knizia, and Lucas Visscher. Generalization of Intrinsic Orbitals to Kramers-Paired Quaternion Spinors,

Molecular Fragments, and Valence Virtual Spinors. *Journal of Chemical Theory and Computation*, 17:1337–1354, 2021.

[115] Tom Ellaby, Ludovic Briquet, Misbah Sarwar, David Thompsett, and Chris-Kriton Skylaris. Modification of O and CO binding on Pt nanoparticles due to electronic and structural effects of titania supports. *Journal of Chemical Physics*, 151:114702, 2019.

[116] B. Hammer, L. B. Hansen, and J. K. Nørskov. Improved adsorption energetics within density-functional theory using revised Perdew-Burke-Ernzerhof functionals. *Physical Review B*, 59:7413–7421, 1999.

[117] M. Dion, H. Rydberg, E. Schröder, D. C. Langreth, and B. I. Lundqvist. Van der Waals Density Functional for General Geometries. *Physical Review Letters*, 92: 246401, 2004.

[118] Neeru Chaudhary, Alyssa Hensley, Greg Collinge, Yong Wang, and Jean-Sabin McEwen. Coverage-Dependent Adsorption of Phenol on Pt(111) from First Principles. *Journal of Physical Chemistry*, 124:356–362, 2020.

[119] Gabriel A. Bramley, Manh-Thuong Nguyen, Vassiliki-Alexandra Glezakou, Roger Rousseau, and Chris-Kriton Skylaris. Understanding Adsorption of Organics on Pt(111) in the Aqueous Phase: Insights from DFT Based Implicit Solvent and Statistical Thermodynamics Models. *Journal of Chemical Theory and Computation*, 18:1849–1861, 2022.

[120] Chao Peng. Mechanism of Li nucleation at graphite anodes and mitigation strategies. *Journal of Materials Chemistry A*, 9:16798–16804, 2021.

[121] Peifeng Su, Zuochang Chen, and Wei Wu. An energy decomposition analysis study for intramolecular non-covalent interaction. *Chemical Physics Letters*, 635: 250–256, 2015.

[122] Thomas Halgren. Representation of van der Waals (vdW) Interactions in Molecular Mechanics Force Fields: Potential Form, Combination Rules, and vdW Parameters. *Journal of the American Chemical Society*, 114:7827–7843, 1992.

[123] Christoph Freysoldt, Sixten Boeck, and Jörg Neugebauer. Direct minimization technique for metals in density functional theory. *Physical Review B*, 79:241103, 2009.

Appendix A

CLMO EDA Validation Benchmarks

CLMO EDA calculations from ONETEP and GAMESS-US were done on water dimer, water-ammonia dimer, and water-ammonium dimer, where all geometries were optimized by Tinker using the AMOEBA09 force field and are in their hydrogen-bonding equilibrium orientations. It is important to note that GAMESS-US does not have CLMO EDA per se, but rather, it is derived from the BSSE-uncorrected and BSSE-corrected LMO-EDA components (cf. §4.5.3).

For both ONETEP CLMO EDA and GAMESS-US, PBE and PKZB exchange-correlation functionals were used. Unlike ONETEP, GAMESS-US does not have an implementation of the B97M-V functional. 800 eV cutoff energy and 8.0 Bohr NGWF radius were used for ONETEP. Three augmented correlation-consistent basis sets were used for GAMESS-US: aug-cc-pVDZ, aug-cc-pVTZ, and aug-cc-pVQZ. Grimme dispersion correction was not done for simplicity and comparison reasons. Comparisons for each CLMO EDA component are made to demonstrate the similarity of the values that were obtained from the two software packages.

Starting with the comparison for water dimer, each EDA component is in good agreement between ONETEP and GAMESS-US within each exchange-correlation functional that was used. With the exception of repulsion, the difference between each component as well as the overall interaction energy is well under 1 kcal/mol, with some of them differing less than 0.2 kcal/mol. When comparing PBE and PKZB, the interaction energies differ by almost 3 kcal/mol for both packages.

TABLE A.1: CLMO EDA of water dimer using the PBE exchange-correlation functional. Grimme dispersion correction was not done. 800 eV cutoff energy and 8.0 Bohr NGWF radius were used for ONETEP. All energy values are in kcal/mol.

CLMO EDA of Water Dimer with PBE				
EDA Component	ONETEP	GAMESS-US		
		aug-cc-pVDZ	aug-cc-pVTZ	aug-cc-pVQZ
Electrostatics	−8.10	−8.65	−8.36	−8.36
Exchange	−3.32	−3.25	−3.50	−3.51
Repulsion	11.76	12.57	12.53	12.60
Polarization	−3.46	−3.40	−3.51	−3.63
Dispersion	−2.03	−2.24	−2.15	−2.14
Interaction Energy	−5.15	−4.97	−4.99	−5.04

TABLE A.2: CLMO EDA of water dimer using the PKZB exchange-correlation functional. Grimme dispersion correction was not done. 800 eV cutoff energy and 8.0 Bohr NGWF radius were used for ONETEP. All energy values are in kcal/mol.

CLMO EDA of Water Dimer with PKZB				
EDA Component	ONETEP	GAMESS-US		
		aug-cc-pVDZ	aug-cc-pVTZ	aug-cc-pVQZ
Electrostatics	−8.04	−8.35	−8.25	−8.28
Exchange	−0.80	−1.07	−0.96	−1.01
Repulsion	11.39	12.44	12.35	12.43
Polarization	−3.04	−2.99	−3.12	−3.19
Dispersion	−1.90	−2.11	−2.02	−2.03
Interaction Energy	−2.37	−2.08	−2.00	−2.08

For ALMO EDA, the component responsible for such a large difference in interaction energy of water dimer between PBE and PKZB is the frozen density. But since ALMO EDA does not further decompose the frozen density, the part of the frozen density that is contributing to the large difference in interaction energy is not known. On the contrary, CLMO EDA demonstrates that it is the exchange component that is contributing to the large difference in the overall interaction energies of water dimer when comparing between the two functionals, while other components exhibit only minor differences. Similar trends and differences exist for water-ammonia and water-ammonium dimers as well.

TABLE A.3: CLMO EDA of water-ammonia using the PBE exchange-correlation functional. Grimme dispersion correction was not done. 800 eV cutoff energy and 8.0 Bohr NGWF radius were used for ONETEP. All energy values are in kcal/mol.

CLMO EDA of Water-Ammonia with PBE				
EDA Component	ONETEP	GAMESS-US		
		aug-cc-pVDZ	aug-cc-pVTZ	aug-cc-pVQZ
Electrostatics	−10.56	−11.32	−11.21	−11.25
Exchange	−4.24	−4.92	−4.77	−4.80
Repulsion	15.71	17.49	17.33	17.49
Polarization	−5.43	−5.10	−5.32	−5.43
Dispersion	−2.55	−2.83	−2.77	−2.76
Interaction Energy	−7.07	−6.68	−6.74	−6.75

TABLE A.4: CLMO EDA of water-ammonia using the PKZB exchange-correlation functional. Grimme dispersion correction was not done. 800 eV cutoff energy and 8.0 Bohr NGWF radius were used for ONETEP. All energy values are in kcal/mol.

CLMO EDA of Water-Ammonia with PKZB				
EDA Component	ONETEP	GAMESS-US		
		aug-cc-pVDZ	aug-cc-pVTZ	aug-cc-pVQZ
Electrostatics	−10.51	−11.37	−11.13	−11.18
Exchange	−1.36	−2.07	−1.82	−1.88
Repulsion	15.39	17.51	17.21	17.39
Polarization	−4.91	−4.61	−4.83	−4.93
Dispersion	−2.36	−2.62	−2.56	−2.57
Interaction Energy	−3.75	−3.16	−3.13	−3.17

TABLE A.5: CLMO EDA of water-ammonium dimer using the PBE exchange-correlation functional. Grimme dispersion correction was not done. 800 eV cutoff energy and 8.0 Bohr NGWF radius were used for ONETEP. All energy values are in kcal/mol.

CLMO EDA of Water-Ammonium Dimer with PBE				
EDA Component	ONETEP	GAMESS-US		
		aug-cc-pVDZ	aug-cc-pVTZ	aug-cc-pVQZ
Electrostatics	−22.44	−21.91	−22.23	−22.23
Exchange	−4.83	−4.82	−4.90	−4.88
Repulsion	22.14	22.51	22.89	22.97
Polarization	−11.99	−12.12	−12.29	−12.43
Dispersion	−3.60	−3.80	−3.79	−3.80
Interaction Energy	−20.72	−20.14	−20.32	−20.37

TABLE A.6: CLMO EDA of water-ammonium dimer using the PKZB exchange-correlation functional. Grimme dispersion correction was not done. 800 eV cutoff energy and 8.0 Bohr NGWF radius were used for ONETEP. All energy values are in kcal/mol.

CLMO EDA of Water-Ammonium Dimer with PKZB				
EDA Component	ONETEP	GAMESS-US		
		aug-cc-pVDZ	aug-cc-pVTZ	aug-cc-pVQZ
Electrostatics	−22.42	−21.66	−21.83	−21.86
Exchange	−1.48	−1.47	−1.51	−1.53
Repulsion	21.69	22.20	22.47	22.58
Polarization	−11.19	−11.21	−11.49	−11.63
Dispersion	−3.35	−3.53	−3.51	−3.52
Interaction Energy	−16.75	−15.67	−15.87	−15.96

Appendix B

ICGS, WO, and GRS Performance Data

TABLE B.1: Performance data of iterated classical Gram-Schmidt (cf. §5.2.2). Matrices are square with sizes indicated as the number of rows/columns. Durations are in minutes.

Iterated Classical Gram-Schmidt		
Square Matrix Size	With Basis Overlap	Without Basis Overlap
500	0.001	0.000
1000	0.007	0.001
1500	0.023	0.003
2000	0.060	0.006
2500	0.132	0.012
3000	0.245	0.020
3500	0.399	0.031
4000	0.613	0.046
4500	0.884	0.065
5000	1.225	0.088
5500	1.646	0.117
6000	2.157	0.152
6500	2.734	0.193
7000	3.415	0.249
7500	4.223	0.314
8000	5.145	0.399
8500	6.148	0.518
9000	7.275	0.639
9500	8.602	0.879
10 000	10.025	1.112

TABLE B.2: Performance data of weighted orthogonalization by matrix size (cf. §5.2.2). Matrices are square with sizes indicated as the number of rows/columns. Durations are in minutes. Matrix sizes beyond 5000 are not benchmarked for the implementation where a basis overlap is used.

Weighted Orthogonalization by Matrix Size			
Square Matrix Size	With Basis Overlap Shared Memory	Without Basis Overlap Distributed Memory	Without Basis Overlap Shared Memory
500	0.009	0.012	0.001
1000	0.462	0.092	0.002
1500	2.526	0.294	0.007
2000	7.956	0.693	0.015
2500	20.314	1.329	0.031
3000	43.922	2.359	0.057
3500	86.033	3.850	0.125
4000	153.644	5.936	0.270
4500	222.494	8.620	0.401
5000	335.797	12.103	0.593
5500		16.340	0.831
6000		21.128	1.127
6500		28.222	1.442
7000		35.834	1.857
7500		41.969	2.292
8000		51.058	2.653
8500		66.489	3.415
9000		80.461	4.104
9500		105.722	4.921
10 000		123.157	5.912

TABLE B.3: Performance data of weighted orthogonalization by number of MPI processes (cf. §5.3.3). Durations are in minutes.

Weighted Orthogonalization by Number of Processes			
Number of Processes	Matrix Size $10\,000 \times 10\,000$	Matrix Size 7500×7500	Matrix Size 5000×5000
1	39.324	16.556	4.770
2	20.930	8.687	2.439
3	14.414	5.996	1.620
4	12.118	4.989	1.248
5	10.403	4.244	0.995
6	9.374	3.745	0.811
7	8.880	3.523	0.789
8	8.539	3.364	0.764
9	8.283	3.241	0.767
10	8.130	3.162	0.745

TABLE B.4: Performance data of weighted orthogonalization by number of hosts (cf. §5.3.3). Durations are in minutes.

Weighted Orthogonalization by Number of Hosts			
Number of Hosts	Matrix Size $10\,000 \times 10\,000$	Matrix Size 7500×7500	Matrix Size 5000×5000
1	8.494	3.157	0.745
2	5.912	2.292	0.593
3	5.304	2.174	0.554
4	5.134	2.061	0.529
5	4.709	1.951	0.498
6	4.949	1.999	0.571
7	4.694	1.982	0.581
8	4.724	1.946	0.553

Appendix C

Distributions of HALMO-EDA Components by GC Content

The different HALMO-EDA components and GC contents of the 4bp dsDNA structures in this study are depicted as histograms for comparing how the energies vary within the 25%, 50%, and 75% GC-content categories as distributions. The 0% and 100% GC-content categories are not depicted due to their low sample size of only 10 sequences. Since ONETEP EDA does not support implicit solvation, only HALMO EDA in vacuum is available.

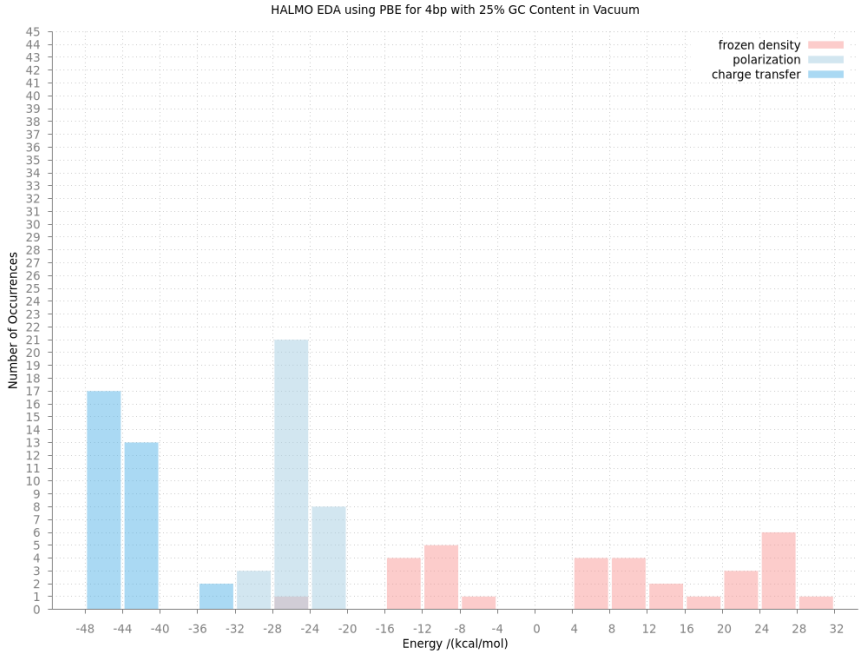

FIGURE C.1: HALMO-EDA frozen density (red), polarization (light blue), and charge transfer (blue) using PBE for 4bp dsDNA with 25% GC content in vacuum.

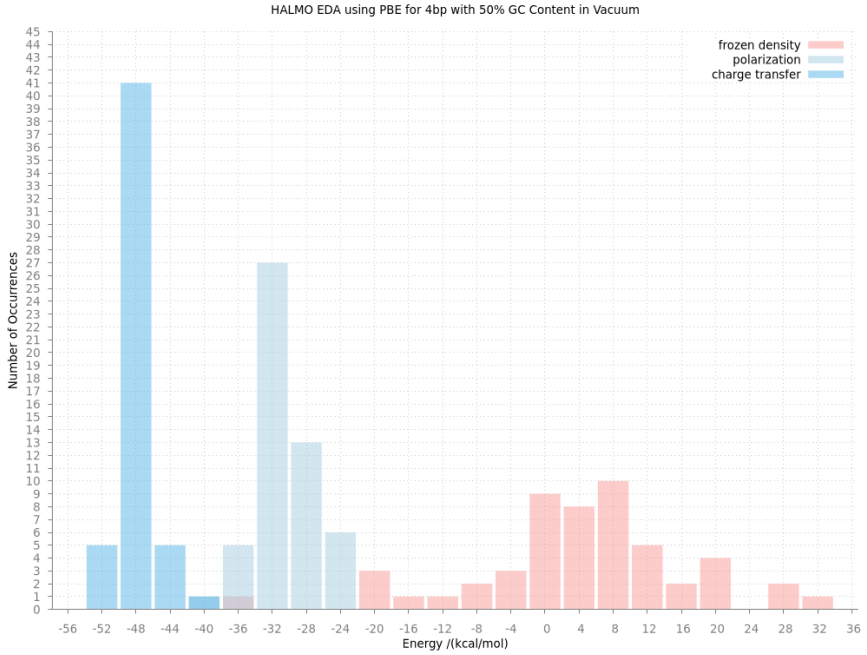

FIGURE C.2: HALMO-EDA frozen density (red), polarization (light blue), and charge transfer (blue) using PBE for 4bp dsDNA with 50% GC content in vacuum.

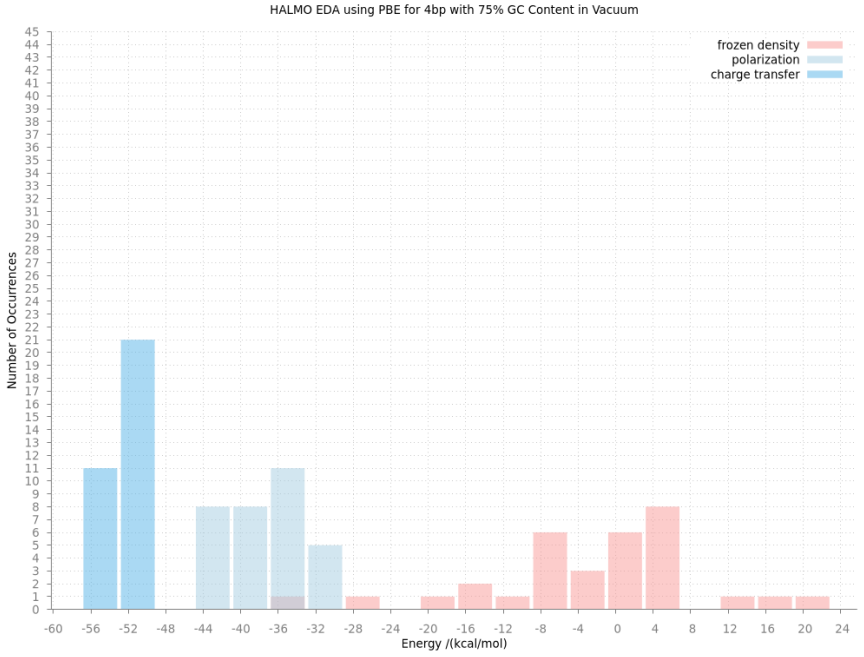

FIGURE C.3: HALMO-EDA frozen density (red), polarization (light blue), and charge transfer (blue) using PBE for 4bp dsDNA with 75% GC content in vacuum.

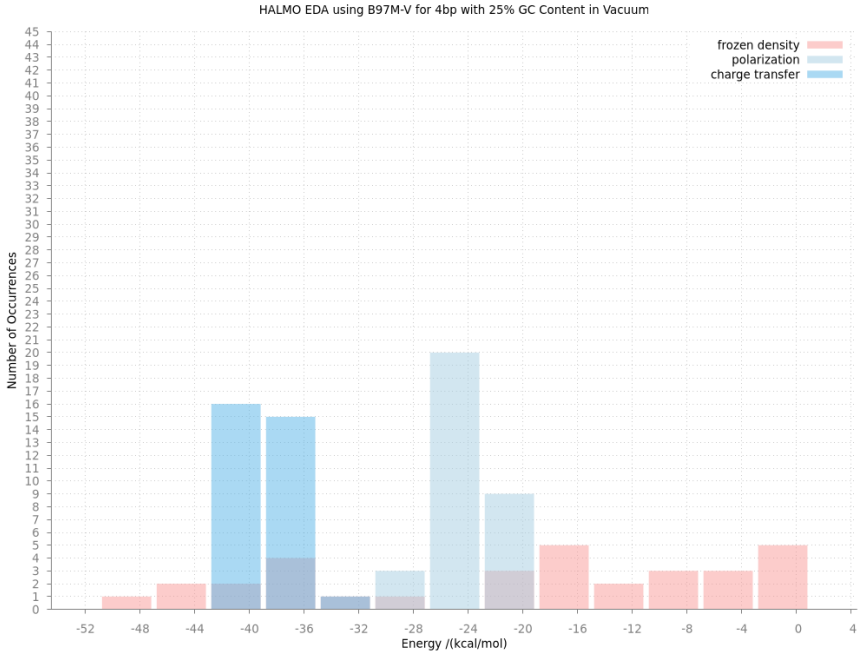

FIGURE C.4: HALMO-EDA frozen density (red), polarization (light blue), and charge transfer (blue) using B97M-V for 4bp dsDNA with 25% GC content in vacuum.

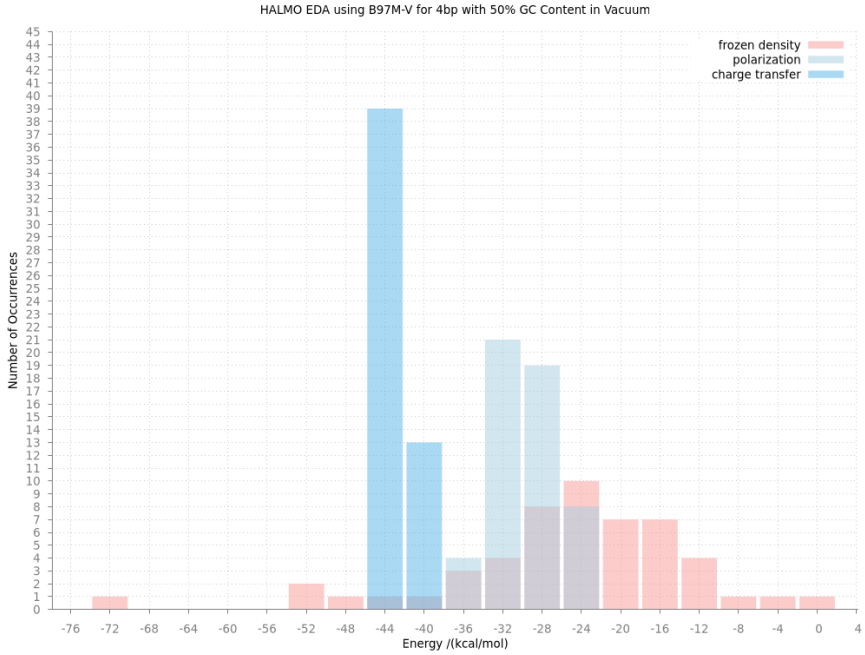

FIGURE C.5: HALMO-EDA frozen density (red), polarization (light blue), and charge transfer (blue) using B97M-V for 4bp dsDNA with 50% GC content in vacuum.

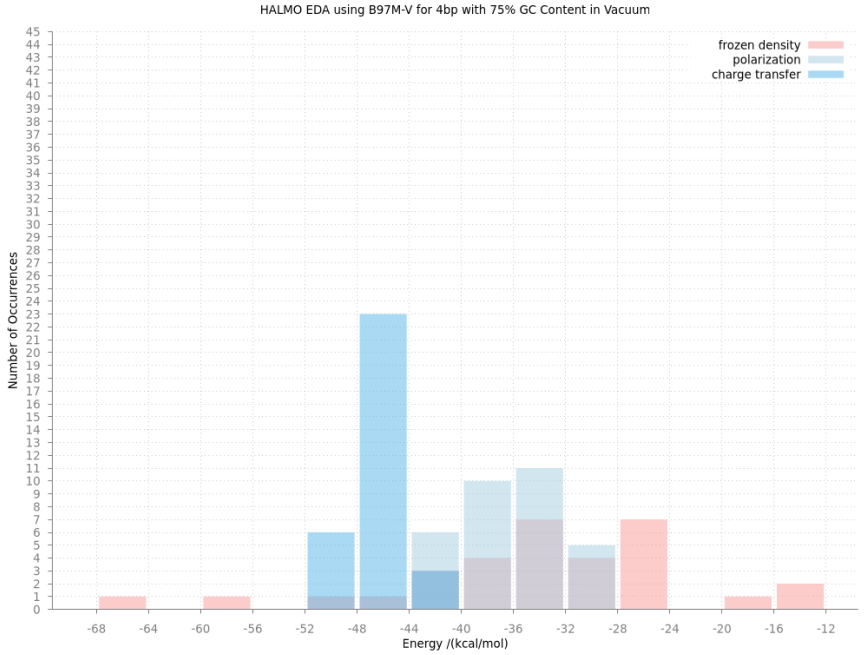

FIGURE C.6: HALMO-EDA frozen density (red), polarization (light blue), and charge transfer (blue) using B97M-V for 4bp dsDNA with 75% GC content in vacuum.

TABLE C.1: VdW energies for 4bp dsDNA in vacuum using HALMO EDA, BSC1 force field, and vdW2017 force field categorized by GC content. In HALMO EDA, vdW is defined either as the empirical dispersion correction (for PBE) or as the correlation component (for B97M-V). In BSC1, there is a dedicated component for vdW. For vdW2017, each atom is assigned an atom class, and then the vdW energy between the two DNA strands is calculated for each dsDNA structure. All energy values are in kcal/mol. Abbreviations: MAD, median absolute deviation

GC	PBE		B97M-V		BSC1		VdW2017	
Content	Median	MAD	Median	MAD	Median	MAD	Median	MAD
0%	-22.5	1.1	-9.2	0.4	-17.8	0.8	48.9	0.7
25%	-24.1	0.8	-21.1	12.4	-17.4	0.9	58.2	1.2
50%	-24.9	1.4	-10.1	0.6	-17.2	1.3	68.1	0.7
75%	-25.9	1.2	-10.4	0.5	-16.9	1.1	77.6	0.6
100%	-27.0	1.3	-11.0	0.7	-17.2	0.9	87.7	0.6

C.1 Comparisons with VdW2017

VdW2017 (updated from vdW2016) is a van der Waals (vdW) potential parameterized against SAPT [94] and can be used to calculate vdW energies between the two strands for each 4bp dsDNA (Table C.1). Prior to calculating such energies, each atom was assigned an atom class according to the vdW2017 parameter set. The functional form used by vdW2017 is Buffered 14-7 (Buf-14-7) [122], with $\delta = 0.201303$ and $\gamma = 0.068272$. Combination rules for atomic radii and well depths are, respectively, cubic mean and Waldman-Hagler (W-H) rule.

Appendix D

Line-Search Method of Optimizing the Hamiltonian for EDFT

The Hamiltonian is optimized by a line-search algorithm in the space of Hamiltonian elements [123] for a fixed set of NGWFs. Let $\tilde{\mathbf{H}}^{(m)}$ denote the Hamiltonian that is formed from the m-th electron density, $n^{(m)}$, whose molecular orbitals were in turn solved from a trial Hamiltonian, $\mathbf{H}^{(m)}$, as

$$\mathbf{H}^{(m)}\mathbf{M}^{(m)} = \mathbf{S}\mathbf{M}^{(m)}\boldsymbol{\varepsilon}^{(m)} \tag{D.1}$$

where $\mathbf{H}^{(m)}$ and $\tilde{\mathbf{H}}^{(m)}$ are the matrix representations of the corresponding Hamiltonians in NGWFs, $\mathbf{S}$ is the overlap matrix of NGWFs, $\mathbf{M}^{(m)}$ is the coefficient matrix for the molecular orbitals expanded in NGWFs, and $\boldsymbol{\varepsilon}^{(m)}$ is the diagonal matrix of orbital energies. According to the line-search algorithm, the next Hamiltonian is determined by

$$\mathbf{H}^{(m+1)} = \mathbf{H}^{(m)} + \lambda\Delta^{(m)} \tag{D.2}$$

with the definition of

$$\Delta^{(m)} \equiv \tilde{\mathbf{H}}^{(m)} - \mathbf{H}^{(m)} \tag{D.3}$$

and λ is a damping parameter fitted against a polynomial such that the Helmholtz free energy is minimized [22, 123]. Equation (D.2) can then be rewritten as

$$\mathbf{H}^{(m+1)} = (1-\lambda)\mathbf{H}^{(m)} + \lambda\tilde{\mathbf{H}}^{(m)} \tag{D.4}$$

The line-search algorithm performs the iterations over m until the Liouville equation is satisfied when the commutator, $\left[\tilde{\mathbf{H}}^{(m)}, \mathbf{K}^{(m)}\right]$, attains zero, with the definition of the elements of the density kernel, $\mathbf{K}$, as

$$K^{ij} = \sum_k M^i{}_k f_k \left(\mathbf{M}^\dagger\right)_k{}^j \tag{D.5}$$

During the line-search algorithm of EDFT, the constraints of SCF MI are imposed, thereby affecting the search direction in the Hamiltonian space and, in turn, the molecular orbitals determined from it (Figure 8.1). The resulting molecular orbitals, expanded in the NGWFs of the corresponding fragments, would therefore satisfy the constraints of SCF MI. Along with the fractional occupancies determined from the Fermi-Dirac distribution during the line search of EDFT, the density kernel can thus be constructed and used in calculating the electron density. The optimization process minimizes the Helmholtz energy.